Brigham Young University
BYU ScholarsArchive

Theses and Dissertations

2021-05-25

Spatiospectral Features in Supersonic, Highly Heated Jet Noise

Kevin Matthew Leete
Brigham Young University

Follow this and additional works at: https://scholarsarchive.byu.edu/etd

 Part of the Physical Sciences and Mathematics Commons

BYU ScholarsArchive Citation

Leete, Kevin Matthew, "Spatiospectral Features in Supersonic, Highly Heated Jet Noise" (2021). *Theses and Dissertations*. 9509.
https://scholarsarchive.byu.edu/etd/9509

This Dissertation is brought to you for free and open access by BYU ScholarsArchive. It has been accepted for inclusion in Theses and Dissertations by an authorized administrator of BYU ScholarsArchive. For more information, please contact ellen_amatangelo@byu.edu.

Spatiospectral Features in Supersonic, Highly Heated Jet Noise

Kevin Matthew Leete

A dissertation submitted to the faculty of
Brigham Young University
in partial fulfillment of the requirements for the Degree of

Doctor of Philosophy

Kent L. Gee, Chair
Tracianne B. Neilsen
Brian E. Anderson
Scott D. Sommerfeldt
Steven E. Gorrell

Department of Physics and Astronomy

Brigham Young University

Copyright © 2021 Kevin Matthew Leete

All Rights Reserved

ABSTRACT

Spatiospectral Features in Supersonic, Highly Heated Jet Noise

Kevin Matthew Leete
Department of Physics and Astronomy, BYU
Doctor of Philosophy

The sound produced by military aircraft is dominated by noise generated by the turbulent mixing of the jetted exhaust with the ambient air. This jet noise has the potential to annoy the community and pose a hearing loss risk for military personnel. The goal of this dissertation is to characterize spatiospectral features in the field produced by full-scale military aircraft that are not traditionally seen at the laboratory scale and identify potential noise mechanisms for these features. Measurements of two military aircraft jet noise fields are found to be best described as a superposition of spatiospectral lobes, whose relative amplitudes dictate the overall directivity at each engine power. Near-field acoustical holography techniques are applied to one of the military aircraft measurements to characterize the behavior of the lobes as a function of engine power. The simulated jet noise of a highly heated laboratory-scale jet is then analyzed to compare with the military aircraft measurement and is found to only partially contain the spatiospectral lobe phenomenon. Application of near to far field coherence tracing and near-field acoustical holography to the simulations provides validation of the methods used on the military aircraft and illuminate potential source mechanisms that may explain the presence of the spatiospectral lobes.

Keywords: aeroacoustics, jet noise, near-field acoustical holography, coherence analysis, large eddy simulations, military aircraft

ACKNOWLEDGMENTS

To my wife, who has provided every good thing in my life and gives me the reason to wake up in the morning and go to work.

To my advisor, who's mentoring efforts have turned my work into something worthwhile. He has provided me all the opportunities a young scientist could ever hope for: a seemingly limitless supply of fun and difficult problems to work on, a critical eye, and the support I needed to succeed.

I am also exceedingly grateful to the Air Force Research Laboratory, Larry and Julia Royster, and Leo and Gabriella Beranek for the fellowships and scholarships which have allowed me to perform this research and still provide for my young family.

Contents

List of Figures

List of Tables

Chapter 1

Introduction

Turbulent fluid flow generates noise. From the characteristic sound of a sharp exhalation to the roar of a military aircraft flying overhead, the fundamental laws governing the motion of the fluid are simply those of Newton. One may then think that understanding the generation of sound from fluids would be simple, though as fluid dynamicists can attest, calculating fluid flow can become prohibitively difficult very quickly. The Navier-Stokes equations, which are the result of the application of Newton's laws to continuous fluids, usually have no analytical solution.

The aeroacoustic noise on which this dissertation focuses is simply called jet noise, and refers to the noise generated from gas being exhausted from an orifice, or jet. The most impactful source of jet noise to the everyday person is that caused by the exhaust of turbojet aircraft. To achieve the thrust required to fly, aircraft must expel a large volume of air quickly, which in turn generates a lot of noise. This jet noise has the potential to annoy communities and harm to those who work in close proximity to aircraft. As the design of aircraft has changed over the years, commercial passenger aircraft have increased the bypass ratio of their engines, and as a result of this increase, the jet noise has decreased significantly [1]. Military jet aircraft and supersonic commercial aircraft, however, do not have this luxury, as this would significantly increase drag and impact performance.

Rockets to power spaceflight are another source of jet noise, which can be so loud that vibroacoustic loading by the radiated sound on the body of the launch vehicle can cause mission failure [2, 3]. Additionally, with the increase in interest in commercial spaceflight, community noise could become a huge issue as the number of spaceports near urban centers increases.

The generation, propagation, and reception of jet noise is then an important area of research for current and future goals of military and civilian groups. This dissertation focuses on understanding the spatiospectral characteristics of jet noise generated by high-performance military aircraft, which is often significantly different from jet noise studied at smaller scales. Two measurements of military aircraft and a numerical simulation of a laboratory-scale jet (operating near military aircraft conditions) are examined to investigate the important features of the radiated sound and their corresponding source mechanisms.

In the following sections, I present a brief overview of some of the major points of jet noise research over the past fifty years, covering the development of acoustical analogies, experimental measurements of jets, numerical simulations of jets, field decomposition analysis, wavepacket analysis, and the current state of understanding of the basic description of the jet noise field and their source mechanisms.

1.1 Jet Noise Research Overview

One can think of the start of jet noise research as being with Sir James Lighthill's 1952 paper [4] where he rearranged the Navier-Stokes equations so that a linear wave operator was on the left hand side and a complex expression involving a multidimensional tensor of Reynolds stresses was left on the right. This formulation is interpreted as the jet noise problem being analogous to an equivalent fictitious problem in a quiescent medium with an array of sources described by the complicated terms on the right-hand side. This is known as "Lighthill's acoustic analogy", with the tensor named

Lighthill's stress tensor. The benefit of the acoustic analogy is that it allows for all known solutions to the wave operator to be applied immediately: if the values of the stress tensor are known at all points within the jet, then a simple Green's function integration would be sufficient to calculate the sound pressure everywhere. The problem that naturally arises is that one must know essentially all the fluid variables everywhere in the flow to be able to calculate the acoustic pressure fluctuations in the field.

Early experiments by Morley [5] found that the overall acoustic power of subsonic jets scaled as the exit velocity to the eighth power. Subsequent application and manipulation of Lighthill's theory by many authors (summarized in [6]) lead to the conclusion that aeroacoustic sources can be represented by quadrupoles, which ends up matching the experimentally discovered velocity scaling. However, the lack of explicit evidence of acoustic quadrupoles in the flow still remains a topic of discussion among researchers [7].

The fundamental idea behind an acoustic analogy is that the problem of solving the Navier-stokes equations everywhere is reduced to thinking of the turbulent interactions in the flow (the components of Lighthill's stress tensor) as acoustic sources that behave like any other source. This idea of generating an equivalent acoustic source for jet noise is a concept that motivates research to this day.

Jet noise fields are unique because frequency content and coherence properties are spatially dependent. Towards the sideline, the spectrum is more broadband and the field is less coherent, while at large aft angles the spectrum becomes peaked and more coherent. This phenomena is so consistent between jets of many shapes, sizes, and (mostly subsonic) speeds that Tam et al. [8, 9] were able to generate empirical fits to the shape of the two spectra (called similarity spectra) based on a repository of data from a large number of laboratory-scale jets. The superposition of spectra suggest that multiple independent source mechanisms (responsible for each spectral shape) are in play in the plume.

Before the 1970s, jet turbulence was thought of simply as a distribution of many small turbulent eddies [10]. However, only the incoherent, broadband noise towards the sideline of the jet fit that source description. Visualizing larger structures in the flow [11, 12] led to the idea that the aft radiation was due to large coherent structures. Correlation analyses [13–15] between the measured flow in the plume and microphone recordings in these two acoustic field regions support the idea that large-scale structures are responsible for the downstream coherent radiation and small eddies throughout the mixing region are responsible for the sideline radiation.

This paradigm for jet noise has been championed by Tam et al. [8] with their development of the similarity spectra. The source mechanisms corresponding to the two similarity spectra have come to be known as large-scale turbulence structures and fine-scale turbulent structures. Fine-scale turbulent structures are understood as small eddies or other perturbations in the mixing region of the flow, which exert an effective turbulence pressure on their surroundings [16], creating acoustic waves that propagate through the flow out to the ambient air. Due to counteracting effects of convection of the sound downstream by the flow and refraction as it transitions from the flow to the ambient air causes the sound to be nearly omnidirectional [9]. Large-scale turbulence structures are generally accepted to be due to Kelvin-Helmholtz instability waves generated at the shear layer of the jet near the nozzle [17] that grow as they convect downstream.

When the jet flow becomes supersonic, additional components of the noise field are present, complicating its description. When supersonic jets are operated off design (such that the pressure of the flow leaving the nozzle does not equal the ambient pressure), shocks and expansion fans are generated in the resulting flow creating quasi-periodic diamond patterns called shock cells or Mach diamonds. These shocks and expansion fans interact with the turbulence that propagate though them to generate a new type of noise called broadband shock-associated noise (BBSAN). This noise component radiates in the forward direction, and its peak frequency is dependent on the shock cell spacing. Models of this noise component are known and agree well with laboratory-

scale measurements [18, 19]. Additionally, the presence of the shock cells cause an acoustical impedance boundary in the flow, such that some percentage of the acoustically-propagating pressure fluctuations may resonate between the shock cells and the nozzle exit, causing a loud, tonal noise called screech [20]. Screech is not seen often in high-performance military aircraft, though BBSAN is [21].

An additional implication of supersonic flow is that the radiation from large-scale turbulent structures becomes extremely efficient. As the turbulent structures convect downstream supersonically, they create nearly plane-wave like wavefronts that radiate at aft angles corresponding to the convective Mach number of the propagating disturbance. This phenomenon is called Mach wave radiation, though the term seems to be used interchangeably with the phrase "large-scale turbulent structure noise" to refer to the aft radiation of supersonic jets.

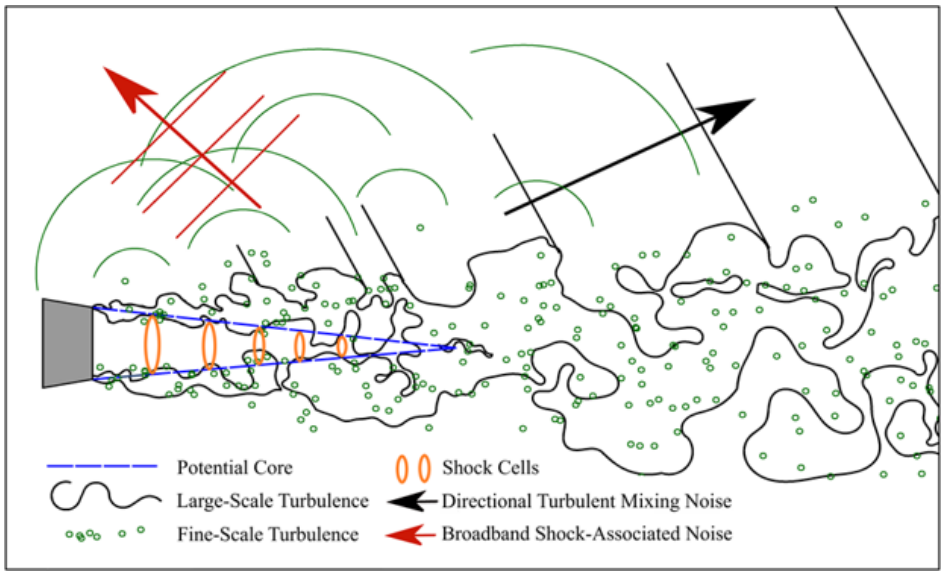

Figure 1.1 Schematic depicting a supersonic jet operating off-design with corresponding typical noise components. Large scale turbulence structures radiated noise to the aft, fine scale radiates omnidirectionally, and BBSAN radiates in the forward direction.

Each of these noise components: large-scale turbulent structure radiation, fine-scale structure radiation, screech, and BBSAN have been studied extensively over the years using various numerical

and experimental methods, mostly at the laboratory scale. A schematic, adapted from Ref. [22], in Fig. 1.1 depicts the major components of jet exhaust operating off design with their corresponding noise components.

1.2 Flow Imaging and Decomposition

In agreement with the acoustic analogy of Lighthill, the complex interaction of pressure, temperature, and the three-dimensional components of the velocity all contribute to the radiated noise. Thus, imaging these fields has been an active area of research. Direct measurements of the turbulence began with invasive procedures such as Pitot tubes and hot-wires, but have developed into many complex, less-invasive methods including Rayleigh scattering [23], particle image velocimetry [24], and Schleiren imaging [25]. These sensitive tools can calculate pressure or particle velocities of entire flow fields simultaneously, allowing for more in-depth analysis of how the flow develops over space and time.

With the advent of these full-field imaging methods, the sheer amount of data generated in measurements necessitates the distillation of the flow fields into their most important components. A plethora of flow decomposition techniques have been applied in various fluid dynamics situations [26] and subsequently applied to jet noise. Some of these methods are theory-driven, such as decomposing the field into acoustic, hydrodynamic, and thermal modes using Doak's momentum potential theory [27, 28], or operator-based analysis such as global linear stability analysis [29] and resolvent analysis [30]. Other decompositions are data-driven, like the spectral proper orthogonal decomposition (SPOD) [31] and dynamic mode decomposition [32]. Operator-based decompositions add information about cause and effect relationships within the flow and between the flow and acoustic radiation and follow-up studies have found relationships between the data-driven and operator-based decompositions [33].

Understanding the decomposed time-harmonic flow field is similar to understanding the radiation from a vibrating surface. When the velocity of bending waves on a plate is higher than the sound speed in the adjacent air at a given frequency (or in other words, is "supersonic"), that frequency is found to radiate efficiently into the field. The large, coherent structures (which are readily visualized by the decomposition methods above) in the flow can be modeled similarly by finding a time-averaged phase relationship over a portion of the flow. If this phase relationship is supersonic compared to the adjacent ambient air, then efficient, directional radiation (Mach wave radiation) occurs at that frequency. The partially coherent nature of the field, however, suggests a superposition of a multiplicity of these structures. The time-averaged amplitudes of these structures over space often start small, saturate to a maximum value, then decay again, resembling a wavepacket [34]. The decomposition of the acoustic [35, 36] and flow [31] fields into wavepackets is an ongoing area of research, with the goal to reduce the complicated jet noise problem into a combination of simple wavepacket shapes. Progress in measurement techniques in the laboratory as well as availability of detailed simulations of the jet plume provide opportunities to apply decomposition techniques to entire flow fields, and these decomposed flow fields are then compared to this wavepacket analogy, or wavepackets directly educed from the flow field.

Decomposition methods, jointly with the acoustical analogy framework and understanding of radiation from wavepacket-like structures lays out the backbone of understanding of the large-scale turbulent structure noise of supersonic jets.

1.3 Numerical Simulations

Simultaneous with the increase in flow decomposition and flow-field imaging methods, numerical simulations of jet noise have also become a widely used and powerful tool [37]. The most straightforward method is called direct Navier-Stokes (DNS) that simply solves the Navier-Stokes

equations numerically. To resolve all the turbulence scales, DNS requires a very fine mesh and is extremely computationally taxing, though it is the most accurate method available. On the other end of the spectrum, Reynolds-averaged Navier–Stokes (RANS) use a Reynolds decomposition of the Navier-Stokes system to solve for the time-averaged fluctuations about a mean value. Since noise is caused by turbulence and the turbulence is modeled instead of calculated, this method's evaluation of the noise is inaccurate, though it has a fast computation time. Large eddy simulations (LES) provide a balance between these two methods: it solves directly for the larger scales and the smaller, sub-grid scales are modeled. Since the large turbulence scales are more effective than the fine turbulence scales at generating noise (particularly in supersonic jets), LES has proven itself a suitable method for calculating jet noise.

To predict the far-field noise generated by jet flow, one could certainly expand their computational domain into the far field, though this becomes quickly impractical. Acoustic analogies, then, are applied to the jet flow field after the computation is complete to calculate the far-field acoustics. A volume integral of Lighthill's source terms, for example, can be calculated directly from the LES-generated data to calculate the far-field acoustics. This volume integral is extremely resource expensive.

The Ffowcs Williams and Hawkings (FW-H) integration method is an alternate method to calculate the far-field acoustics, where a virtual surface [Ffowcs Williams and Hawkings surface, (FWHS)] is drawn surrounding the flow and a Rayleigh-type surface integral is taken of the pressure or velocity components on the surface [38]. The placement and extent of the FWHS is often chosen based on trial and error: it needs to be far enough outside the flow and large enough that it contains all the sources, though near enough that the often-variable grid used in the numerical simulations is dense enough to resolve the salient acoustics. Generally, it is a conical surface that parallels the shear layer, without end caps. FW-H integration is convenient for supersonic jets because the vast majority of the radiated sound energy goes right through this kind of conical surface.

Numerical simulations are ideal because they can provide full flow data for decomposition techniques as well as predictions of the far-field acoustics through the FW-H integration methods. As computational schemes become more advanced, more and more difficult jet noise problems (such as simulating highly supersonic military aircraft jets) can be investigated. At this time, for example, there are few LES of highly-heated jets at temperature ratios on the same order of military aircraft jets at afterburner [39–42] and have not been directly validated through laboratory-scale investigations because of difficulties in reproducing these extreme temperatures in the lab.

1.4 Rockets

Parallel to the investigations of jet noise source phenomena, the jet noise caused by rocket plumes has been an engineering challenge. With the advent of the space race in the 1950s and 60s, rapid development of more and more powerful rockets took place, and it was found the acoustic loading from the noise on the rocket body could cause equipment failure during takeoff. Subsequent research done to understand and mitigate the noise generated by rockets has focused on semi-empirical methods. NASA SP-8072 [43] was a landmark document that provides normalized spectra, estimates of axial distributions of overall sound power, and sound source position as a function of frequency generated using laboratory-scale supersonic jet and full-scale rocket data [44, 45]. It presents a method to apply these generalized spectra by scaling to the specific test at hand to create an equivalent source model of the jet noise, consisting of a distribution of sources along the jet centerline. The strength of these sources is related to the mechanical power of the jet through an assumed acoustic efficiency of about 0.5%, or 1% as a conservative upper bound.

Since then, several studies have focused on adapting these empirical relations so that they match more recent data as they became available [46–48], often tuning the definitions of characteristic lengths [49], as well as including the integration of computational schemes [50, 51] for generation

and propagation of the sound field. Recent work [52] has shown that a plotting error in the original NASA SP-8072 document has led to an understanding in the rocket noise community that the main source of noise is the subsonic portion of the flow, while in the jet noise community it is understood that the main acoustic power originates between the potential and supersonic cores [45]. The state of the art for rocket noise prediction then is a combination of semi-empirical methods, involving estimating the source locations and strengths from a combination of normalized parameters and scale model testing of the rocket being investigated.

There is a certain disparity between the rocket and jet noise communities in that many of the normalization schemes that work for laboratory-scale jets (which use Strouhal number to normalize their spectra and the nozzle diameter to normalize the lengths) do not seem to apply directly to rockets, where the peak of the spectra on a Strouhal number scale is an order of magnitude lower. Additional scaling schemes that attempt to unite these two disparate spaces have been proposed [53], but not widely adopted.

1.5 Measurements of Full-Scale Aircraft

In recent years, several high-quality measurements of military aircraft jet noise have been produced [54–56]. Using the similarity spectra to verify that these measurements follow established trends in jet noise, however, provided some challenges. Neilsen et al. [57], when fitting the similarity spectra to a rectangular-nozzled aircraft, showed how the fine-scale similarity spectrum fit the field towards the sideline, the large-scale spectrum fit in the area of maximum radiation, and a mixture of the two fit in the boundaries around the area of maximum radiation. Where the spectrum did not fit was when the aircraft was run at high engine powers and the measured spectrum in the direction of maximum radiation exhibited multiple peaks. Multiple peaks in the spectra were subsequently

observed in a measurement of an F-18 and F-35 aircraft, and the same issues arose when fitting similarity spectra to their fields [56, 58].

With the observations of the dual-peaked spectrum in the aft radiation of these three aircraft, Tam and Parrish [59] suggested that the additional spectral peaks were attributed to combustion noise originating in the nozzle. Liu et al. [39, 40] hypothesized that the increase of temperature of the flow causes the radiation originating from the potential core region to have a different directivity than the radiation originating from the subsonic, downstream portion of the flow. They used LES of laboratory-scale jets of increasing total temperature ratio to show that the Mach wave radiation's directivity shifted towards the sideline, though the portions of the flow that were beyond the supersonic core still maintained a shallower directivity, thus identifying the importance of the distinction between Mach wave radiation and large-scale turbulence structure noise. However, when looking at a single point in space, no multiple peaks in the spectra were observed.

Follow up studies of the correlation and coherence of the measured fields of the rectangular-nozzled aircraft [60] and the F-35 [61] show that the multiple peaks in the spectra are mutually uncorrelated, which suggests they may be due to independent noise sources. Swift et al. [61], analyzing the F-35 field, found that BBSAN was partially coherent with the aft radiation, and could potentially be a cause for the multi-lobed spectra.

Additional speculations of the cause of the multi-lobed spectra involve the interaction of the jet with the hard ground. Investigations of laboratory-scale jets near rigid boundaries [62–67] provide evidence of additional noise components due to jet-surface interactions at frequencies below the peak frequency of the jet noise.

1.6 Inverse Methods

Jet noise has often been seen as a fluid dynamics phenomenon that happens to radiate noise and has been investigated as such. Investigations of the Lighthill stress tensor and complicated simulations and decompositions of the flow have been the leading driver of understanding of the jet noise problem. However, because of the sensitive nature of the details of military aircraft engines, this line of thinking is near impossible to take when investigating the deviation of the jet noise created by military aircraft from laboratory-scale counterparts. Thus, to understand the noise source of military aircraft, it is necessary to start from the acoustic field and look backwards into the flow.

Acoustic inverse methods have been instrumental in understanding the localization and characterizations of acoustic sources for many years, and a wealth of array-based localization techniques are available. Two of these techniques, near-field acoustical holography [68] and beamforming [69], have been applied to jet noise in recent years, both at the laboratory and full-scale. Beamforming [70–75] is based on an equivalent source model (ESM), which assumes some distribution of monopoles as a source, then calculates the strength each source would need to combine together to make the measured field at the location of measurement. Near-field acoustical holography (NAH) uses an equivalent wave model (EWM), which assumes that the field in the region of the measurement can be decomposed into a linear combination of a set of wavefunctions. Those wavefunctions can then be fit to the measurement data and evaluated at another location to reconstruct the field at that location. Near-field acoustical holography, which was developed for the general three-dimensional imaging of noise fields [76, 77], has been used in laboratory jet noise measurements [78–81] and was recently adapted to full-scale measurements of the jet noise produced by military aircraft [82, 83].

Alan Wall's dissertation [84] focused on developing a variant of statistically optimized near-field acoustical holography (SONAH) called multisource statistically optimized near-field acoustical holography (M-SONAH) [85], which uses two sets of basis function in the EWM instead of just

one. This was formulated so that the noise field surrounding the rectangular nozzled aircraft in Ref. [54] could be reconstructed, as one set of wavefunctions was to represent the direct sound from the plume and the second from the reflected sound from a virtual source located below the ground. The M-SONAH technique was successful in reconstructing the field in a large area surrounding the aircraft based on two-dimensional measurements taken in the near field. These measurements were a massive undertaking, with a dense array of 90 microphones being laterally translated downstream parallel to the jet plume of the aircraft over multiple measurements to cover the desired area. Though this method provided two dimensional measurements, it was found that including an axisymmetric assumption in the formulation of the EWM did not decrease the reconstruction accuracy.

Taking reconstructions of the field along the nozzle lipline, Wall et al. [36] were able to apply a decomposition method that was able to generate an equivalent acoustic source for the field generated by the aircraft in Ref. [54]. This source was tailored to identify independent coherent phenomena in the plume as a function of frequency and split the multiple directivities associated with the independent spectral peaks into separate sources, suggesting the spectral peaks be associated with different fluid dynamics phenomena. This type of analysis was repeated by Harker et al. [75], though using a different decomposition method of the source generated by a beamforming method applied to the same measurement.

1.7 Scope

The purpose of this dissertation is to characterize the field produced by high-performance military aircraft and investigate potential source mechanisms for the presence of multiple peaks in their spectra. This is accomplished by:

1. Adapting the near-field acoustical holography methods developed by Ref. [84] to measurements of an F-35 aircraft [55].

2. Measuring the field of the new Boeing T-7A trainer aircraft.

3. Investigating the radiated field of a LES of a highly heated laboratory-scale jet [40].

4. Applying NAH to the radiated field of the LES as if it were a measurement of a full-scale aircraft and comparing the properties of the flow to the reconstructions.

This dissertation is a compilation of five individual works (each contained in a Chapter) that accomplish these goals. Chapter 2 presents an acoustical holography-based analysis of spatiospectral lobes in the measured jet noise field of an F-35 aircraft. It discusses how the multiple peaks in the spectra measured of full-scale aircraft are better described as multiple lobes in the spatiospectral domain, which change as a function of engine power. Chapter 3 details a follow-up study to the first, which investigates the accuracy of the adapted M-SONAH method and discusses the applicability of the EWM to reproducing the effects of the hard ground on the measurements. Chapter 4 contains a publication describing the large, multi-organizational effort to measure the field radiated by the T-7A aircraft and the efforts to identify data artifacts. Spatiospectral lobes following the same pattern of those observed in the F-35 measurement are seen.

Chapter 5 shifts gears and presents an analysis of the field observed of a LES of a highly heated laboratory-scale jet. The coherence function is calculated in the field and between points in the flow and the field, in a similar fashion as was done on a laboratory scale jet in Ward et al. [86]. Chapter 6 contains an application of SONAH to the same simulation, with the ability to compare the source reconstructions of the field to actual LES data to verify the holography applied to the F-35. The final analysis in Chapter 6 is the calculation of the axial distribution of sound power using the LES-generated field and the holographic reconstructions.

Because flow parameters of the F-35 and T-7A are unknown, direct investigation of the source phenomena responsible for the spatiospectral lobes measured in the field of these aircraft is unavailable. The addition of the LES of a highly heated laboratory-scale jet, however, provides

opportunities to use the NAH methods applied to the F-35 on the LES and subsequently compare the flow parameters generated by the simulations to the NAH reconstructions. The juxtaposition of the full-scale military aircraft measurements with the LES allow for investigation of potential source mechanisms of the spatiospectral lobe phenomenon.

Chapter 2

Acoustical Holography-based Analysis of the Spatiospectral Lobes of the F-35

This work was accepted for publication in AIAA Journal February 18th, 2021 under the title "Acoustical Holography-based Analysis of Spatiospectral Lobes in High-performance Aircraft Jet Noise". I hereby confirm that the use of this article is compliant with all publishing agreements.

2.1 Abstract

Holographic reconstructions of the sound field in the vicinity of a tied-down F-35 aircraft were achieved by applying multisource statistically optimized near-field acoustical holography to measurements taken at a linear ground array approximately parallel to the shear layer of the jet. The measured field, as well as reconstructions to locations where the field was not measured, show that the field can be described as a superposition of multiple lobes in the spatiospectral domain. These lobes are observed in the field when the aircraft is operated at a variety of engine powers, including afterburner. For a given engine power, as frequency is increased the spatial lobes in the mixing noise region shift aft in directivity until they disappear beyond the aperture of the measurement

while new ones appear towards the sideline and shift aft with the others. At a fixed frequency, when engine power is increased the forward-most spatial lobe increases in level more than the other lobes, which is a major factor in the observed forward shift in overall directivity with increasing engine power. Frequency-dependent raytracing of the spatial lobes gives insight into the directivity and apparent source locations for jet noise components as a function of frequency and engine power.

2.2 Introduction

Although important insights are gained from laboratory-scale investigations of jet noise, some aspects of jet noise produced by full-scale military aircraft have not yet been reproduced by laboratory-scale measurements. Additional insight into aeroacoustic noise is, therefore, obtained by application of techniques used in laboratory settings to measurements of full-scale, high-performance military aircraft. Two such techniques are beamforming and near-field acoustical holography (NAH). Beamforming has been successfully used to image aeroacoustic sound sources in the laboratory [70, 72] as well as at the full-scale [71, 73–75]. Near-field acoustical holography, which was developed for the general three-dimensional imaging of noise fields [76, 77], has been used in laboratory jet noise measurements [78, 80, 81, 87], and was recently adapted to full-scale measurements of the jet noise produced by military aircraft [82, 83]. The NAH process involves fitting an equivalent wave model (EWM) for the field under examination to measured data (called a hologram). This fitted EWM can then be evaluated at any point of interest and provides reliable estimations of the field as far as the assumptions in the EWM hold. Acoustical holography studies of jet noise from high-performance military aircraft have been successful in showing trends across frequency and engine conditions in both the source extent and directivity [83].

Wall *et al*. [85] used an advanced method of NAH called multisource statistically-optimized NAH (M-SONAH) to investigate the characteristics of the field in the vicinity of an F-35 operating

at 100% Engine Thrust Request (ETR). Using a ground-based linear array as the input to the holography process, reconstructions were achieved over a large area within the aperture of the hologram. At several frequencies in the region of maximum radiation, multiple radiation lobes were observed. As frequency increased, as many as four individual lobes emerged towards the sideline, moved aft, and submerged back into the overall field. Evidence of broadband shock associate noise (BBSAN) was also observed as a lobe propagating in the forward direction [58, 88].

The presence of multiple radiation lobes in military aircraft jet noise has been seen in several data sets [54–56, 89], though no conclusive explanation of its cause has been given. These lobes are described as either multiple peaks in the spectra at a given measurement location or as multiple local maxima in the directivity when plotting a single frequency across space. Evidence of spatiospectral lobe content in laboratory-scale measurements is sparse. In one example, Long [87] used NAH to image the source from a heated laboratory-scale jet and showed striation patterns in the spatial/spectral domain.

Several studies have proposed explanations for multiple lobes. Tam and Parrish [59] sought to explain dual spectral peaks shown in one-third octave band spectra of a rectangular-nozzled aircraft [57] in terms of indirect combustion noise sources that originate from within the nozzle. Liu *et al*. [39, 40, 90, 91] investigated temperature ratio as a possible cause of multiple lobes by using large-eddy simulations of laboratory-scale jets and showed far-field evidence for at least two noise source mechanisms which became more distinct as temperature ratio is increased. Schmidt *et al*. [31], doing spectral proper orthogonal decomposition and resolvent analysis of large-eddy simulations of cold laboratory-scale jets, show two main low-rank wavepacket structure types: one in the initial shear layer of the jet near the nozzle with a high phase speed and another found downstream, more spatially extended, and with a lower phase speed. These wavepacket types qualitatively agree with the two source mechanisms observed by Refs. [39, 40, 90, 91], as discussed in Ref. [92].

Previous NAH [36] and beamforming [35] performed on measurements of military aircraft jet noise have constructed equivalent source models that have been successful in reproducing the sound field. These reduced-order equivalent source models use multiple independent sources to contribute to individual spatiospectral lobes, suggesting that the multiple lobes are incoherent. Swift *et al*. [61] performed an extensive correlation and coherence analyses on the same data set presented in this paper that verifies incoherence between lobes. The incoherence between the lobes suggest that they may be due to independent sources or source mechanisms. Additionally, Ref. [61] shows correlation between the aft radiation where multiple lobes are present and BBSAN in the forward direction, which suggests that shock cell interactions could be a contributor to these multilobe effects.

The purpose of the current study is to use M-SONAH, which was developed for the use of imaging the field produced in the presence of a ground reflection, to reconstruct the sound field produced by a tied-down F-35B aircraft running at various engine conditions. Trends in observed spatiospectral lobes and BBSAN across engine power are presented in a large area surrounding the jet for select frequencies. The measured and reconstructed fields show that the noise in the region of maximum radiation is a superposition of multiple spatiospectral lobes, where the overall trends across frequency and engine power are best described by the number and levels of the individual lobes present. Prior observations of a "dual-peak" or multilobe phenomena in Refs. [56, 59, 83] appear to be subsets of the more complete picture described herein.

2.3 F-35 Measurement

This section discusses the measured spectra and OASPL gathered from a ground-based array in the geometric near field approximately parallel to the jet shear layer and a far-field arc array 1.5 m off the ground. Spatiospectral lobes are seen at all engine powers.

2.3.1 Setup

Extensive static measurements of the F-35 A and B variants were performed at Edwards Air Force Base in 2013 [55]. The aircraft were tied down on a concrete run-up pad while the engine was cycled through various engine conditions, including 13% ETR to 150% ETR. Engine powers greater than 100% ETR are due to the addition of afterburner. This paper uses measurements of the B variant, which had a Pratt & Whitney F135-PW-600 afterburning turbofan engine. The nozzle of the engine was 2 m from the ground and had a nominal 1 m diameter, though the exact nozzle diameter changed with engine condition. Jet parameters such as Mach number, nozzle pressure ratio, temperature, and exact nozzle diameter for each engine power are unknown by the authors, so no Strouhal number or other type of scaling is attempted in this work.

The coordinate system used in this study is centered on the nozzle exit (with the point on the ground below the nozzle exit as the origin) with the jet exhausting in the positive z direction, as illustrated in Fig. 2.1. The x-axis is the horizontal distance from the jet centerline and the y-axis is the height above the ground. Cylindrical coordinates are used in the M-SONAH algorithm, with r being the radial distance from the z axis. Another useful coordinate is the jet inlet angle, θ, which is measured from the direction of the aircraft nose ($-z$ direction) around a microphone array reference point (MARP) which was located at $z = 7.5$ m. The array was laid out to the left side of the aircraft as shown in Ref. [55], though for ease of plotting and consistency with previous NAH studies, all plots here are mirrored to show it on the right side of the aircraft. This study focuses on a 32 m long, 71-element (0.45 m interelement spacing) linear ground array placed approximately parallel to the shear layer, which is used as the input to the holography processing and is referred to as the holography array. An arc array located 38m from the MARP is also used to validate the field reconstructions. Figure 2.1 shows a schematic for the test geometry with the coordinate system and the approximate location of the F-35B.

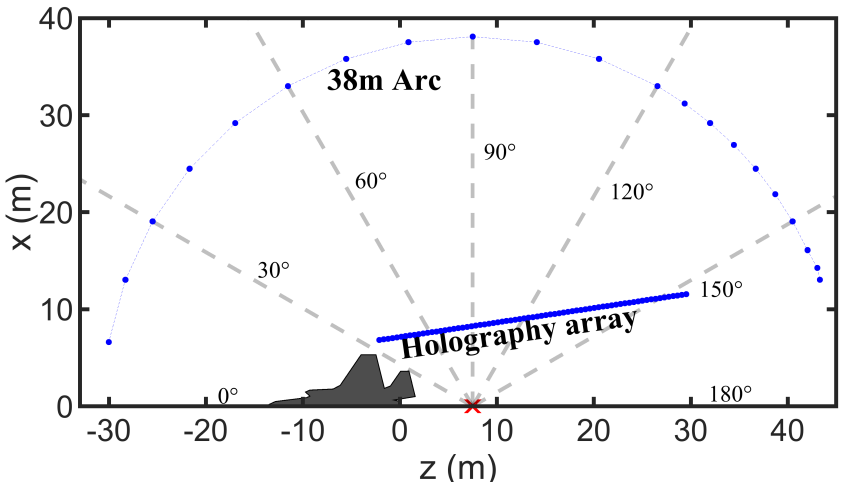

Figure 2.1 Holography array and 38 m arc positions for the F-35B. The red marker is the microphone array reference point (MARP), which was 7.5 m behind the nozzle.

2.3.2 Measured Data

The measured data along the 71-microphone holography array demonstrate how the sound field varies with engine condition. The measured overall sound pressure levels (OASPL) and corresponding spectra for each engine condition are shown in Figs. 2.2a) and 2.3, respectively. As engine power increases from 25% to 150% ETR, a peak in the OASPL appears at about $z = 15$ m at 50% ETR, shifts forward to about $z = 11$ m at 75%, then continues shifting forward until it settles at about $z = 8$ m at 150% ETR. The transition between 130% and 150% ETR does not increase the OASPL significantly, except for rounding out the peak. At 50% ETR and above, a secondary local maximum is seen at about $z = 22$ m. The far-field OASPL measured at the 38 m arc in Fig. 2.2b) shows the forward shift in directivity as engine power is increased, though both afterburning conditions have similar curves. The increased level in the forward direction at 25% ETR is attributed to aircraft noise, but at 75% ETR and above the increase in the forward directions is due to BBSAN [58]. There are hints of a split directivity in the OASPL at 75% ETR and greater, though the deviation

is too small and angular spacing of the array is too large to be sure. The OASPL directivity shifts from being centered at approximately 145° at 25% ETR to 125° at afterburner.

The spectra at each point on the holography array illuminate why the OASPL changes as it does. Figure 2.3 shows the sound pressure levels (SPL) for frequencies between 30 and 700 Hz (spacing of 3 Hz) for each microphone along the array. Each pane of Fig. 2.3 shows the data for an engine condition (specified above the pane). The color bar on the right (shared across panes) shows the levels relative to the peak, which is specified above each pane. At 25% ETR, the left portion of the array ($z < 10$ m) appears to be dominated by engine noise, with the louder jet noise farther aft. At 50% ETR and above, jet noise dominates the whole array. For engine conditions at 75% ETR and above, radiation in the forward direction is observed between 300 Hz and 700 Hz, which analyses in Refs. [58, 88] show to be BBSAN.

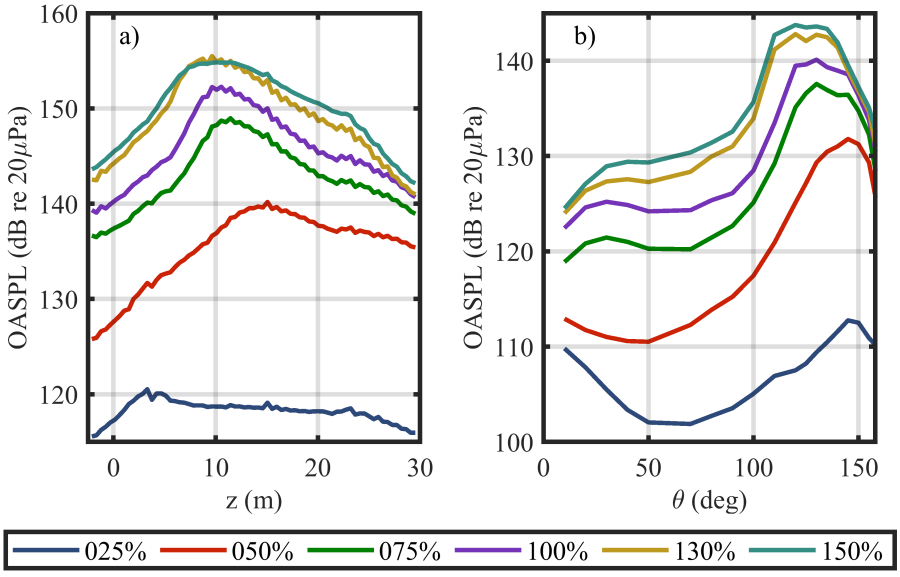

Figure 2.2 OASPL across the a) holography array and b) 38 m arc for several F-35B engine conditions (given in % ETR).

The most prominent feature of the spatiospectral plots in Fig. 2.3 is the presence of multiple lobes in the space–frequency domain. There are at least two lobes at 25% ETR, four lobes between

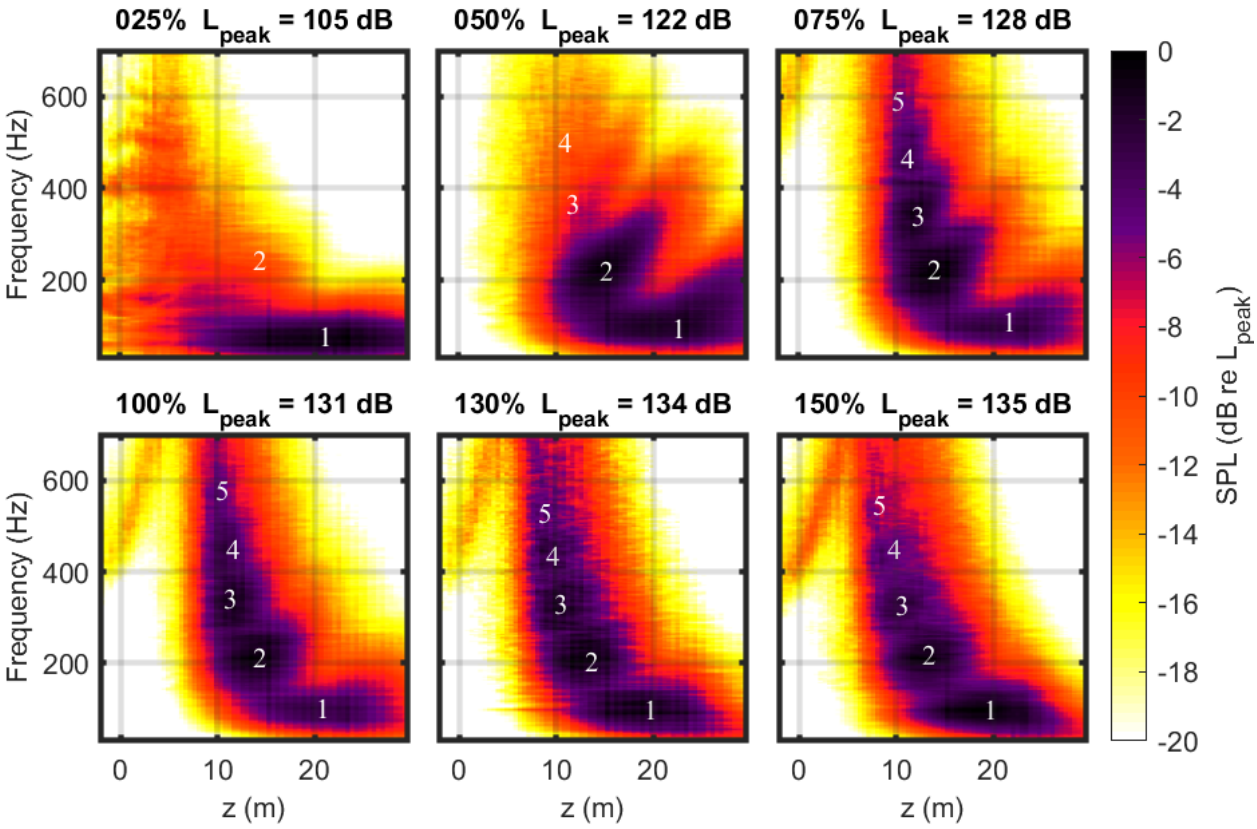

Figure 2.3 Spatiospectral maps of normalized sound pressure level on the holography array as a function of downstream distance from the nozzle (z) and frequency. The numbers indicate the several spatiospectral lobes

50% ETR and 130% ETR and five at 150% ETR. Deciphering the exact number of lobes is an ongoing research problem, with different methods being employed. For this work, the patterns of minima and maxima in the levels are used, as indicated by the white numbers on the spectra in Fig. 2.3.

The placement of each lobe in the spatiospectral domain appears consistent across engine conditions, though their individual extent, shape, and relative amplitudes differ greatly. A clear example is the difference between the 50% ETR and 75% ETR engine conditions; lobe 4 is barely visible in the 50% ETR case, but in the 75% ETR case it has a much greater contribution to the field.

The significant addition of upstream energy in the third and fourth lobes in the transition from 50% ETR to 75% ETR appears to be the single greatest contributor to the increase in OASPL and the forward shift in directivity seen in Fig. 2.2. Qualitatively, the total spectrum appears to be a simple superposition of these lobe structures, which would imply an incoherence between them. These observations seem to show that the aft radiation region, which has been attributed to "large-scale turbulent structure noise" may actually be a superposition of different noise mechanisms. Analyses in Sections 2.5.4 and 2.5.4 of this paper are geared to understand the source regions in the jet plume responsible for these spatiospectral lobes, though additional work is needed to understand if these are universal aeroacoustic phenomena or only apply to military aircraft jet noise.

2.4 M-SONAH Method

This section discusses the application of M-SONAH to the F-35B measurements (described in Sec. 2.3) to reconstruct the time-averaged complex pressure field in the area surrounding the aircraft. M-SONAH, developed by Wall *et al*. [82], modifies the traditional SONAH algorithm [93] to use a two-source model: one along the jet centerline and an image source–equidistant from but below the ground–to account for the ground reflection. Each source has a corresponding set of cylindrical basis functions that constitute the equivalent wave model (EWM) of the field. The time waveforms recorded from the holography array are the input to the M-SONAH algorithm, which includes the following steps.

2.4.1 Extract frequency-dependent complex pressures from recorded pressure waveforms

To obtain the frequency-dependent complex pressures for all measurement locations and engine conditions, the recorded 30-second time waveforms are split into multiple blocks with a 50%

overlap and windowed with a Hann function. The Fourier transform is then applied to each block. During the F-35B measurements, several organizations and different data acquisition systems with different sampling frequencies were involved in the simultaneous measurement of all the microphone channels. For this study, the block sizes for each different sampling rate were chosen such that the resultant frequency resolution was 3 Hz in all cases. The applied Fourier transform yields a single complex pressure value per block, per frequency. The remaining steps are done on a frequency-by-frequency basis.

2.4.2 Perform a partial field decomposition (PFD) to generate mutually incoherent partial fields

Application of acoustical holography fundamentally assumes that the field in question is coherent. Therefore, to apply NAH to partially coherent jet noise, the complex pressures on the holography array are decomposed into mutually incoherent, but self-coherent, partial fields that can be processed independently. After propagation, the individual partial fields are summed energetically to reproduce the total field [94]. For each frequency, the cross-spectral matrix (CSM) of the input array is calculated. The CSM is a matrix where the ij^{th} entry is the cross spectrum between elements i and j in the array. A singular value decomposition (SVD) is done on the CSM, where the singular vectors of the SVD scaled by their corresponding singular values yields a set of partial fields. The number of partial fields generated is equal to the number of elements in the input array. Figure 2.4 shows the SPL of the singular values for two representative engine powers. These singular values indicate the contribution of each partial field at each frequency. At low frequency, the field exhibits low-rank behavior; the majority of the energy is compacted by the SVD into relatively few partial fields.

Since each partial field is processed individually and the final reconstructed field is a sum of all the processed partial fields, a "filtering" of sorts can be done by only using the most energetic partial fields to reconstruct the total field. In this study, for each frequency of interest, the number

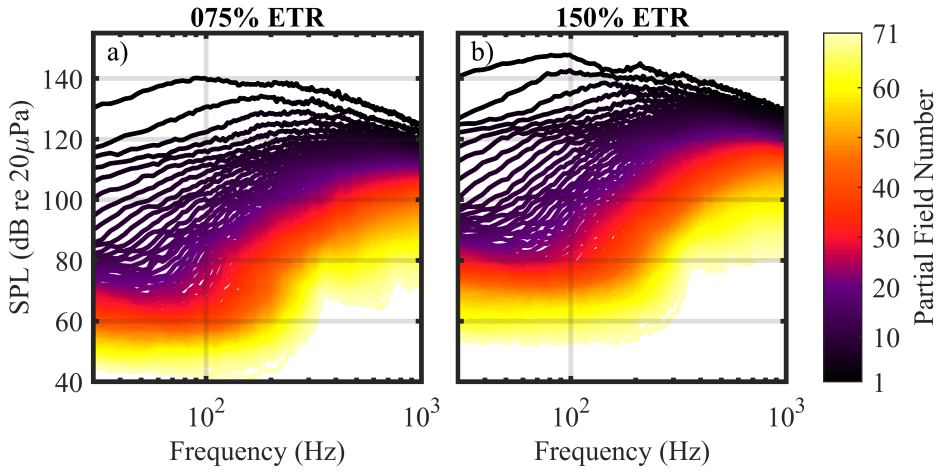

Figure 2.4 Singular values of the 71 partial fields as a function of frequency for a) 75% and b) 150% ETR.

of partial fields used was selected such that their sum represented 99.9% of the total energy of the input hologram. Over the frequency band presented in this paper, only four partial fields were needed to meet this energy criteria for the lowest frequencies and on the order of 50 for the highest frequencies. Because the excluded partial fields generally had higher relative amplitudes towards the edges of the array, the 0.1% of energy removed generally causes the field at the edges of the array to be slightly underestimated.

2.4.3 Numerically extrapolate each partial field beyond the measurement aperture

The SONAH algorithm was originally developed to reduce errors caused by having a measurement aperture that was not significantly larger than the source [93]. Even with the SONAH algorithm, in this measurement the 32 m aperture was not large enough to capture all the pertinent energy for the lowest frequencies, causing finite-aperture effects to become significant. The two most significant finite-aperture effects in this work are wraparound error and high-wavenumber leakage. Wraparound error is solved easily by zero-padding the edges of the input hologram so that it is much

larger than the area in which the reconstructions are made. High-wavenumber leakage is caused by pressure discontinuities in the input, which in turn are caused by the pressures not decaying to zero by the edges of the hologram. In an attempt to simulate the missing energy from having a too-small aperture at low frequencies and to reduce the discontinuity at the measurement edge, linear forward prediction was implemented to estimate values for the complex pressures of the field at locations beyond the original measurement aperture and a window was applied to the extended measurement to reduce the pressures to zero by the edge.

In linear forward prediction, the coefficients of a polynomial are determined from existing data, the polynomial is used to predict one point beyond the original aperture, which is then included in the fitting of a new polynomial. This process is iterated until the field is extended the desired amount. This method has been used for previous studies [95] and is repeated here for simplicity. A challenge with extending the aperture of each partial field individually is that the SVD-based PFD may generate partial fields which do not monotonically decrease towards the end of the original measurement. In such cases, the linear forward prediction (which has a tendency to produce extraneous oscillations [95]) of the higher-order partial fields (which via the SVD are inherently less energetic than the lower-order partial fields) often end up contributing more to the energy of the extended field than the lower-order partial fields. This causes the extended field to only be accurate for short distances outside of the original measurement. To enforce a graceful taper of the pressures to zero at the end of the extended aperture and reduce the effect of extraneous oscillations outside the original measurement, a Tukey window is applied to the magnitude of the complex pressures along the extended hologram. The window has a value of one over the original measurement that decays to a value of zero within one acoustic wavelength of the edge of original measurement. Extending the aperture with the window provides zero padding as well. For this measurement geometry, the aperture is extended approximately 68 m on either side of the array, which is needed to eliminate wraparound error for as low as 32 Hz.

2.4.4 Formulate the EWM of the jet in the run-up pad environment and solve for pressure at desired reconstruction locations

The EWM methodology used in the M-SONAH algorithm is described in detail in Refs. [82, 83]. For this study, the EWM is comprised of two sets of cylindrical wave functions to capture the effect of the rigid ground on the measurement, one centered along the jet centerline and another along an image jet centerline below the ground. The basis functions for outward propagation are

$$\Psi_{l,k_z}(\vec{r}) \equiv \frac{H_l^1(k_r r)}{H_l^1(k_r r_0)} e^{il\phi} e^{ik_z z},\ r \geq r_0 \tag{2.1}$$

where r, ϕ, and z are the radial, azimuthal, and axial spatial coordinates of the position vector, $\vec{r}$; H_l^1 is the lth-order Hankel function of the first kind; i is the imaginary unit; r_0 is some small reference radius (traditionally the assumed source radius) [96]; and k_z and k_r are the axial and radial wavenumbers, respectively. For this study, only $l = 0$ is used, since a single, ground-based linear array is used as the input. This choice of l forces axisymmetry for each wavefunction at each frequency. This limitation is sufficient to reconstruct the sound field over a limited azimuthal aperture, as exemplified by the success of prior work [83], where a large two-dimensional array was used as input but only the zeroth-order mode was needed for accurate reconstructions. The success of limiting the equivalent wave model to $l = 0$ is likely due to the reconstructions only being attempted at sufficiently low frequencies.

The number of wavefunctions in each set, M, is therefore only dependent on the number of k_z values used. The k_z values for this study are regularly spaced between $-\frac{\pi}{\mathrm{d}z}$ and $\frac{\pi}{\mathrm{d}z}$ in steps of $\frac{\pi}{\Delta z}$, where $\mathrm{d}z$ is the interelement spacing along the array in z and Δz is the total axial span of the array. The radial wavenumbers are

$$k_r = \begin{cases} \sqrt{k^2 - k_z^2} & \text{for } |k| \geq |k_z|, \\ i\sqrt{k_z^2 - k^2} & \text{for } |k| < |k_z|, \end{cases} \tag{2.2}$$

where $k = \frac{\omega}{c}$ is the acoustic wavenumber, ω is the angular frequency, and c is the speed of sound. This choice for wave function and definition of k implies a time harmonicity of $e^{-i\omega t}$.

The basis functions in Eq. 2.1 depend on a position vector $\vec{r} = (r, \phi, z)$, which is expressed relative to the above-ground jet centerline (superscript ^{1}) or the image jet centerline below the ground (superscript ^{2}) via Eqs. 2.3 and 2.4,

$$\vec{r}^1 = \left(\sqrt{x^2 + (y-2)^2}, \tan^{-1}\left(\frac{y-2}{x}\right), z \right) \tag{2.3}$$

$$\vec{r}^2 = \left(\sqrt{x^2 + (y+2)^2}, \tan^{-1}\left(\frac{y+2}{x}\right), z \right), \tag{2.4}$$

using the Cartesian coordinates of Fig. 2.1. The notation $\vec{r}_{hi}$ is now used to represent the position vector of the i^{th} point on the holography array (which has N_h points), and $\vec{r}_{q_i}$ represents the position vector of the i^{th} of N_q points on the reconstruction array.

The total EWM is now created by evaluating all the basis functions at each measurement point and each reconstruction point. They are combined into the matrices

$$\mathbf{A} = \begin{pmatrix} \Psi_{k_{z1}}(\vec{r}_{h1}^{\,1}) & \dots & \Psi_{k_{z1}}(\vec{r}_{hN_h}^{\,1}) \\ \vdots & \ddots & \vdots \\ \Psi_{k_{zM}}(\vec{r}_{h1}^{\,1}) & \dots & \Psi_{k_{zM}}(\vec{r}_{hN_h}^{\,1}) \\ \Psi_{k_{z1}}(\vec{r}_{h1}^{\,2}) & \dots & \Psi_{k_{z1}}(\vec{r}_{hN_h}^{\,2}) \\ \vdots & \ddots & \vdots \\ \Psi_{k_{zM}}(\vec{r}_{h1}^{\,2}) & \dots & \Psi_{k_{zM}}(\vec{r}_{hN_h}^{\,2}) \end{pmatrix} \tag{2.5}$$

and

$$\alpha = \begin{pmatrix} \Psi_{k_{z1}}(\vec{r}_{q1}^{\,1}) & \dots & \Psi_{k_{z1}}(\vec{r}_{qN_q}^{\,1}) \\ \vdots & \ddots & \vdots \\ \Psi_{k_{zM}}(\vec{r}_{q1}^{\,1}) & \dots & \Psi_{k_{zM}}(\vec{r}_{qN_q}^{\,1}) \\ \Psi_{k_{z1}}(\vec{r}_{q1}^{\,2}) & \dots & \Psi_{k_{z1}}(\vec{r}_{qN_q}^{\,2}) \\ \vdots & \ddots & \vdots \\ \Psi_{k_{zM}}(\vec{r}_{q1}^{\,2}) & \dots & \Psi_{k_{zM}}(\vec{r}_{qN_q}^{\,2}) \end{pmatrix}, \tag{2.6}$$

where the number of rows in $\mathbf{A}$ is equal to the number of wavefunctions used in the model (twice the M discrete k_z values), and the number of rows is equal to the N_h measurement points on the hologram. The $\boldsymbol{\alpha}$ martrix has the same number of rows as $\mathbf{A}$, but with columns equal to the N_q number of points in the array where the field is to be reconstructed.

At this point, the M-SONAH process is the same as SONAH [93], where the column vector of pressures at all the reconstruction locations, $\mathbf{p}_q$, is given in terms of the column vector of pressures at each point of the hologram, $\mathbf{p}_h$, as

$$\mathbf{p}_q^{\mathrm{T}} = \mathbf{p}_h^{\mathrm{T}} \mathbf{R}_{\mathbf{A}^{\mathrm{H}}\mathbf{A}} \mathbf{A}^{\mathrm{H}} \boldsymbol{\alpha}, \tag{2.7}$$

where the superscript T is the transpose, the superscript H is the Hermitian transpose, and $\mathbf{R}_{\mathbf{A}^{\mathrm{H}}\mathbf{A}}$ is the regularized inverse of $\mathbf{A}^{\mathrm{H}}\mathbf{A}$. Regularization was performed using a modified Tikhonov filter with the generalized cross validation procedure for the selection of the regularization parameter as outlined in Ref. [97]. The reconstructed pressures for each partial field are then energetically summed to obtain the final answer for each frequency. All levels shown in this paper for specific frequencies are scaled as if these frequencies were extracted from an autospectrum with units of Pa^2.

2.5 Results and Discussion

This section shows the reconstructed field in the area surrounding the aircraft. In Section 2.5.1, the field is reconstructed along the holography array to verify the spatial and frequency regions where reliable reconstructions are obtained. Section 2.5.2 contains reconstructions to the two dimensional plane along the ground surrounding the aircraft as well as comparisons of reconstructions to the measured field along the 38 m arc. Section 2.5.3 has the reconstructions that were made along the nozzle lipline of the jet to give insight into acoustic source characteristics of the jet plume. Section 2.5.4 shows reconstructions made to the field in the region to the side of the aircraft to characterize BBSAN directivity and source location. In Section 2.5.4, the region of maximum radiation in the aft direction is examined and the field sound level maps are used to characterize the behavior of the multiple spatiospectral lobes across frequency and engine power. Finally, Section 2.5.5 compares these results to previous studies of similar military aircraft as well as a numerical simulation of a heated laboratory-scale jet.

2.5.1 Reconstructions at the Hologram

To verify the frequency range in which the aperture and interelement spacing of the array are sufficient, field reconstructions are made at the input array and compared to the measured data. The difference between the reconstructed and measured fields are displayed in Fig. 2.5 for two engine conditions: an intermediate condition (75% ETR) and the maximum afterburning condition (150% ETR). The largest errors in the reconstruction occur at low frequencies, where the method overestimates the field level, and at high frequencies (above 400 Hz) where the levels are underestimated. The low-frequency errors are attributed to the array not being large enough to fully capture all the pertinent energy in the field. The high-frequency underestimations are due to spatial aliasing, where the trace wavelength of the noise along the array is smaller than twice the interelement spacing

in the array. The spatial aliasing at frequencies above 400 Hz causes a reallocation of energy to a non-physical lobe which starts far downstream and propagates upstream. This reallocation of energy is manifest as an immediate drop in level at about 400 Hz for $z > 10$ m. The upstream region ($z < 10$ m, where BBSAN is dominant) maintains a smaller error for frequencies above 400 Hz until the aliased lobe causes an overestimation of the levels there (particularly at 75% ETR). Based on these limitations, investigations into the directivity of the aft radiation lobes are only conducted for frequencies less than 400 Hz.

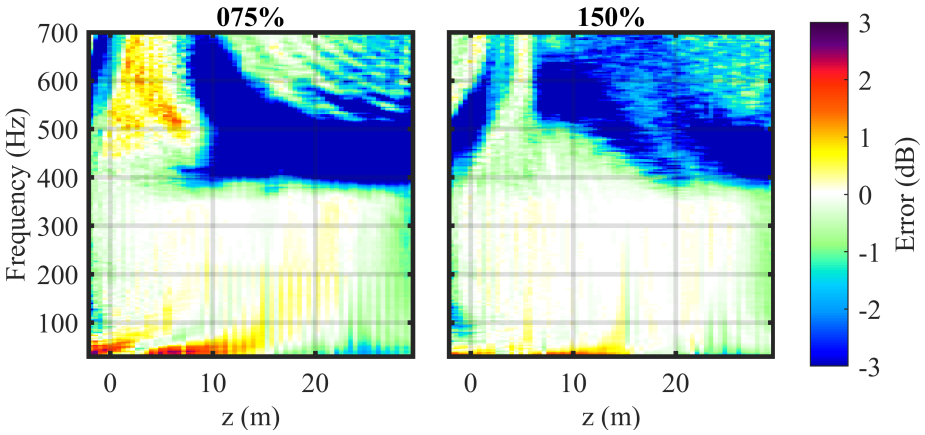

Figure 2.5 Error of the M-SONAH reconstruction along the input holography array as a function of frequency for two engine conditions, 75% and 150% ETR.

2.5.2 Field Reconstructions

The benefit of the holography process is its ability to reconstruct the field at arbitrary locations, which gives a physics-based extrapolation of the field to a myriad of points that would be impractical to measure. Figure 2.6 shows reconstructions of the field to points in the ground plane ($y = 0$) for two representative frequencies and engine conditions. The top row corresponds to 162 Hz and the bottom row to 354 Hz. The columns represent two engine conditions, on the left, an intermediate condition (75% ETR) and on the right, the maximum afterburning condition (150% ETR). The color contour maps show the reconstructed sound pressure level at each point, the white

line is the holography array location, and the gray outline is the aircraft position. In general, the reconstructions show field trends expected for jet noise, with the maximum radiation beaming at a large aft angle. However, the most apparent features at these frequencies are the multiple radiation lobes. At 75% ETR and 162 Hz, two lobes are present with distinct directivities and apparent source locations; at the same frequency but 150% ETR, the lobes rotate to a more forward directivity, have a higher level, and overlap more. The same trend (though less clear) can be seen at 354 Hz.

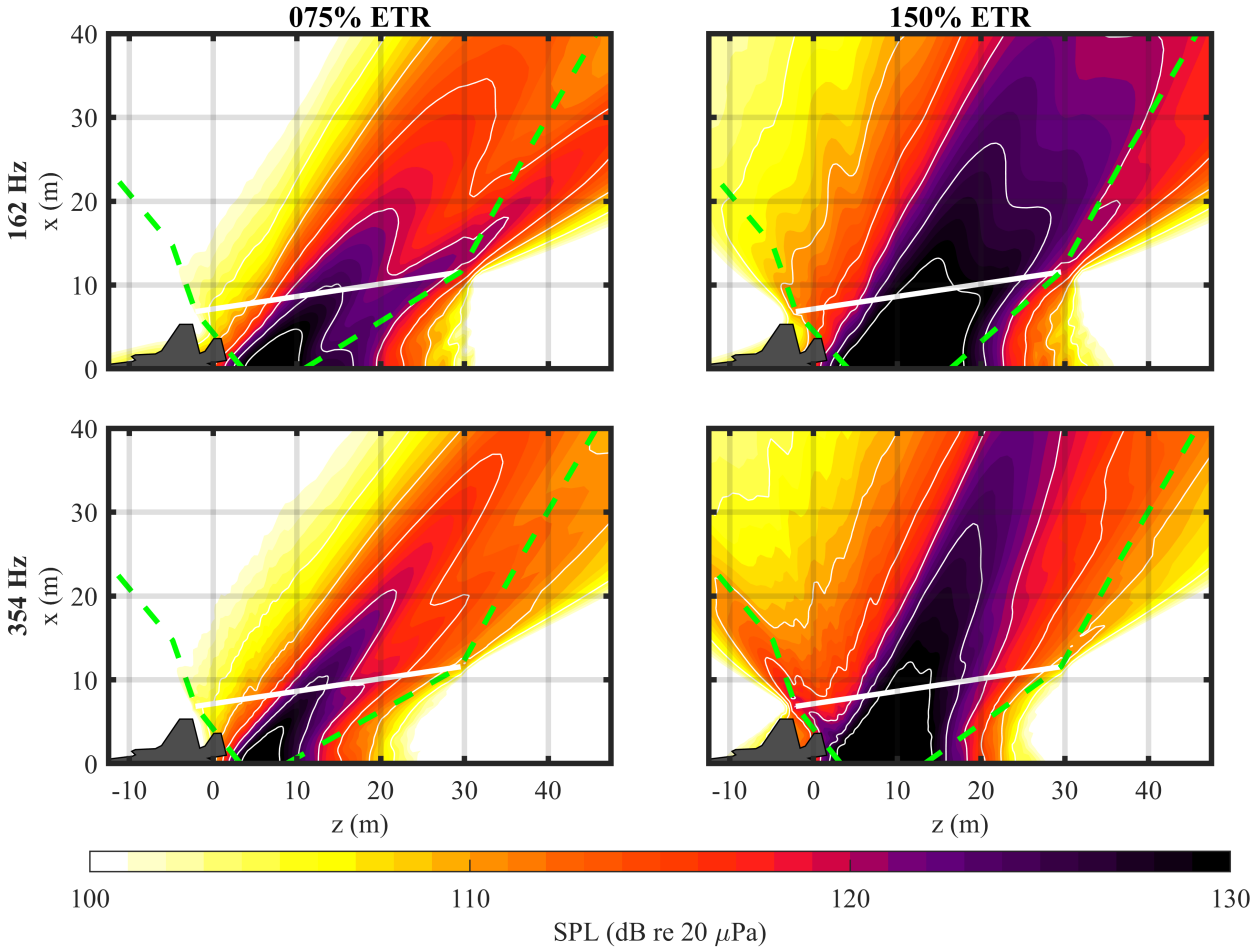

Figure 2.6 Reconstructions along the $y = 0$ plane at two frequencies and engine conditions. The colored contour plots show the sound pressure level maps, the thick white line is the location of the input holography array, and the region between the green dashed lines represent where errors are expected to be less than 2 dB.

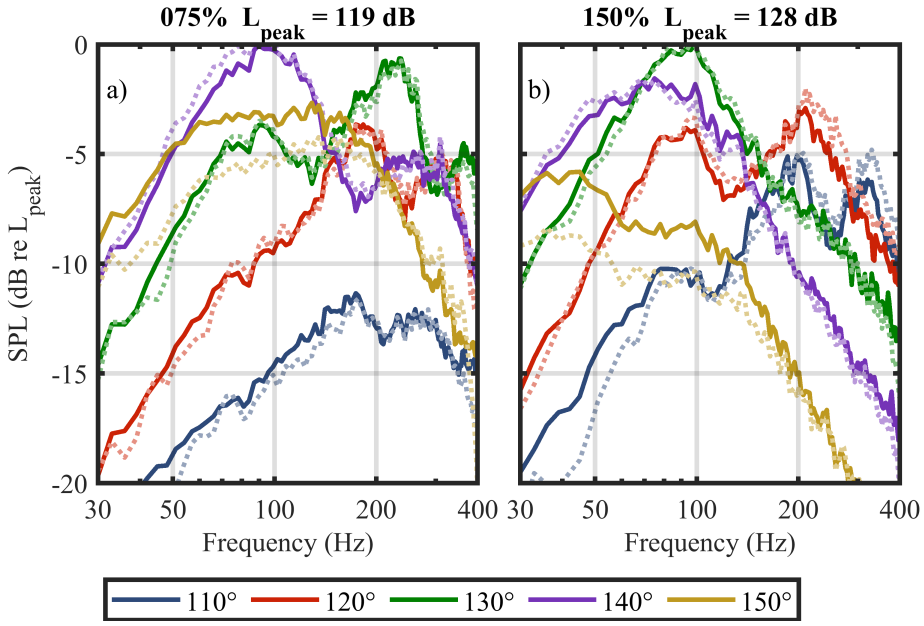

Figure 2.7 Select spectra along the 38m arc at five polar angles and two engine conditions. Dotted lines are M-SONAH reconstructions

To be able to characterize the directivity of the multiple lobes across frequency and engine power, it is important to understand the spatial limitation of accurate field reconstructions. Though not shown in Fig, 2.1, the F-35 measurement contained a number of arrays in the field, including arcs with radii of 19, 29, 38 and 76 m as well as additional line arrays in front of and just behind the holography array. A previous study [98] compared M-SONAH reconstructions to the measurements at these arrays and found errors were less than 2 dB between $\theta = 50°$ and $\theta = 150°$. Further investigation of the artifacts of the M-SONAH procedure was done using a numerical simulation. A numerical source was created along the jet centerline, the M-SONAH procedure was applied to an input hologram (same spatial location as the F-35 measurements), and field reconstructions of the numerical source were compared to the numerical field. The 2 dB error contours of this numerical case are used in conjunction with the error of the M-SONAH reconstructions to all the measurements in the region to determine a conservative estimate of a region of good fit for the frequencies of interest in this paper. The boundary of the good-fit region is represented by the

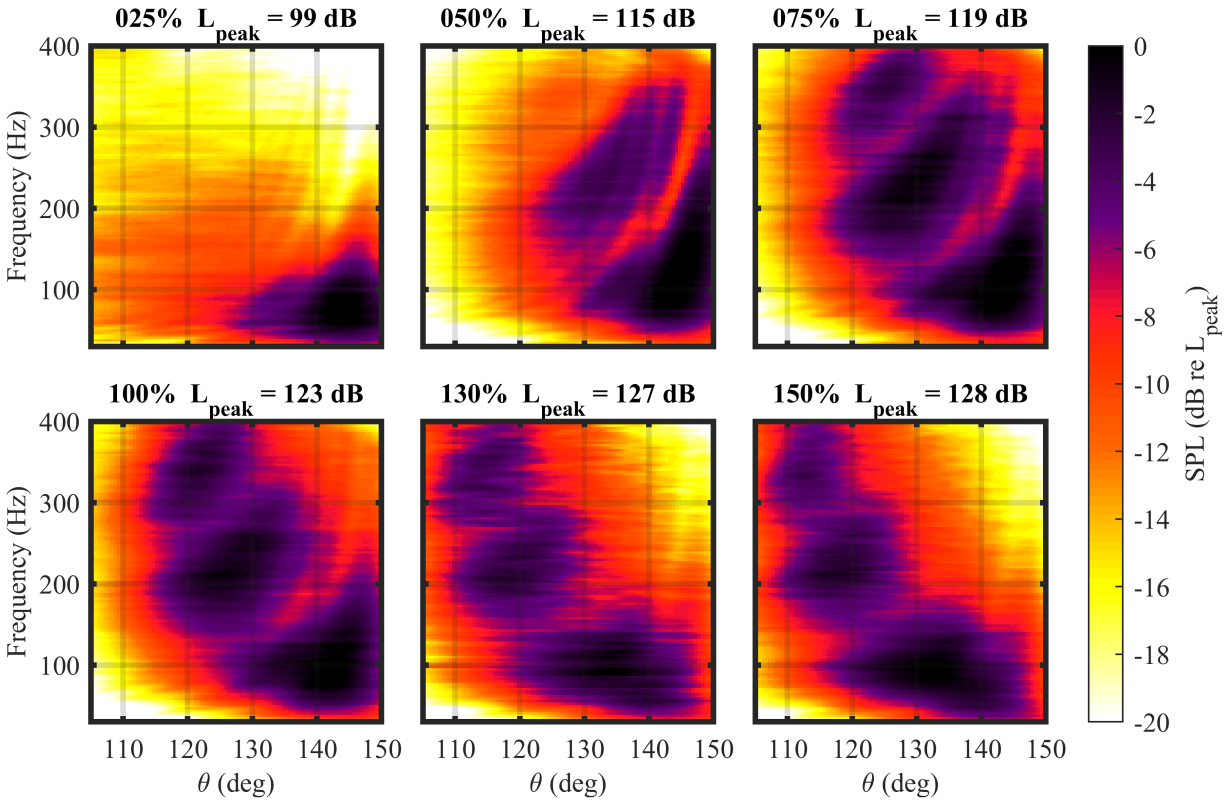

Figure 2.8 Reconstructed spatiospectral maps along the 38 m arc in the same format as Fig. 2.3

dashed green lines in Fig. 2.6. A line is drawn from the edges of the holography array outward to select microphone positions at the 19, 38, and 76 m arcs. Upstream of the main radiation lobe, the boundary points are chosen as $\theta = 50°$ for the 19, 38, and 76 m arcs; Downstream of the main radiation lobe, $\theta = 140°$ for the 38 m arc and $\theta = 130°$ for the 76 m arc. These lines are continued from the edges of the holography array inward to the nozzle lipline to the spatial region that contains the top 6 dB of reconstructed levels at each frequency (represented by the solid green lines in Fig. 2.9).

The accuracy of the outward reconstructions is confirmed by comparing reconstructions to measured spectra along the 38 m arc. Figure 2.7 shows five spectra measured at 110°, 120°,

130°, 140°, and 150° at two engine conditions, along with the M-SONAH reconstructions at the corresponding measurement locations (dotted lines). The spectra are limited between 30-400 Hz and normalized to the peak of the spatiospectral domain (similar to Fig. 2.3). Though the measurement was taken at 5 feet off the ground, the multi-peaked spectra observed at all engine conditions are not attributed to ground reflection interference nulls. Because of the large distance of the array from the jet, the lowest frequency where ground reflection nulls for even an infinitely long cylindrical source at the jet centerline is calculated to be above 400 Hz. Reconstructions follow the measured spectra closely except for frequencies below 150 Hz at the 150° location, where the reconstructions underestimate the levels, likely due to the limitations in the aperture extension procedure.

To provide a more complete view of the aft radiation, holographic reconstructions to a dense grid along the 38 m arc are shown in Fig. 2.8 in the same format as Fig. 2.3, with the exception that the horizontal axis is now the jet inlet angle, θ. The M-SONAH reconstructions appear to interpolate between the measured spectra in Fig. 2.7 and show up to three clearly defined spatiospectral lobes in this frequency range.

2.5.3 Source Reconstructions

M-SONAH reconstructions at the nozzle lipline for the F-35B (along the line at $x = 0.5$ m, $y = 2.0$ m) can provide insight into source characteristics. Spatiospectral reconstructions to the nozzle lipline are displayed in Fig. 2.9, which is in the same format as Fig. 2.3. Each pane represents the reconstructions between 30 Hz and 700 Hz at each point along the lipline. The green contour lines represent the spatial region where the levels are within 6 dB of the maxima at that frequency. For a given engine condition, the peak region of the source contracts in size and shifts upstream with frequency, which is well-documented for subsonic [7] and supersonic [99,100] jet noise at laboratory scales. However, like previous studies of tactical aircraft [75,83], there are some deviations in the source distributions. At 25% ETR between 200-400 Hz there seems to be two spatially separated

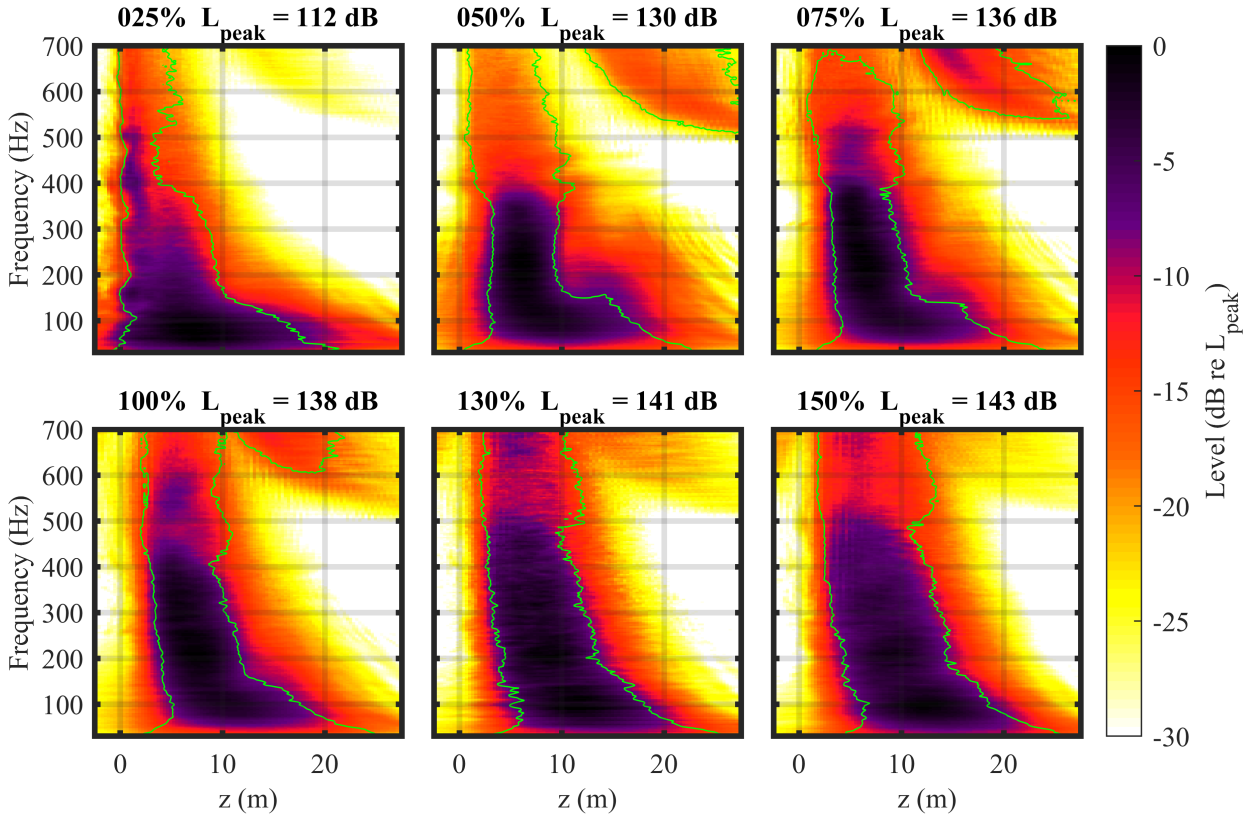

Figure 2.9 Spatiospectral maps of M-SONAH reconstructions along the nozzle lipline. The solid green contour represents the 6 dB-down region for each frequency, which is the intersection of the green dashed lines in Fig. 2.6 with the nozzle lipline.

local maxima. The upstream maximum is possibly an attempt by the algorithm to reconstruct the engine noise, while the other likely the reconstruction of the aeroacoustic noise, with lower frequencies dominated by aeroacoustic noise and higher frequencies dominated by engine noise. Spatiospectral lobes are seen at 50% ETR and above that follow similar patterns as seen in Fig. 2.3. At 50% ETR and 75% ETR though, instead of discrete lobes as seen in Fig. 2.3 it appears as more of a continuous L-shaped region. At 130% ETR and 150% ETR, however, the spatiospectral levels in Fig. 2.9 start to mimic the measured data at the input array and split into separate lobes similar to those in Fig. 2.3.

As previously mentioned, spatial aliasing starts to appear in the field reconstructions at 400 Hz. Even though an aliased lobe does not appear at the lipline until above 500 Hz, at 50%, 75%, and 100% ETR there is an enlargement of the marked 6 dB-down region between 400 and 500 Hz. The enlargement is probably due to the spatial aliasing, as it does not follow trends measured from similar full-scale military aircraft [75].

2.5.4 Multiple Lobe Tracing

The multiple radiation lobes can now be tracked across space because of the holographic projection of the field between measurement arrays. First, the field was reconstructed to a dense polar grid (with the MARP as the origin) along the ground plane in the vicinity of the aircraft. This projection onto the ground plane provides an approximation of the lobes that would be found in a free-field analysis (lobe tracing at the jet centerline height with no ground interference effects). Examples of these field reconstructions are seen in Fig. 2.6. To capture trends of the multiple spatiospectral lobes across frequency and engine power, lines were fit in the *z*-*x* plane to each of the spatial lobes at each frequency, similar to laboratory-scale work where the field could be measured directly [101]. To trace the lobes, points of local maxima were selected along each radius of the dense polar grid programmatically. Several local maxima were seen at each arc due to the multiple radiation lobes in the aft direction, the BBSAN noise lobe in the forward direction, and noise in the reconstruction. To identify which points correspond to spatiospectral lobes, these points were then overlaid over plots of the complete field reconstructions such as in Fig. 2.6 to see them in context. Each plot for every frequency and engine power combination was then viewed to manually select which points were representative of each directivity lobe in the field. Lines in the *z* -*x* plane were then least-squares fit to each group of selected points to create a line to represent each directivity lobe. This resulted in a set of lines which represent specific directivity lobes at individual frequencies.

The lines with a positive slope (representing a spatial lobe with aft directivity) for each frequency were then associated with each of the spatiospectral lobes as numbered in Fig. 2.3. This association was done by calculating the intersection point of each line with the holography array and superimposing those points on Fig. 2.3. Each point (representing a traced line at a single frequency) was then manually assigned to one of the numbered spatiospectral lobes. This process contains some ambiguity in that sometimes more than one spatial local maximum at a single frequency appears to be a part of a single spatiospectral lobe as numbered in this paper. This suggests that the spatiospectral lobes as numbered in Fig. 2.3 are in fact not capturing all the physical phenomena present. However, for the purposes of this paper, these smaller fluctuations are ignored. Further analyses to quantitatively isolate finer patterns than the several lobes discussed in this paper (such as coherence analyses [61]) are ongoing.

The slope and z- intercept of each line now give information about the directivity and apparent source location of each spatiospectral lobe and can be tracked as a function of frequency and engine power. This procedure for tracking the spatiospectral lobes is used in Section 2.5.4 to discuss the trends of the BBSAN lobe in the upstream direction and the multiple radiation lobes in the aft direction.

BBSAN Trends

Broadband shock-associated noise (BBSAN) has been explored in much more detail in the jet noise literature than the spatiospectral lobes radiating in the aft direction. The characteristic spatiospectral signature can be seen along the holography array (Fig. 2.3) for 75%, 100%, 130%, and 150% ETR between 400 Hz and 700 Hz at $z < 7$ m. M-SONAH reconstructions of the field show BBSAN as a lobe radiating upstream. Figure 2.10 shows M-SONAH reconstructions along the ground plane at two representative frequencies from 75% to 150% ETR. At 450 Hz, there is little evidence of BBSAN at 75% ETR, but it quickly strengthens as engine condition increases. At 549 Hz, BBSAN

is apparent at 75% ETR and increases in strength up to 150% ETR. The lines fitted to the BBSAN lobes are superimposed on Fig. 2.10 in dark blue.

The reconstructions at frequencies above 400 Hz (as shown in Fig. 2.10) are considerably noisier than low-frequency reconstructions seen in Fig. 2.6. This noise arises during the regularization step in the inversion of $\mathbf{A}^{\mathrm{H}}\mathbf{A}$, which becomes more difficult as frequency increases (particularly above the Nyquist frequency when aliasing is present). A more stringent choice of regularization parameter significantly smooths out the field but also causes the level to be severely underestimated. The parameter used here was chosen to favor accuracy in level.

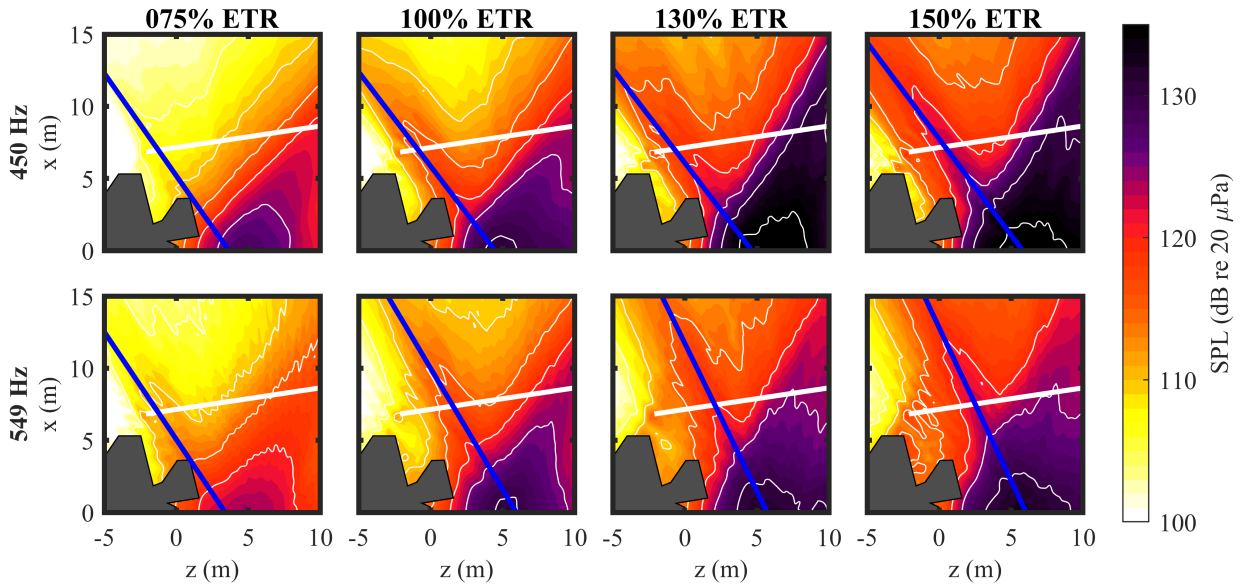

Figure 2.10 Reconstructions along the ground plane of the region towards the side of the aircraft where BBSAN is apparent.

To track the BBSAN lobe characteristics across frequency and engine condition, Fig. 2.11 shows the directivity angle and z-intercept of lines fitted to the BBSAN lobe for several engine conditions. Little variation across engine condition is seen, except for the z-intercept at 75% ETR. The BBSAN at this engine power is low in level and appears at the edge of the holography array as seen in Figs. 2.3 and 2.10. The low prominence of the BBSAN lobe and incomplete coverage by the array likely

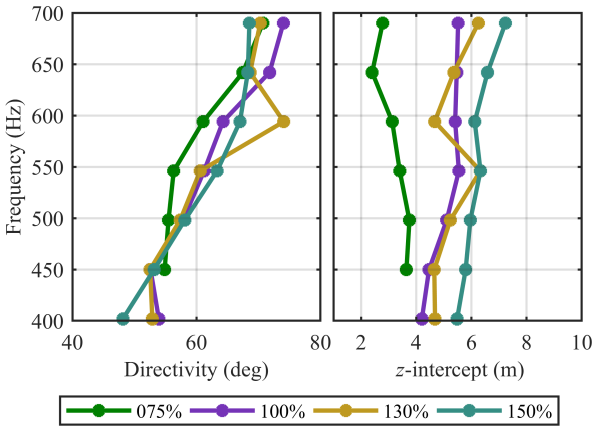

Figure 2.11 Directivity and z-intercept of line traced through the BBSAN lobe for four engine conditions

causes the fitted line to be less accurate than at higher engine powers, where the BBSAN lobe is fully captured. For all engine conditions, however, the placement of the origin of BBSAN in Fig. 2.11 is within the 6 dB down region seen in Fig. 2.9. The directivity angle of BBSAN noise increases with frequency across all engine conditions, which is consistent with laboratory-scale overexpanded jets [18], as well as conclusions for this aircraft by Ref. [58].

Mixing Noise Trends

The trends of the aft spatiospectral lobes across frequency and engine condition are summarized by Figs. 2.12 and 2.13. Figure 2.12 shows M-SONAH reconstructions in the same format as Fig. 2.6 but including more engine conditions, frequencies, and the lines that were traced through the multiple spatiospectral lobes. These lines are color-coded to correspond with the spatiospectral lobe numbers from Fig. 2.3: lobe 1 is blue, lobe 2 is green, and lobe 3 is orange. At a fixed engine condition, when frequency is increased, the lobes swing aft until they leave the aperture of the array. While that happens, new lobe(s) appear upstream and then swing aft as well. When each new lobe

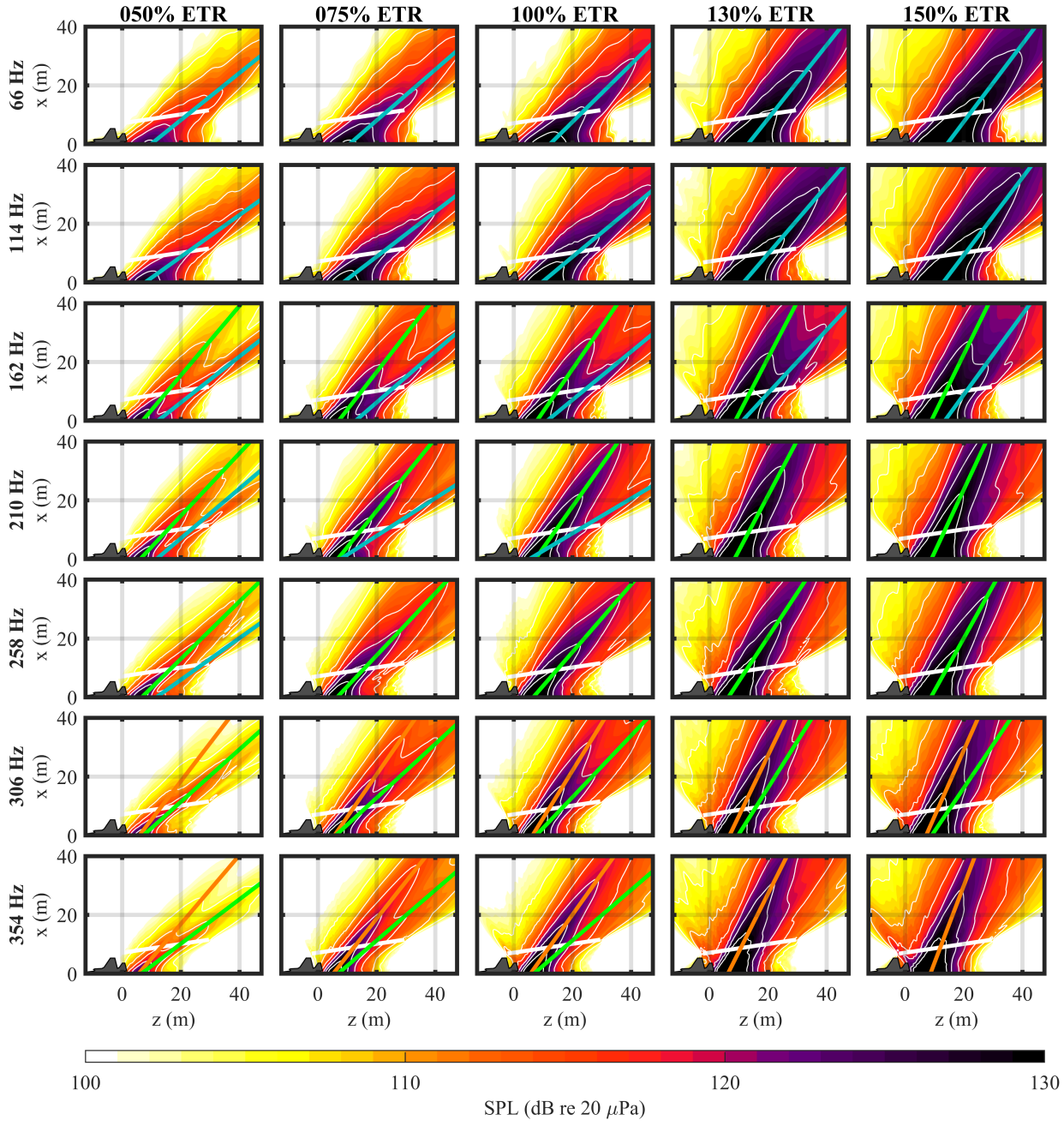

Figure 2.12 M-SONAH reconstructions along the $y = 0$ plane for several frequencies and engine conditions. The blue, green, and orange lines represent the lines fitted to the spatial lobes corresponding to spatiospectral lobes 1, 2 and 3 from Fig. 2.3.

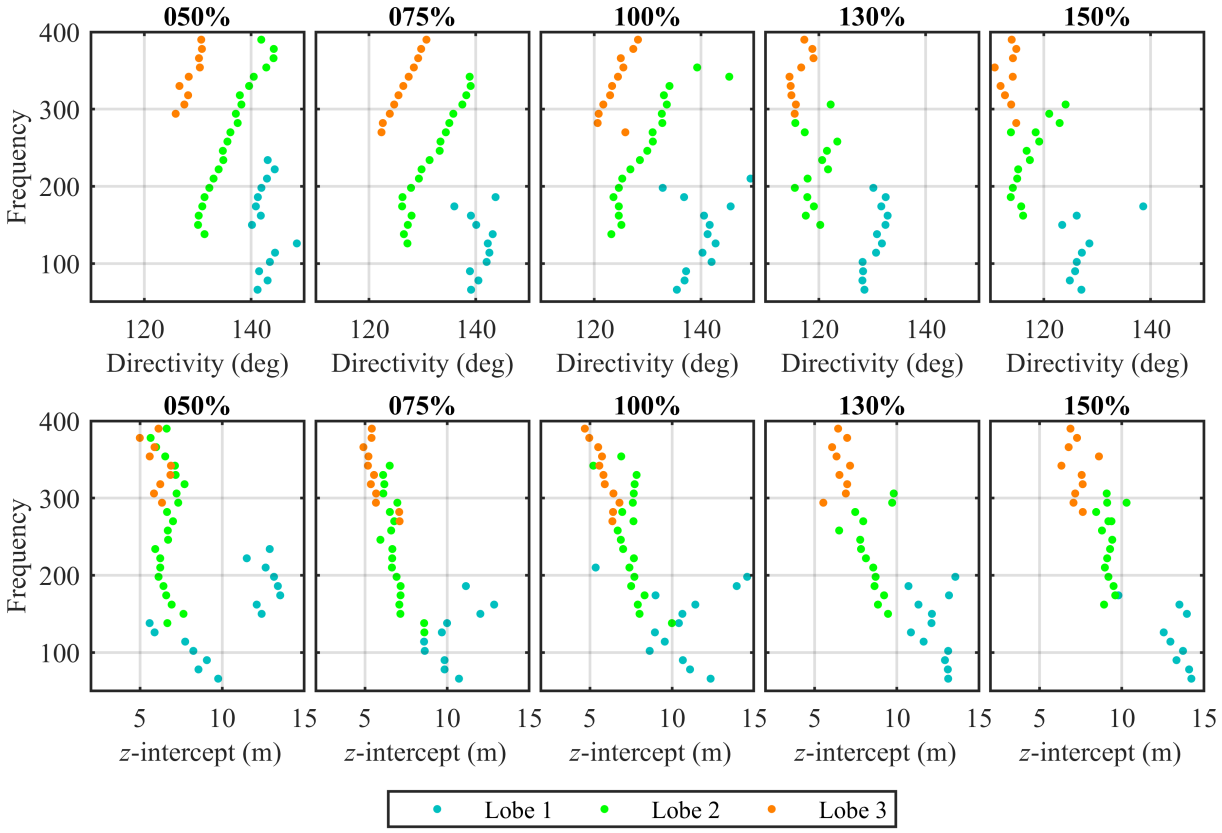

Figure 2.13 Directivity angle (top row) and z-intercept (bottom row) of the lines fitted through each of the spatial radiation lobes seen in the M-SONAH reconstructions.

appears, it starts at a low amplitude, grows to a peak in the maximum radiation direction of the overall field, and then decays as it continues to swing aft and out of the aperture of the array.

For a given frequency, lobes increase in level for higher engine conditions and their directivity angle decreases, consistent with an increasing convective Mach number of the jet. Additionally, whichever lobe originates closest to the nozzle increases in level more than the others do, thus increasing its relative contribution to the overall field. As with the discussion of Fig. 2.2 and Fig. 2.3, it appears that the increasing contribution of the forward-most lobe is the driving factor in the change of overall directivity as engine condition increases, especially in the transition from 50% ETR to 75% ETR.

As was done for the BBSAN lobe, lines were fit to each lobe which defines them by two parameters: the slope and the z-intercept. The slope of the line can be expressed in terms of the jet inlet angle, giving a measure of directivity for that lobe. The z-intercept of the line gives an approximation to the acoustic source region corresponding to that lobe. The directivities and z-intercepts in Fig. 2.13 came from lines that were fitted to every spatial lobe between 60 and 400 Hz. At 60 Hz, lobe 1 (blue) begins with an aft directivity and downstream source location. As frequency increases, the directivity and z-intercept tend to increase, though there appears to be some clustering of the points suggesting that lobe 1, as identified in Fig. 2.3, is probably a superposition of two lobes that are not entirely separable when looking at level alone. Coherence analyses in Ref. [61] corroborate this conclusion. Lobe 2 (green) has a source region between 5 m and 10 m downstream that does not change drastically with frequency but consistently shifts downstream with increasing engine condition. The directivity angle increases with increase in frequency, with as much as a 15° increase for 50% and 75% ETR from 150 to 400 Hz. At 130% and 150% ETR, the change in directivity across frequency is less. Lobe 3 (orange) first appears at a higher frequency than the other two lobes and has similar trends as lobe 2. Lobes 2 and 3 share similar z-intercepts as the BBSAN lobe seen in Fig. 2.11. As engine power increases, the z-intercepts for all lobes are

shifted farther downstream and the directivities shift towards the sideline. In most cases, the lines representing the several lobes stay in the same ordering relative to each other — lobe 1 remains the farthest downstream with lobe 3 being the farthest upstream.

2.5.5 Comparison With Other Studies

The spatiospectral lobe trends discussed in this work have been partially observed by several studies in recent years. Harker *et al*. [60] show one-third octave band spectra for pressures measured by a ground-based linear array parallel to the jet centerline of a tied-down high-performance military aircraft with a rectangular nozzle. Figure 2 of that paper displays the OASPL and spectra as a function of distance downstream from the nozzle, similar to Figs. 2.2 and 2.3 of this paper. At least two spatiospectral lobes are apparent at the afterburning engine condition, with the first centered at about 100 Hz and 17 m downstream of the nozzle and the second centered at 250 Hz and about 10 m. Acoustic intensity vectors measured in the vicinity of that same aircraft are reported in Refs. [102] and [103]. A video (Mm. 1.) attached to Ref. [102] shows a vector intensity map which changes as a function of frequency. At low frequency, the intensity vectors show a large aft directivity with apparent source region far downstream. As frequency increases, the vectors measured nearer to the nozzle grow in level relative to the far aft intensity vectors, while all vectors slightly rotate aft. This pattern is again recorded in Fig. 12 of Ref. [103] where the angular span of the top 3 dB of intensity vectors is plotted as a function of frequency. The top 3 dB region of the radiation points far aft at low frequency, then, as frequency increases, the angles jump upstream, shift downstream, then jump upstream again. This general pattern is the same as is observed in the columns of Fig. 2.12 in the current work; as frequency increases, new lobes appear upstream and grow in strength as the farther aft lobes decay and shift out of the measurement aperture.

A recent measurement of the T-7A trainer aircraft [89] with an expansive near-field array identified spatiospectral lobes in military, afterburner, and two intermediate conditions with qualitatively

similar patterns across frequency and engine power as those discussed here. Similarity in the spatiospectral domain of the F-35, the T-7A, and the aircraft measured in Ref. [54] suggests that with some frequency or velocity scaling they could potentially collapse into self-similar behavior. For most military aircraft, however, flow parameters are not disclosed, thus rendering this type of analysis difficult.

Another look at the multiple lobes in the one-third octave band spectra of the same aircraft in Refs. [54, 57, 60, 83] was performed by Tam and Parrish [59], who attempted to fit large-scale turbulent structure similarity spectra to the spectra published in Ref. [57]. Tam and Parrish [59] identify two "new" noise components associated to regions in the measured spectra that do not fit the ad-hoc similarity spectrum they derived specifically for that study. For the first, this similarity spectrum was fit to the lower of the two peaks in the measured spectrum at an inlet angle of 115° and the higher-frequency component was deemed to be a new noise source (see Fig. 22 of Ref. [59]). For the second new noise source, the similarity spectrum was fit to the higher-frequency peak at an inlet angle of 150° and the extra low-frequency content is called a new source (see Fig. 29). These two new noise sources are then identified as "fast wave indirect combustion noise" and "slow wave indirect combustion noise". If that aircraft under investigation has a similar spatiospectral structure as the F-35B, then it would appear that the authors are attempting to fit the similarity spectrum to lobe 2, and are calling lobe 3 "fast wave indirect combustion noise" and lobe 1 "slow wave indirect combustion noise". Because of the high-resolution measurements provided by the current study, it is clearly seen that lobes exist across multiple engine conditions, regardless of the presence of afterburner.

In previous laboratory-scale investigations of jets exhausting over rigid surfaces [62–67], an additional peak in the spectrum was observed below the peak frequency of the jet noise and was attributed to the interaction of the jet with the surface. For cases where the surface was smaller than the extent of the plume, the noise source was found to be the scattering of the jet off the edge of the

surface. In cases where the surfaces were larger than the extent of the plume and were meant to represent a rigid ground, low-frequency amplification is observed in the far aft beyond inlet angles of 150° [62, 63]. It is noted that lobe 1 as labelled in the current work is situated below the peak frequency of the jet noise from this aircraft and is found in this far aft region. It is therefore possible that jet-ground interactions could be a contributing effect. For example, there are a few cases in Fig. 2.13 where the directivity and source location of lobe 1 does not follow the same trends as the other lobes (particularly apparent at 50% ETR). It may be that at these low frequencies jet noise and jet-ground interaction noise are superimposed, thus corrupting the field reconstructions. Further work is needed to understand the effect of the ground on the low-frequency component of military aircraft jet noise.

In an attempt to shed light on the origin of multiple radiation lobes, Liu *et al*. [39] used the JENRE® large eddy simulation solver developed at the Naval Research Laboratory to simulate a supersonic jet at a temperature of 2100 K (total temperature ratio of 7), which is comparable to operating conditions of high-performance jet engine exhaust at afterburner. Figure 21 a) of Ref. [39] shows a far-field spatiospectral plot, which is described as being separated into three regions: the first upstream region as being dominated by BBSAN, the second region that is the region of maximum radiation, and a third, further aft region that is dominated by a lower frequency component. These three regions appear similar to those seen in Fig. 2.3 of this paper at afterburning engine powers, where the $z < 7$ m region is dominated by BBSAN, 7 m $< z <$ 15 m is dominated by lobes 2-5, and $z >$ 15 m downstream is dominated by the low-frequency lobe 1. Leete *et al*. [92] investigated the coherence of the LES-generated field of Ref. [39] and found that the BBSAN component originated from the potential core region where shock cells are present, the region of maximum radiation originated from the supersonic portion of the jet, and the far aft radiation originated from an extended region around the end of the supersonic core. The source localizations of the BBSAN in Fig. 2.11 and the lobes in the afterburner cases in Fig. 2.13 agree qualitatively

with the pattern found in the LES dataset, with BBSAN originating in feasible locations for shock cells and lobe 1 appearing farther downstream than lobes 2-3.

An important distinction between the LES of the highly-heated laboratory-scale jet [39] and F-35 data seen in the present work is that the LES does not contain multiple spectral peaks, simply a smooth transition from spectra with a high-frequency peak towards the sideline to a low-frequency peak in the far aft. The only time any discrete spatiospectral content is seen in the LES is when the coherence with the field is calculated to a reference point along the nozzle lipline where shock cells are present (see Fig. 7 of Ref. [92]). The coherence of the field appears to split into spatiospectral lobe-type patterns, suggesting that shock cells contribute to the presence of distinct lobes. However, without more knowledge of the plume characteristics of the F-35, more specific comparisons cannot be made.

2.6 Conclusions

The sound field in the vicinity of a tied-down F-35B aircraft is examined for engine powers ranging from 25% to 150% ETR. The OASPL across a linear ground array approximately parallel to the shear layer show that as engine power increases, the directivity of the field in the main radiation direction shifts towards the sideline. Spatiospectral maps along the array show that trends in the jet noise field can be described as a superposition of multiple spatiospectral lobes, and the trends in overall level with engine power are explained by the number of lobes present and their distribution of amplitudes.

M-SONAH reconstructions of the field in the vicinity of the aircraft allow for a detailed look at the evolution of each spatiospectral lobe across frequency and engine power. At a single engine condition with increasing frequency, the lobes swing farther aft until they pass beyond the downstream extent of the array. While that happens, new lobe(s) appear upstream and then swing

aft as well. As engine power increases for a fixed frequency, all lobes increase in level and their directivity shifts slightly toward the sideline. Additionally, whichever lobe is the farthest upstream increases in level more than the other lobes present at that frequency, which seems to be the largest contributor to the overall directivity shifting forward.

The extra detail provided by this measurement of the F-35B along with the M-SONAH reconstructions of the field sheds light on previous measurements of similar high-performance military aircraft. These and prior data show that looking at the main radiation region from high-performance military jet aircraft as a single phenomenon is insufficient. The paradigm needs to shift to thinking of the main radiation lobe as a superposition of multiple, overlapping lobes, the trends of which across frequency and engine power dictate the trends of the overall field. The source mechanisms involved in producing the multiple radiation lobes are still unknown, though their presence at low engine powers suggests they are not combustion-related. Also unknown is why these phenomena appear to be more prominent in the current measurement of the F-35B than measurements of other aircraft, laboratory-scale jets, and numerical simulations. Answering these questions is necessary to have a complete understanding of aeroacoustic noise from full-scale high-performance jet aircraft.

2.7 Acknowledgments

The authors gratefully acknowledge funding for the measurements provided through the F-35 Joint Program Office and Air Force Research Laboratory. K. M. Leete was funded by an appointment to the Student Research Participation Program at the U.S. Air Force Research Laboratory, 711th Human Performance Wing, Human Effectiveness Directorate, Warfighter Interface Division, Battlespace Acoustics Branch administered by the Oak Ridge Institute for Science and Education through an interagency agreement between the U.S. Department of Energy and USAFRL. Distribution A: Approved for public release, distribution unlimited. F-35 PAO Cleared 07/21/2020, JSF20-612.

Chapter 3

Numerical Validation of M-SONAH Applied to the F-35 Field

This work has been published as "Numerical validation of using multisource statistically-optimized near-field acoustical holography in the vicinity of a high-performance military aircraft", Kevin M. Leete, Alan T. Wall, Kent L. Gee, Tracianne B. Neilsen, J. Micah Downing, and Michael M. James. Proceedings of Meetings on Acoustics 31:1. I hereby confirm that the use of this article is compliant with all publishing agreements.

3.1 Abstract

Multisource statistically optimized near-field acoustical holography (M-SONAH) is an advanced holography technique [Wall et al., J. Acoust. Soc. Am. 137, 963–975 (2015)] that has been used to reconstruct the acoustic field from measurements taken in the vicinity of a high-performance military aircraft [Wall et al. 139, 1938 (2016)]. The implementation of M-SONAH for tactical jet noise relies on creating an equivalent wave model using two cylindrical sources, one along the jet centerline and one below the ground as an image source, to represent the field surrounding an

aircraft tethered to a reflecting ground run-up pad. In this study, the spatial and frequency limitations of using the M-SONAH method to describe the field of a tethered F-35 is explored by using the same measurement geometry as at a recent test, but substituting the sound field obtained from a numerical source for the measurement data. The M-SONAH reconstructions are then compared to numerical benchmarks. A spatial region and frequency bandwidth where bias errors are low are identified and provide validation for the use of this method in tactical jet noise source and field reconstructions. [Work supported by USAFRL through ORISE and the F-35 JPO. Distribution A - Approved for Public Release; Distribution is Unlimited. Cleared 06/28/2018; JSF18-643.]

3.2 Introduction

Near-field acoustical holography (NAH) was developed for three-dimensional imaging of noise fields. The technique has been used for laboratory jet noise measurements [78, 79], and was recently adapted to measurements of full-scale military aircraft [82, 83, 104]. Statistically-optimized NAH (SONAH) [77, 93] fits an equivalent wave model (EWM) to the sampled field, which then can be evaluated at any arbitrary point of interest. Multisource statistically-optimized near-field acoustical holography (M-SONAH) is a version of SONAH adapted to image a three-dimensional sound field in the presence of a ground reflection [82]. It was originally developed to image the noise field in the vicinity of a military aircraft tied down to a concrete run-up pad, where the field was sampled approximately parallel to the jet shear layer with a two-dimensional measurement [54, 104]. In the process of analyzing the reconstructed field, it was found that the inclusion of only the zeroth-order Hankel functions in the EWM was sufficient to obtain accurate sound field reconstructions, and because of the lack of azimuthal coverage by the array, including higher-order terms did not substantially increase reconstruction accuracy. This leads to a question: if only axisymmetric terms in the EWM sufficiently describe the sound field, is a two-dimensional measurement necessary?

This question can be investigated by applying the M-SONAH technique with the axisymmetric EWM to one-dimensional measurements of the acoustic emissions of the F-35 Lightning II [55].

In that 2013 measurement, a linear ground array was placed approximately parallel to the shear layer, which spanned the axial extent of the jet plume. The resulting data are currently being used to characterize the sound field this aircraft produces across engine condition and frequency using M-SONAH [85, 105]. The purpose of this paper is to investigate the capabilities and limitations of the linear ground array as the input to the M-SONAH algorithm to reconstruct a three-dimensional field of the noise produced by this aircraft.

In the current study, M-SONAH reconstructions of the noise field near the aircraft running at 100% Engine Thrust Request (ETR) are obtained for two frequencies and compared against the measurement. Due to limitations in the measurement, the M-SONAH reconstructions cannot be validated at all locations of interest. To help validate the areas where no measurement was taken, a numerical experiment is created to simulate a sound field at the locations of the input array as well as the surrounding area. Then, the M-SONAH algorithm is run on this simulated data to reconstruct the simulated field and check for errors. The error in the field reconstructions of this numerical case are used to identify a spatial region where the reconstruction of the F-35 is expected to fit well and are compared to the error of the M-SONAH reconstruction of the F-35 noise field. Finally, measured spectra at locations in the geometric near field of the jet are compared against reconstructed spectra to check how well M-SONAH predicts ground interference effects.

3.3 Experiment and Analysis

3.3.1 Military aircraft data

An extensive measurement of the sound field in the vicinity of the F-35B was performed at Edwards's Air Force Base in 2013 [55]. The aircraft was tied down to a concrete run-up pad

while the engine was cycled through various engine conditions, from 13% ETR (idle) up through 150% ETR (maximum afterburner). The aircraft has a Pratt & Whitney F135 afterburning turbofan engine, which can achieve up to 43,000 pounds of thrust. The nozzle of the engine was 2.0 m from the ground and had a nominal 1 m diameter, though the exact nozzle diameter changed with engine condition. Over 350 microphones were deployed at locations near the shear layer out to 1.2 km from the aircraft. The data used as input to the holography process were gathered from a linear, 71-element ground array with 0.45 m (1.5 ft) inter-element spacing, which was placed approximately parallel to the shear layer of the jet with a standoff distance of about 8 m. This study uses the measurement of the F-35B operating at 100% ETR.

The Cartesian coordinate system used in this study is such that the origin is a point on the ground directly below the nozzle exit plane with the z-axis pointed downstream, the x-axis towards the sideline, and the y-axis pointed upward. The jet centerline is the line $x = 0$ and $y = 2.0$ m and the nozzle lipline is approximated by the line $x = 0.5$ m, $y = 2.0$ m. The array was laid out on the left side of the aircraft in the test, though for convenience all figures here are mirrored to show it on the right. Figure 3.1a) shows a schematic of the measurement arrays out to 76 m from the aircraft, where Figure 3.1b) is a zoomed-in portion near the aircraft. The far-field arcs were centered on the Microphone Array Reference Point (MARP), which was 7.5 m downstream of the nozzle. Whereas positions are referenced to the origin located on the ground below the nozzle exit plane, the jet inlet angle, θ, is defined relative to the MARP, where$\theta = 0^\circ$ points in the direction of the aircraft nose.

3.3.2 Numerical Test case

To test the effectiveness of the M-SONAH algorithm in the context of the measurement geometry, a numerical source was created along the jet centerline. The source, as pictured in Fig. 3.2, is similar to equivalent source models that have been created for jet noise [35, 106–108]. It is a superposition of two linear distributions of monopoles along the jet centerline. One is a line of

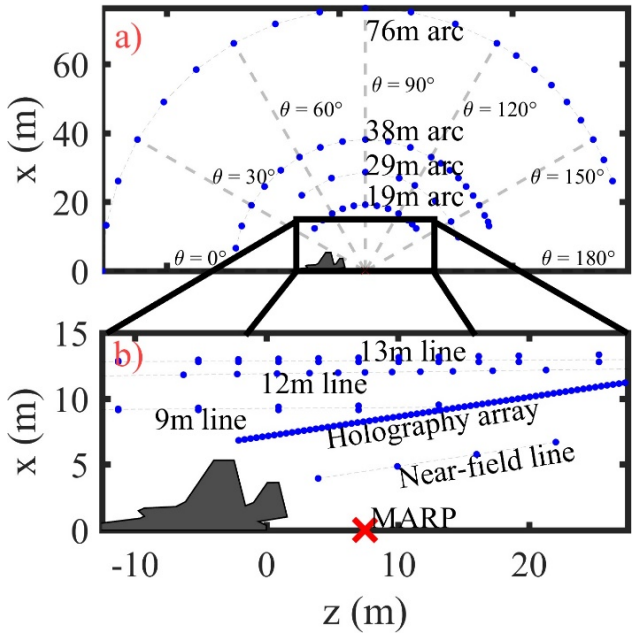

Figure 3.1 Schematic of the measurement. The outline of the aircraft is marked with gray, the red x is the microphone array reference point (MARP), and the blue dots are measurement locations. The far-field arcs are measured with the MARP as their center point. Part b) is a zoomed in portion of part a) near the aircraft

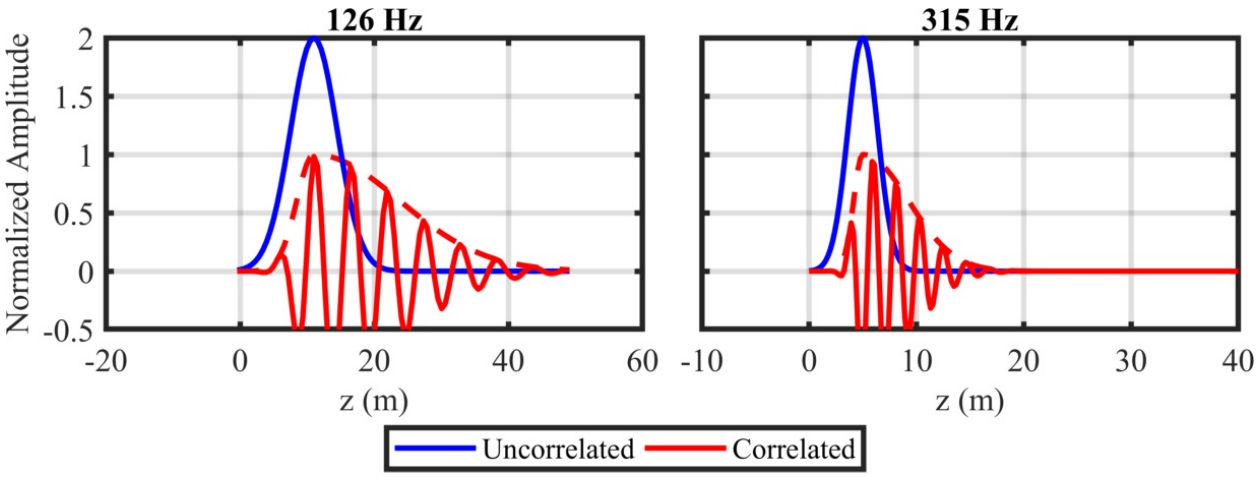

Figure 3.2 The source at 126 Hz (left) and 315 Hz (right). Each source is a superposition of two distributions of monopoles along the jet centerline one Gaussian distribution of uncorrelated monopoles (blue) and one asymmetric Gaussian of correlated monopoles (red) that has a phase relationship to produce directional radiation at $\theta = 120^\circ$

correlated monopoles whose amplitudes are weighted with an asymmetric Gaussian distribution and have a fixed phase relationship to produce a directional radiation pattern at $\theta = 120^\circ$. The other is an uncorrelated distribution of monopoles, with a Gaussian envelope of amplitude twice that of the correlated distribution. The frequency-dependent widths of the Gaussian distributions along with their peak locations on the z - axis were loosely based on Figure 13 of Ref. [103]. To account for the ground reflection, an identical image source was centered at $y = -2.0$ m. Rayleigh integration was performed to calculate the radiated sound at all measurement locations in the field as well as to a fine, two-dimensional grid at $y = 2.0$ m. At each frequency of interest, this was realized 500 separate times with added random phases to simulate measurement blocks. Afterward, simulated uncorrelated measurement noise was added to each block of each field location to yield a signal-to-noise ratio of 80 dB. The simulated blocks were then averaged over to give a single complex pressure value. The radiated fields from these distributions are visualized in the top row of Figure 3.3.

3.3.3 M-SONAH method

The M-SONAH method involves the following steps, which are more extensively discussed in Refs. [82, 83]:

1. Extract frequency dependent complex pressures from recorded pressure waveforms
2. Perform a partial field decomposition to generate mutually incoherent partial fields
3. Numerically extrapolate each partial field beyond the measurement aperture
4. Formulate the EWM of the jet in the run-up pad environment and solve for pressure at desired reconstruction locations

First, the frequency-dependent complex pressures were obtained. For the F-35 measurement, the recorded 30-second time waveforms were split into multiple blocks with a 50% overlap, windowed with a Hann function, then the Fourier transform was applied to each block. The block sizes were adjusted to give a frequency resolution of 3 Hz. Steps 2-4 were applied for each frequency independently.

Second, because the complex pressures for a given frequency along the input array were partially correlated, it was necessary to perform a singular value decomposition of the cross-spectral matrix of the measurement array to generate mutually incoherent and self-coherent partial fields. Each partial field is the singular vector given by the decomposition scaled by its corresponding singular value. Steps 3 and 4 were then applied for each partial field individually and the results summed energetically to reconstruct the entire field at that frequency.

Third, to reduce leakage to high wavenumbers and wraparound error due to the finite nature of the input array, each partial field was numerically extrapolated beyond the measurement aperture using a linear prediction method [95]. Because the aperture extension technique was only accurate within a short distance of the edge of the array, a Tukey window was used to reduce the field to zero outside of one acoustic wavelength of the edge of the array.

Fourth, the EWM uses one set of cylindrical wave functions centered on the jet centerline and a second set centered on the image source below the ground to model the reflection. The EWM methodology used in the M-SONAH algorithm is described in detail in Ref. [82], which uses cylindrical Hankel functions as the basis. The solution for the vector of pressures at the desired reconstruction locations ($p(r_q)$) is given in terms of the vector of pressures along the input hologram ($p(r_h)$) by Equation 3.1,

$$p^T(r_q) = p^T(r_h) R_{A^H A} A^H \alpha, \tag{3.1}$$

where A and α are matrices comprised of each of the wavefunctions in the EWM (each column) evaluated at the hologram and reconstruction locations (each row), respectively. $R_{A^H A}$ is the regularized inverse of the matrix $A^H A$. This entire process can be described as finding the minimum norm EWM that fits the hologram data, then reevaluating the EWM at the location where the reconstructed field is desired or alternately, thinking of the matrix $R_{A^H A} A^H \alpha$ as a transfer matrix between the measured pressures at the hologram and the reconstruction locations of interest.

3.3.4 Reconstruction of the Numerical Case

The utility of the M-SONAH technique is exemplified via field reconstructions of the numerical case. The simulated field, M-SONAH reconstructions, and their error are displayed in Figure 3.3 for two frequencies: 126 Hz (left) and 315 Hz (right). The colored contour plots show the sound pressure level (SPL) at each point in a two-dimensional plane at y=2.0 normalized to the maximum level along the nozzle lipline. The black line represents the position of the hologram. The upper plots are the simulated data from the numerical source, the middle plots are the M-SONAH reconstruction from the numerical data, and the lower plots are the error in the reconstruction. With the input of only the measured hologram, reconstructions of the field over a large area are obtained. Low errors are seen in the triangular aperture covered by the array with high errors outside. The largest

difference between the left and right plots are the ground interference patterns. By design, the source at 315 Hz was more compact than the source at 126 Hz, which caused the ground interference nulls to have a more circular pattern. Since the EWM being used is a cylindrical wave model, it seems the algorithm has a tendency to align ground interference nulls parallel to the jet centerline instead of circularly as it should. The largest sources of error inside the aperture covered by the array seem to be due to the inability of the algorithm to reconstruct the correct ground interference patterns. The 126 Hz case matches better as the nulls in the field are parallel to the jet centerline.

The region spanned by the array that is not in a ground interference null has errors consistently less than 1 dB. This region of good fit appears to cover an area where the levels are within ± 20 dB of the input holography array, which is quite a large span and is heartening for its potential usefulness to characterize the F-35 field.

One purpose of performing M-SONAH has been to obtain equivalent acoustic source characteristics by reconstructing the field along the nozzle lipline of the jet [83]. The reconstruction amplitudes give information about the spatial distribution of noise sources, or the complex pressures can give an equivalent pressure-source model that can be reradiated to reproduce the field. Figure 3.4 shows the sound pressure levels of the numerical dataset (blue) along with the reconstructions (red) at the nozzle lipline ($x = 0.5$ m and $y = 2.0$ m). The acoustic source region where the error in the reconstruction is less than 1 dB is marked by the magenta dashed lines, which includes levels about 5 dB down from the maximum.

3.3.5 Reconstructions of the F-35 field

There is a clear boundary between high and low accuracy in the M-SONAH reconstructions. For the numerical case, it is seen in the lower row of plots in Figure 3.3, where the area within the aperture of the input array show errors consistently below 2 dB. This gives a potential region of confidence in the accuracy of the reconstructions of the F-35. To compare the F-35 reconstructions against the

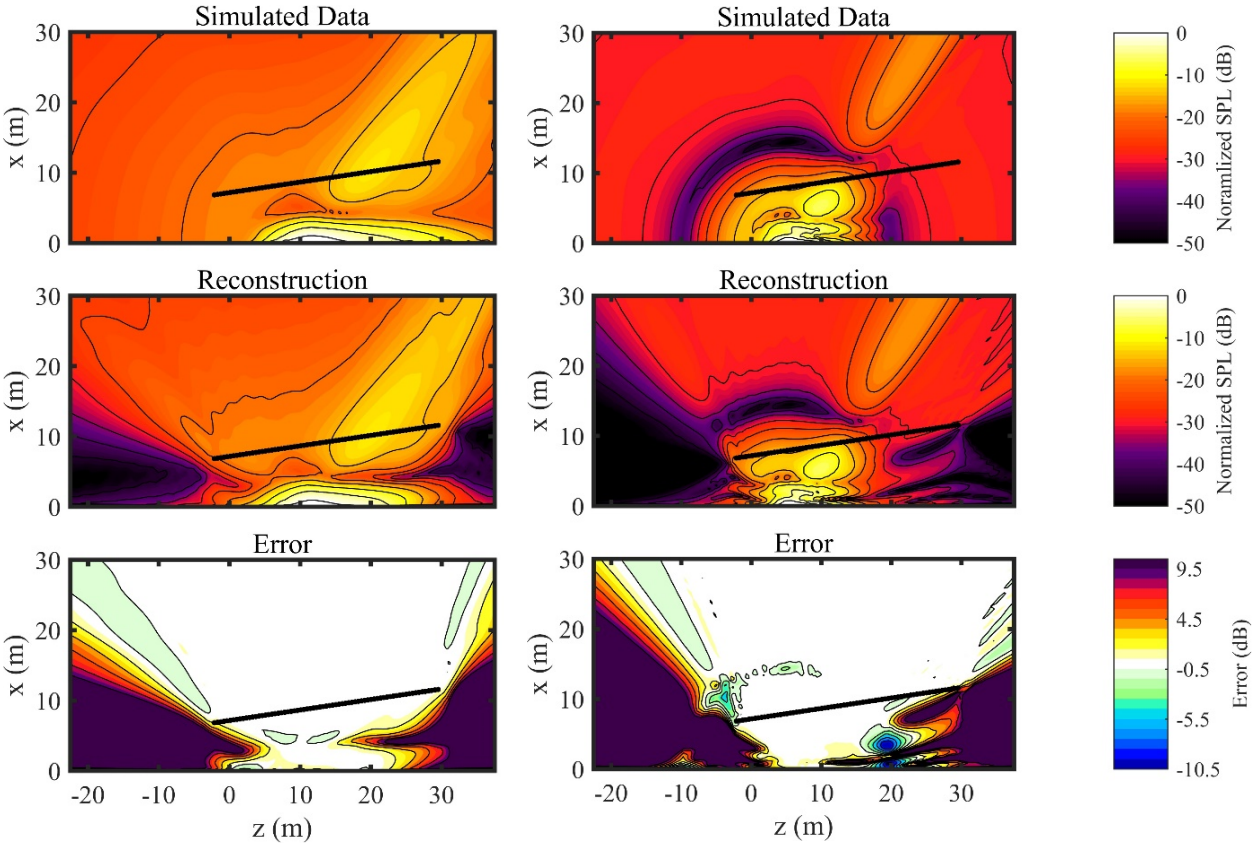

Figure 3.3 SPL (normalized to the maximum level along the nozzle lipline) for each point in a 2-D plane parallel to the ground at the jet centerline height. The black line marks the location of the input array for the holography process. The left column of plots is at 126 Hz, and the right column of plots is at 315 Hz. The upper row of plots are the simulated data at each location, the center plots display the M-SONAH reconstructions, and the lower plots show the differences between the two.

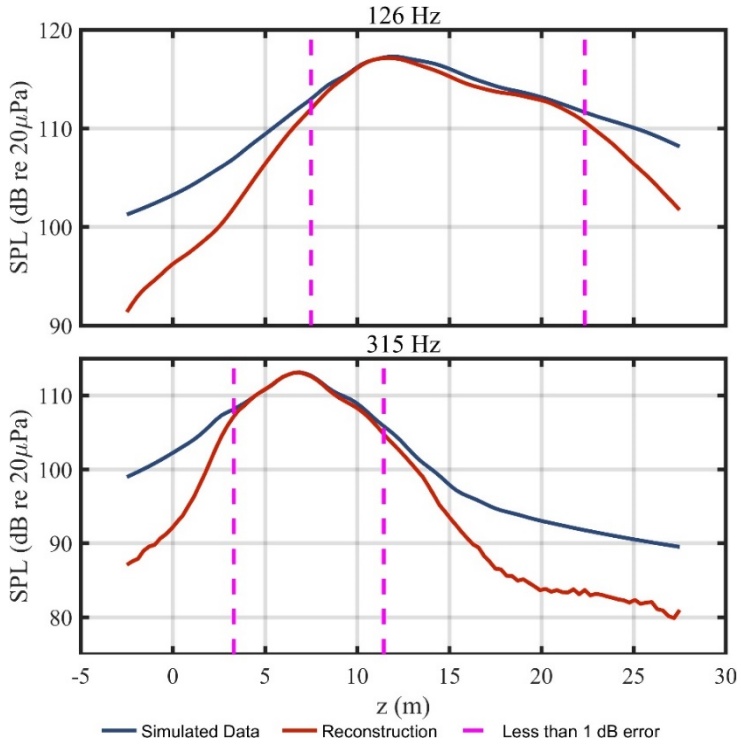

Figure 3.4 Reconstructions of the field (red) along the nozzle lipline ($x = 0.5$ m at the jet centerline height) compared to the simulated data (blue) at the same locations. Magenta dashed lines represent where the error in the reconstruction exceeds 1 dB.

measured sound field, the reconstructed and measured SPL along the input hologram as well as several arrays pictured in Figure 3.1 are plotted in Figure 3.5. The top and bottom plots show 126 and 315 Hz, respectively. The diamonds represent the measured levels at the various subarrays, and the dashed colored lines represent the M-SONAH reconstructions at those locations. Exceptional agreement for both inward and outward propagation from the hologram is found for θ between 50° and 150°, where all errors are less than 2 dB and often less than 1 dB. This angular span coincides with maximum coverage by the input hologram.

The reconstructions of the jet noise field of the tethered F-35 are displayed in Figure 3.6 for two frequencies. The colored contour maps represent the single-frequency SPL at each point in the two-dimensional plane parallel to the ground at $y = 2.0$ m. To identify a region of potential accuracy of reconstruction, a thick white contour is drawn on Figure 3.6 where the reconstruction error of the numerical case was less than 2 dB. The field inside the white contour appears as expected for military jet noise—a large radiation lobe which beams at a large aft angle with lower levels radiating towards the sideline. The acoustic source region extends tens of meters down the $z-$axis, with the 126 Hz case having about twice the extent as the 315 Hz case. The 315 Hz case also shows the maximum radiation lobe at a slightly forward position. Ground reflections are similar in shape and location to those seen in Figure 3.3 for the numerical case. Additionally, when the green dashed lines from Figure 3.5 are superimposed on Figure 3.6. It can be seen that for the most part, the 2 dB error contour from the numerical case covers approximately the same region as the 2 dB error region from the actual measurement (over the aperture pictured here). This provides confidence that the reconstructed field is representative of the physical field in the angular region covered by the array propagated outward toward the arc arrays.

For inward propagation from the hologram towards the jet centerline, Figure 3.6 shows that the 2 dB error contour from the numerical case coincides with predicted locations of ground interference nulls, implying that the model does not accurately capture the ground reflection pattern. In the

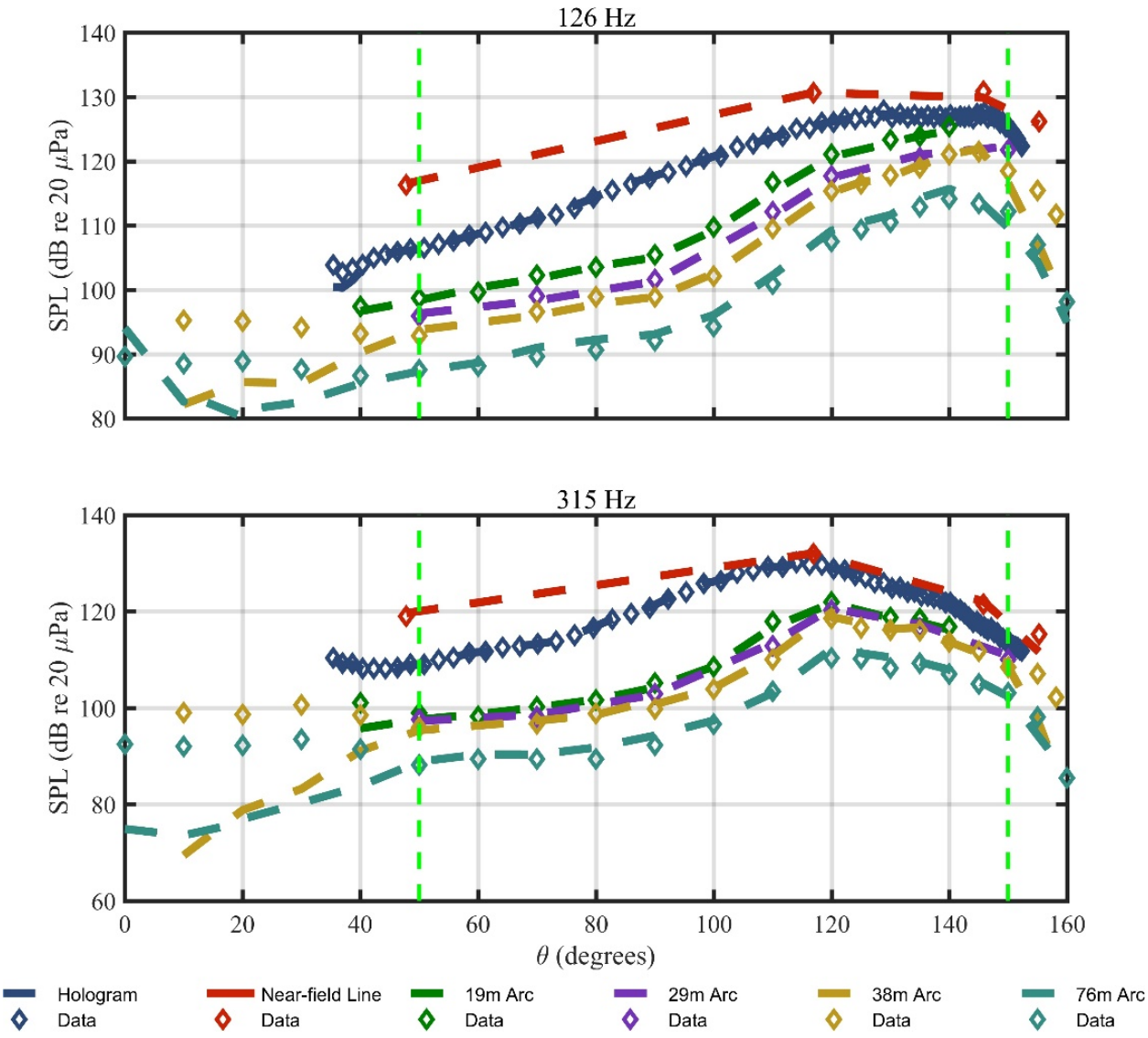

Figure 3.5 Comparison of measured data of the F-35 to the M-SONAH reconstructions at several arrays at 126 and 315 Hz. The horizontal axis is the jet inlet angle (θ), the vertical axis the sound pressure level, the dashed colored lines represent the M-SONAH reconstruction at the specified array locations, and the diamonds are the measured data. The vertical green dashed lines represent the angular aperture where all measured errors are less than 2 dB.

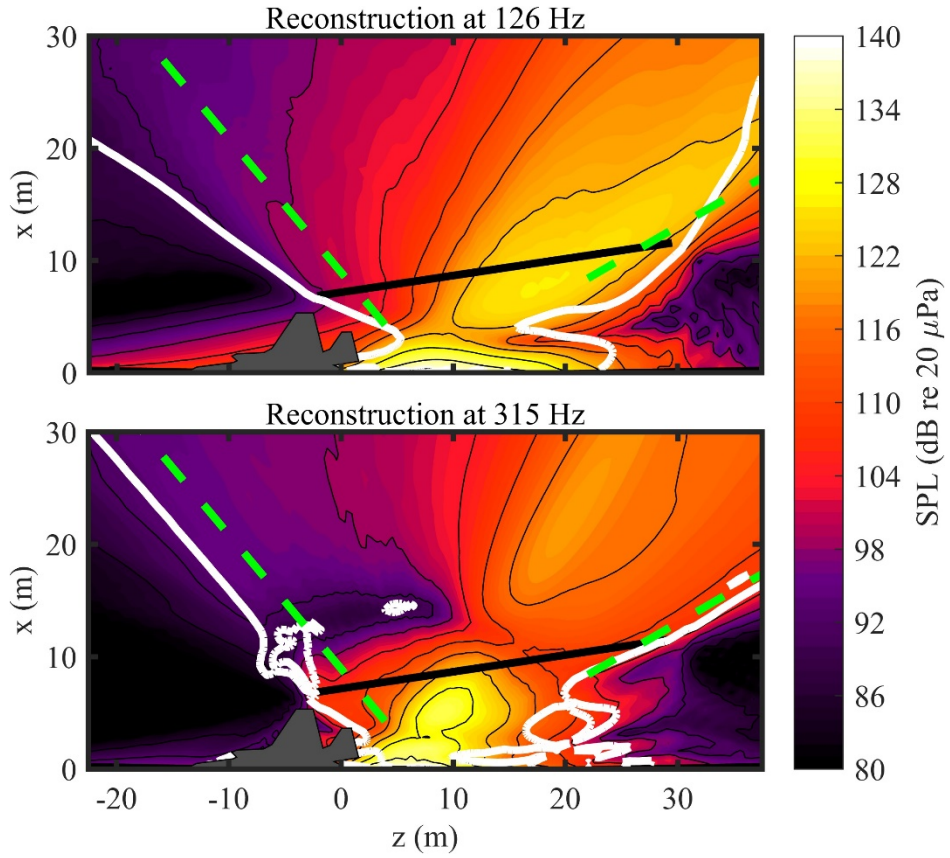

Figure 3.6 M-SONAH Reconstruction of the field of the F-35B at 126 and 315 Hz. The colored contour plot shows the SPL of the reconstructed field at each point in the 2-D plane at the height of the jet centerline. The grey outline shows the position of the aircraft. The thick white line is the 2 dB contour line taken from the error of the numerical case (Figure 3.3). The green dashed line is taken from Figure 3.5 to signify the angular aperture where errors are estimated to be less than about 2 dB.

numerical case, errors in predicting the ground interference pattern seem to be caused by the reconstructions having interference nulls characteristic of a cylindrically-radiating source, when the input data would suggest a more spherically radiating one. For example, at 315 Hz, the numerical field has a strong interference null in an arc, which suggests that the source is compact enough to radiate in a spherical fashion, where the reconstructions reallocate the interference nulls into nulls parallel to the z axis. There are a few aspects of the M-SONAH process which are hypothesized to cause this reallocation. First, the EWM as formulated in the matrices A and α inherently only include a finite number of cylindrical basis functions. Also, the regularization step in the inversion of $A^H A$ acts to decrease the influence of the higher order wavefunctions, so as to not become numerically unstable. The net effects of these is to act as a low-pass spatial filter of sorts, causing difficulty in reconstructing a spherical shape from a cylindrical model.

For the F-35, the M-SONAH reconstructions in Figure 3.6 show a more cylindrical-like ground interference pattern between the jet centerline and the hologram, but as seen in Figure 3.1b), the only measurements in that region were the holography array and the near-field line. These arrays were both ground-based, so no interference pattern is observed. There is no way to conclusively verify if the reconstructions of the F-35 field are physically representative of the actual field in that area, though an investigation of ground interference effects where there were measurements can give clues as to whether the field is behaving cylindrically or spherically.

To investigate the ground interference pattern of the F-35 field, Figure 3.7 plots the spectra measured at $\theta = 70^\circ$ and $\theta = 140^\circ$ from the 19-m arc. For comparison, the M-SONAH reconstructions as well as theoretical ground interference patterns calculated at those points are superposed. In the $\theta = 70^\circ$ case, the M-SONAH reconstruction (blue dashed lines) match the measured spectra (solid blue lines) well until it enters a region of a ground reflection interference null, where the reconstruction severely underestimates the field. The M-SONAH algorithm is expected to overestimate the depths of ground interference nulls because of its ideally compact nature. In reality,

the jet plume is a turbulent, volumetric source that would cause the ground reflection to not have such a sharp null. To evaluate the proper placement of ground reflection nulls in the frequency domain, Figure 3.7 includes an ideal ground reflection pattern from a source located at the MARP (dashed red line), and an infinite cylindrical source along the jet centerline (solid red line) overlaid on the measured spectra. The $\theta = 70^\circ$ case shows the measured data, the M-SONAH reconstruction, and both theoretical ground interference patterns having a null in the same frequency region. This suggests that the sources contributing to the field at this location can be accurately modeled as either a monopole-like source close to the MARP or as a line source along the jet centerline.

An interesting feature is seen in the $\theta = 140^\circ$ plot of Figure 3.7, where M-SONAH predicts there should be a ground interference null around 480 Hz, the cylindrical and spherical ground interference patterns predict nulls at 350 and 550 Hz, respectively, and there is no apparent measured null in the spectrum. This could mean that in actuality, the jet noise field is the superposition of multiple different interference patterns from multiple sources with different locations and extents, where their interference patterns combine to yield a flat response. In a previous study of a high-performance military aircraft engine [16], it was found that microphones that were in different (spatially separated) ground interference nulls had partial mutual coherence. One possible explanation for this is if the plume had multiple sources: one which was experiencing a ground interference null at those locations and another that was not [16]. The M-SONAH algorithm does not appear to replicate this nuance, and lumps any potential individual source mechanisms into a single source, which has a ground interference pattern somewhere in between cylindrical and spherical, which is expected for a cylindrical source of finite length. It is important to note that because of aliasing limitations due to the inter-element spacing of the input holography array, M-SONAH reconstructions above 600 Hz were not completed. Ground reflection interference patterns therefore cannot be fully explored in all locations, particularly in the mid-to-far-fields where the interference nulls are pushed into higher frequencies.

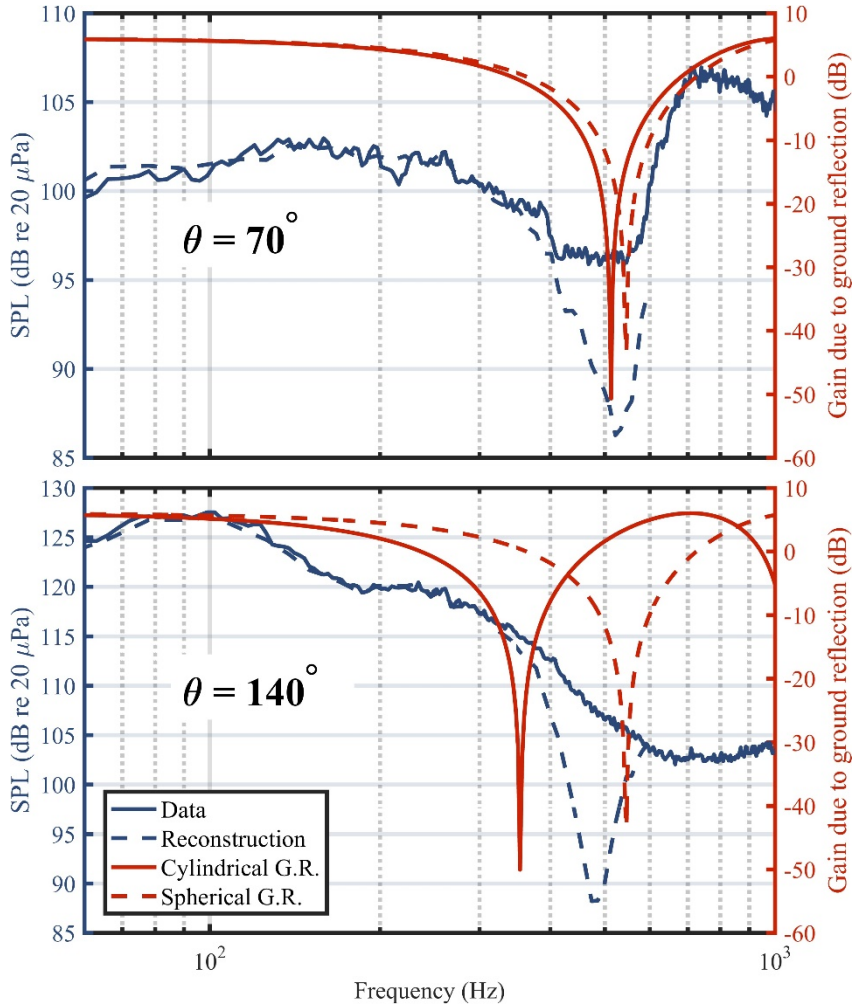

Figure 3.7 Measured spectra at $\theta = 70^\circ$ and $\theta = 140^\circ$ from the 19-m arc array (solid blue) compared with reconstructions (dashed blue) as well as theoretical gains due to a ground reflection by a cylindrical source (solid red) and from a monopole source placed at the MARP (dashed red)

In summary, towards the sideline of the jet the interference pattern appears either cylindrical-like (which matches well with the EWM used in M-SONAH and allows for correct placement of the ground interference nulls in the reconstructions of the field) or monopole-like from a source location that by happenstance allows the cylindrical EWM to place the interference nulls in the correct location. However, in the aft region, the region of maximum radiation, the EWM as presently constituted is insufficient to accurately model the ground reflection from the complicated aeroacoustic source of the F-35. Even with this limitation, the reconstructed levels match the measured levels exceptionally well where there are no ground interference effects, as shown by the dashed green lines in Figures 3.5 and 3.6 which denote a region where all measured errors were less than 2 dB from the input hologram out to an arc with a radius of 76 meters. The SONAH algorithm, and its current implementation in M-SONAH, has sufficient flexibility to allow the user to modify the EWM to account for additional source locations and distributions without requiring a priori assumptions about source coherence or source strengths. Future modeling efforts could use more tailored EWMs to better fit spatial/spectral interference patterns.

3.4 Conclusions

Initial investigations of M-SONAH field reconstructions in the vicinity of an F-35 have been discussed. Inside the spatial aperture of the measurement array, the reconstruction of a numerical source has excellent agreement to the field, generally within 2 dB error. The reconstructions of the F-35 field match measurements to within 2 dB error over that aperture in most cases. Errors only become substantial in spatial and frequency regions where ground interference nulls dominate the field. Outside the angular coverage of the hologram, the M-SONAH process substantially underestimates the field in both the numerical and measured cases due to a lack of an effective

aperture extension protocol. The use of a few sparse datapoints collected beyond the measurement aperture to inform improved aperture extension processes is being explored.

Investigation of the ground interference nulls predicted by the M-SONAH algorithm show that the field towards the sideline of the jet, outside of the region of maximum radiation, can be accurately represented by the cylindrical EWM. In the region of maximum radiation, the ground interference nulls predicted by the M-SONAH process are not apparent in the data. It is likely that multiple, distinct sources in the jet plume are spatially separated (or distributed) enough to cause changes to the measured ground interference pattern that is not captured by the EWM. In theory, this should be correctable by the inclusion of additional source terms, which will be explored as a possible model refinement.

Acknowledgements

The authors gratefully acknowledge funding for the measurements, provided through the F-35 Program Office and Air Force Research Laboratory. K. M. Leete was funded through by an appointment to the Student Research Participation Program at the U.S. Air Force Research Laboratory, 711th Human Performance Wing, Airman Systems Directorate, Warfighter Interface Division, Battlespace Acoustics Branch administered by the Oak Ridge Institute for Science and Education through an interagency agreement between the U.S. Department of Energy and USAFRL. (Distribution A – Approved for Public Release; Distribution is Unlimited. Cleared 06/28/2018; JSF18-643.)

Chapter 4

Measurement of the Boeing T-7A Aircraft's Noise Emissions

This chapter is an abridged version of the publication entitled "Jet Noise Measurements of an Installed GE F404 Engine", Kevin M. Leete, Aaron B. Vaughn, Michael S. Bassett, Reese D. Rasband, Daniel J. Novakovich, Kent L. Gee, Steven C. Campbell, Frank S. Mobley and Alan T. Wall. AIAA 2021-1638. AIAA Scitech 2021 Forum. January 2021. I hereby confirm that the use of this article is compliant with all publishing agreements.

A large, multi-organizational effort to measure the sound field generated by the T-7A trainer aircraft is documented. My role was to aid in the planning of the near-field array (which will be used for future acoustical holography purposes, in the same vein as Chapter 2) and oversee the data validation and compilation into a single, usable framework (including the publication of the document).

4.1 Abstract

This paper describes noise measurements taken of the new Boeing T-7A Red Hawk trainer aircraft, which uses a single F404 afterburning turbofan engine. The extensive measurement satisfies the American National Standards Institute/Acoustical Society of America standard S12.75-2012 for ground run-up for future environmental impact assessment and includes additional locations around the aircraft to understand exposure by maintenance personnel. A large near-field array was also deployed to shed light on phenomena that are not generally seen in the measurement of laboratory-scale jets, such as the presence of spatiospectral lobes. Initial data analysis shows they are of high fidelity and contain similar phenomena as other recent high-performance jet aircraft noise measurements, including evidence of large and fine-scale noise radiation, broadband shock-associated noise, spatiospectral lobing at multiple engine powers, an upstream shifting of overall level directivity with engine power, and appreciable shock content in the measured waveforms. Further analysis of this dataset will add to the understanding of full-scale, high-speed jet noise and allow comparisons to similar numerical simulations and laboratory-scale measurements.

4.2 Introduction

The Air Force Research Laboratory (AFRL) led a multi-organizational effort to measure the noise generated by the new Boeing/Saab T-7A "Red Hawk" aircraft at Holloman Air Force Base in August 2019. The three purposes of the measurement were to a) characterize the noise for environmental and community impact assessment following the ANSI/ASA standard S12.75 for ground run-up, b) understand levels experienced by maintainers working around the aircraft during various operations, and c) increase understanding of the aeroacoustic noise sources generated by military aircraft, including phenomena not generally seen in laboratory-scale jet noise measurements.

Numerous methods have been used to alter the jet flow produced by aircraft in an attempt to reduce the radiated noise [1]. Specifically for the F404 engine, the use of microjet injectors, [109], chevrons [110], contoured inserts [111] and twin jet nacelles [112] have been investigated for noise reduction. Of critical importance in developing these and future technologies is the understanding of how jet noise differs between full-scale installed engines, laboratory-scale models, and numerical simulations [113]. The addition of this dataset to growing repositories of measurements of high-performance aircraft will allow for further understanding of these complex noise mechanisms, which can inform future jet noise reduction studies.

In recent years, several measurements have been taken of full-scale military aircraft operating at various engine powers. [54, 55, 114] Subsequent analyses of these datasets show phenomena that are not often reproduced at laboratory scales, such as the presence of spatiospectral lobes [105]. Spatiospectral lobes are local maxima in the space-frequency domain, which manifests itself either as multiple peaks in a spectrum measured at a single location, or multiple maxima in the levels when plotting a single frequency across space. These spatiospectral lobes have been seen in measurements of aircraft with round [55, 114] and rectangular [60, 83] nozzles operating with and without the addition of afterburner.

The layout of the remainder of the paper is as follows. First, Section 4.3 discusses the measurement procedure, microphone arrangement, and data acquisition systems used. Sections 4.4, 4.5, and 4.6 discuss measurements of the near-field Imaging array, the influence of the ground reflection on off-ground measurements, and measurements by the far-field arrays. Overall sound pressure levels (OASPL) under and around the aircraft and spatial maps of select one third octave band levels are included in the Appendix.

4.3 Measurement Description

4.3.1 Measurement Procedure

The measurement was conducted early in the morning on August 18$^{\text{th}}$, 2019 at Holloman Air Force Base in New Mexico. The aircraft was tied-down to a concrete run-up pad which extended 12.2 m (40 ft) to either side of the aircraft and far downstream. The origin of the coordinate system used is directly under the nozzle exit on the ground, with the positive x-direction downstream of the nozzle, negative x-direction upstream towards the nose of the aircraft, positive y-direction on the array side (port side of the aircraft), and positive z-direction as the height above ground. The nozzle center was approximately 1.65 m ($65''$) above the ground, though this varied slightly ($\pm$5 cm) throughout the test as the pitch of the aircraft compensated for the changes in engine power. A microphone array reference point (MARP) located $13'$ downstream of the nozzle was established to determine angles, θ, relative to the jet inlet with 0° pointing upstream towards the nose of the aircraft and 180° pointing downstream along the jet centerline.

The aircraft was cycled through various engine conditions multiple times, pausing at each condition for at least enough time for each data acquisition system to record for 30 seconds. An ambient measurement was first taken before startup, then the auxiliary power unit startup sequence initiated and ran until fully prepped for engine startup. The engine was then started and ran at idle. Then, the engine was run at N2 values of 75%, 82%, 88%, at full military power, and then with afterburner. After 30 seconds at afterburner, it was brought down to idle for a few minutes, then the cycle from 72% N2 to afterburner was repeated and finally powered down. This complete sequence was repeated two additional times, giving at least six measurements of each test point. For the purposes of this paper, results from 82%, 88%, Military power, and Afterburner will be shown.

4.3.2 Microphone Arrangement

Over 200 microphones were organized into various arrays from the immediate vicinity of the aircraft out to 229 m (750′), as shown in Fig. 4.1. Eleven locations under and around the aircraft were measured using a set of four low-sensitivity GRAS 40BG $1/4''$ pressure microphones on tripods which were moved between measurements to cover all the locations (numbered orange circles). Four low-sensitivity GRAS 40BH $1/4''$ pressure microphones were placed approximately parallel to the shear layer of the jet and taped to the ground. Farther out, a 120-channel array (referred to as the "Imaging array") of GRAS 46BD and 46BG $1/4''$ pressure microphones were taped to the ground, ranging from $x = -15.2$ m (50′) to $x = 53.0$ m ($-174'$) (gray circles in Fig. 4.1b). Downstream of the nozzle, the array was linear, starting at $y = 17'$ and extending aft approximately parallel to the shear layer. Upstream, the array linearly increased in y for several feet then extended upstream parallel to the jet centerline. The inter-element spacing of the array varied based on predicted peak frequencies of the aeroacoustic noise, such that the spacing was smaller towards the sideline of the jet where higher frequency components were predicted to dominate and larger in the aft, where the louder, lower frequency components were predicted to dominate. On the concrete run-up pad was also a line array 7.62 m (25′) parallel to the jet centerline, which spanned from $x = -21.34$ m to $x = 18.29$ m (light green circles in Fig. 4.1b). Special low-sensitivity GRAS 40BE-S2 free-field microphones, which have been used on previous measurements of high-performance aircraft [54] were mounted on tripods 1.52 m (5′) off the ground.

Beyond the run-up pad, there were five microphone arc arrays centered around the MARP with radii of 19.1 m, 38.1 m, 76.2 m, 152 m, and 229 m (63′, 125′, 250′, 500′, and 750′), corresponding to dark blue, red, green, purple, and yellow circles in Fig. 4.1a. The 19.1 m and 38.1 m (63′ and 125′) arcs consisted of GRAS 40BE-S2 microphones, whereas the remaining arcs used $1/4''$ GRAS 40BE and 46BD microphones, all of which which were mounted 1.52 m (5′) off the ground. The 19.1 m, 38.1 m, and 76.2 m (63′, 125′, and 250′) arrays ranged from 30° to 160° in 10° intervals,

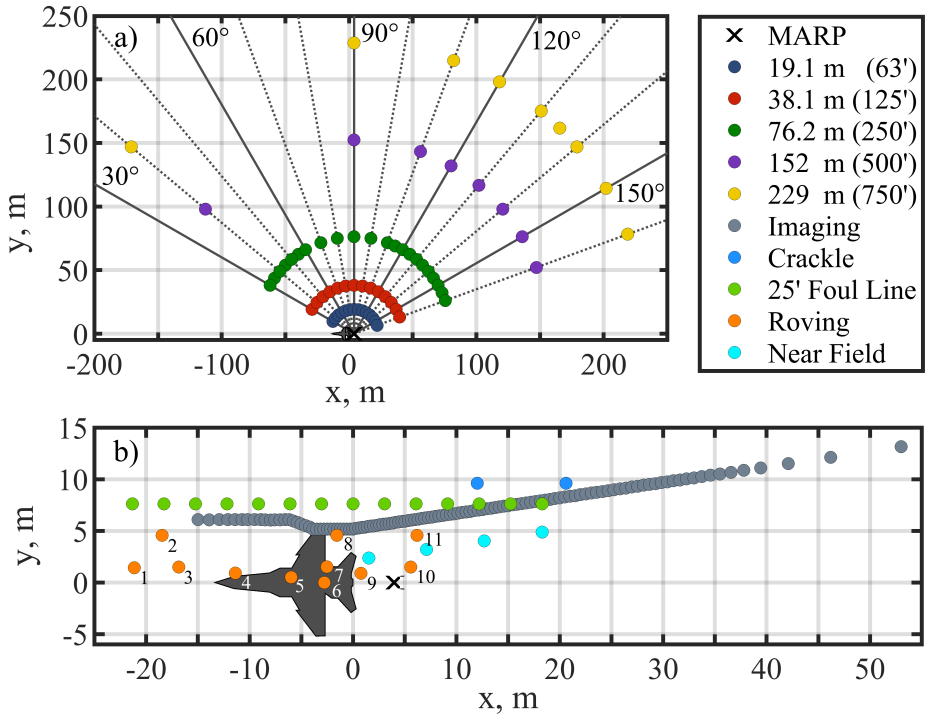

Figure 4.1 Measurement schematic of the T-X for the a) far-field microphone arcs and b) near-field microphone arrays. Angles are defined relative to the jet inlet and centered about the microphone array reference point (MARP) with solid and dashed lines every 30° and 10°, respectively. Though the array was physically placed on the port side of the aircraft, it is shown mirrored in this figure for plotting convenience.

with additional locations in 5° increments from 110° to 160° for the 76.2 m (250′) arc. Additional arc arrays at 152 m and 229 m (500′ and 750′) are more sparse with locations at 40°, 90°, 110°, 120°, 130°, 135°, 140°, 150°, and 160°. At these two outer arcs, the terrain became significantly more uneven and overgrown with brush, sometimes as tall as the mounted microphone height.

Other than the aforementioned arrays, additional measurements were taken to investigate the effect of microphone height on the measured sound field and the influence of the ground reflection on the perception of crackle. Two such setups on the concrete run-up pad were placed at 130° and 150° and included GRAS 1/8″ 40DD microphones mounted on the ground as well as at 2.54, 7.62,

Figure 4.2 Images of T-X measurement layout at Holloman Air Force Base, New Mexico: a) tied-down aircraft with 38.1 and 19.2 m (125′ and 63′) arcs and maintainer mics visible, b) imaging ground array and maintainer mics facing downstream, c) 130° crackle station facing a loudspeaker located at the MARP, d) Imaging array data acquisition unit, and e) Kestrel weather station located at 57.2 m (187.5′) along the 70° radial.

and 15.24 cm (1″, 3″, and 6″) heights, with GRAS 1/4″ 46BD microphones at 0.305 and 1.52 m (1′ and 5′) heights. These locations are shown as the light blue dots on Fig. 4.1b).

4.3.3 Data Acquisition

The microphones comprising the Imaging array and the near-field line connected to a large National Instruments PXIe 24-bit system populated with 449x series 16-ch cards and 4462 4-ch cards. To simplify cabling, 4X infiniband cables were used to run from the acquisition system to the arrays and custom infiniband to BNC breakout boxes attached to connect the individual channels to the infiniband cable. The system provided 4mA constant current power to the prepolarized microphones, and was able to sample all 120+ channels at a 204.8 kHz sample rate over a ±10V range. The PXIe

chasis was controlled by a NI-8354 server with two internal and one external solid state drives for data storage.

The 7.62 m (25′) line array as well as the 19.1 m, 38.1 m, and 76.2 m arc arrays and the roving maintainer microphones were run via BNC and Infiniband cable to a National Instruments PXIe-1062Q chasis with 4496 and 4497 cards, as well as an 8840 Quad Core Controller. The 100+ channels were intended to be sampled at 204.8 kHz as well, though limited hard-drive write speeds required that the sample rate be changed to 96 kHz partway through the test. A 4mA constant current power supply over ±10V input range was used for this acquisition system as well. The controller was operated via remote desktop connection from a laptop to manage the recording process.

The microphone height study on the run-up pad were connected via Infiniband cable to a third PXIe chasis loaded with two 6-ch 24-bit National Instruments PXIe-4480 cards. This was controlled by a laptop via expresscard that sampled the twelve channels at 1.024 MHz over a ±10V range with capacity for 10mA constant current power.

To avoid excessive cable runs to the 152 m and 229 m arc arrays, the 18 channels were collected using seven individual data acquisition systems placed in the field near their respective microphones. They were comprised of National Instruments 9250 2-channel cards mounted onto 9174 cDAQ 4-slot USB chassis, which were plugged into small tablet PCs. The fixed ±5 V, 2 mA data acquisition systems, computers, and IRIG-B timeclocks were all powered by MAXOAK lithium-ion batteries, creating a compact, portable data acquisition unit. Each tablet PC also connected via Bluetooth to Kestrel 4500 weather meters, which simultaneously recorded ambient weather data.

The total of 10 independent data acquisition systems used IRIG-B GPS timeclocks to allow for post-process synchronization of the recordings. All the systems were managed using the custom Acoustic Field Recorder (AFR) software developed by Brigham Young University and Blue Ridge Research and Consulting LLC. This robust software has been used on previous jet

noise measurements [54, 55], measurements of weapon noise [115], rocket launches and test firings [116, 117] and sonic booms, and is designed for efficient configuration, rapid deployment, and highly scalable systems. It includes options for both level and time-based triggering, and allows for real-time monitoring of levels, spectra, and other statistics.

4.3.4 Weather

In addition to acoustic data, several weather stations, such as the one pictured in Fig. 4.2e, recorded the ambient temperature, relative humidity, and wind speed over the course of the measurement. The measurement was conducted early in the morning (5-7 am local time) to avoid high wind speeds. The temperature and relative humidity varied from 19.9 - 25.8 °C, 21.9 - 31.9 %, while the average wind speed was 1.9 kts over the course of the measurement.

4.4 Near-field

Pressure measurements along the Imaging array give a detailed look into the geometric near field of the noise produced by the aircraft. Figure 4.3 shows the OASPL and skewness of the pressure derivative, $\mathrm{Sk}\{\partial p/\partial t\}$, measured along the array for each measurement for four engine conditions. The $\mathrm{Sk}\{\partial p/\partial t\}$is a statistical measure of the pressure waveform and is indicative of the perception of “crackle”, an annoying component of jet noise which has been under investigation in recent years [118–122].

The variance between measurements is minimal upstream of $x = 25$, though towards the end of the array it becomes large, with pairs of measurements clustering together separate from others. As stated in section 4.3.1, the aircraft powered on, cycled through engine conditions twice, then powered off again. Additional analysis of the exact operating parameters of the engine as well as variance of the weather conditions is needed to understand why individual power cycles would

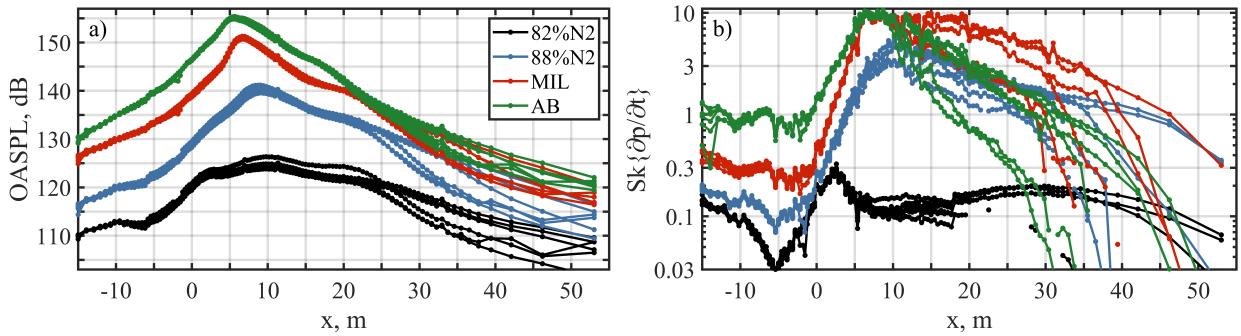

Figure 4.3 a) Overall sound pressure level and b) Sk$\{\partial p/\partial t\}$ values calculated along the Imaging array for each measurement at four engine conditions

cluster the way they did. For the purposes of this paper, however, all subsequent figures will display the mean of the statistical quantities over the 6 runs.

Figure 4.4 shows the spectra (from 0 to 2000 Hz) recorded at each microphone along the 120-channel Imaging array arranged by the x-coordinate of the measurement position. The squared pressures of the spectra are averaged over the 6 runs, and the entire plot is normalized to its peak value for each engine condition to share a common color scale. The engine power and maximum SPL is recorded in the upper right corner of each pane. Colors change in 1 dB increments with contour lines every 6 dB. As has been shown in previous measurements of other high-performance military aircraft, this measurement contains spatiospectral lobes, or local maxima and minima in the space-frequency domain plotted in Fig. 4.4. There is a definite change of structure as engine power is increased among the intermediate conditions, in this case from 82% N2 to 88% N2, where additional high-frequency spatiospectral lobes appear upstream of the main radiation lobe. This mirrors the pattern in the OASPL seen in Fig. 4.3, where there is a large increase in the forward portion of the OASPL between 5 and 10 m downstream.

Generally, the spectra follow classical trends in jet noise, with broad spectra towards the sideline and more peaked spectra towards the aft, with the addition of broadband shock associated noise, BBSAN, radiating in the forward direction at the higher engine powers. However, at all engine

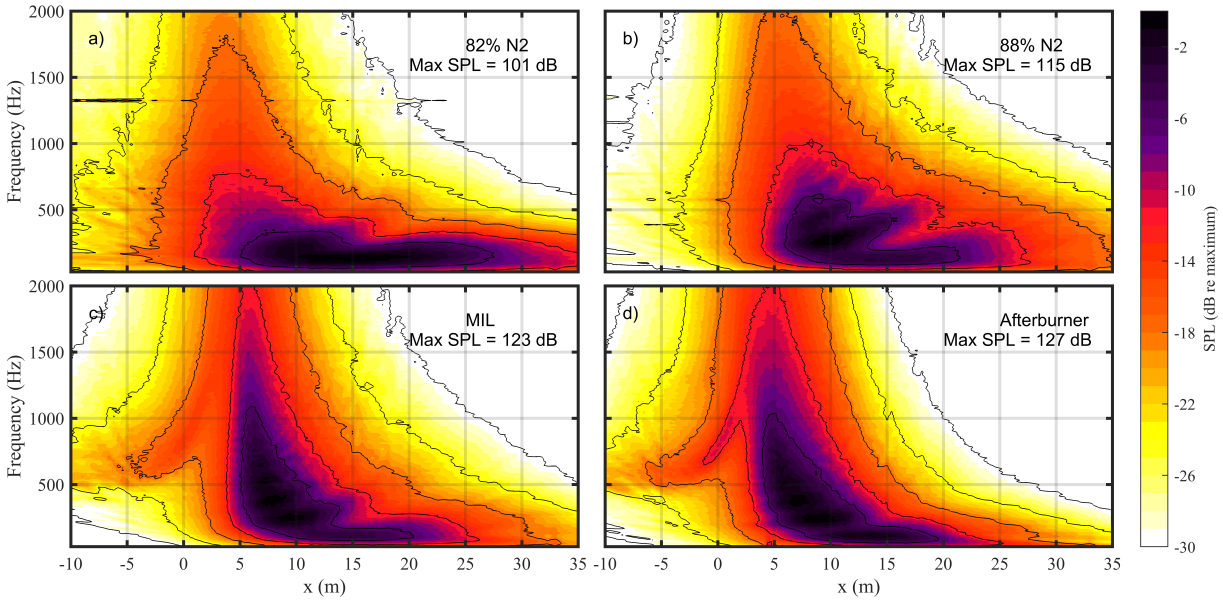

Figure 4.4 Spectra as a function of x-coordinate along the Imaging array for four engine conditions

powers significant deviations from this norm appear in the aft radiation, where multiple peaks in the spectra are seen. The spatiospectral shapes seen in Fig. 4.4 are qualitatively similar to those seen in a similar measurement taken of an F-35B [105, 123].

4.5 Influence of the ground

The Near-field measurements discussed in the previous section were all located on the ground, while the mid to far-field measurements were all taken at a height of $5'$. A first order estimate of the effect of the ground would be a perfect pressure doubling, representing an increase in the OASPL by 6 dB. The measured difference in OASPL between co-located ground and $5'$ microphones are given in Table 4.1, which shows for two different angles the mean and standard deviations of the OASPL differences for the four engine conditions. The OASPL is greater at the ground, though the

difference is as low as 1.1 dB for Afterburner at the 150° location and as much as 4.4 dB at the 88% N2 condition at the 130° location.

Comparison of the ground and 5′ spectra at these different conditions and locations sheds insight into the variance of the OASPL differences. Figure 4.5 shows the spectra at these locations (arbitrary amplitude, offset for clarity) and engine conditions. The solid lines are the spectra measured at the ground and dashed lines measured at 5′. The largest differences in OASPL between the ground and aerial microphones is where the ground reflection null appears at the peak in the spectrum. Because of the frequency-dependant and ambiguous source geometry, very deep nulls are not seen in the ground reflection spectra for many configurations, resulting in much smaller than expected OASPL reductions in the aerial microphones.

Table 4.1 Average OASPL difference between co-located microphone at ground and 5′ heigths for the two Crackle Study measurement locations, denoted by angle, and standard deviations averaged across six runs.

Angle	**82% N2**	**88% N2**	**MIL**	**AB**
130°	3.0 ± 0.2	4.4 ± 0.3	4.4 ± 0.1	4.2 ± 0.1
150°	1.3 ± 0.2	2.2 ± 0.4	1.7 ± 0.2	1.1 ± 0.2

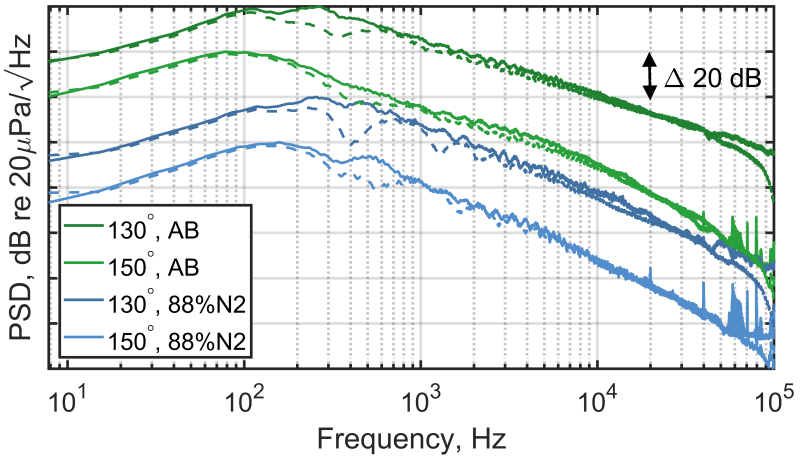

Figure 4.5 PSD for two heights at two engine conditions at two locations. Solid lines denote ground microphone and dashed lines are 5′ off the ground.

4.6 Far-field

The remainder of the presented results were measured 5′ off the ground in the mid to far-field of the aircraft, starting with the 25′ foul line and including the 19.1, 38.1, 76.2, 152, and 229 meter arc arrays. First, two-dimensional maps of the OASPL are generated by interpolating between the measurement points. Figure 4.6 shows the OASPL measured at four engine conditions, normalized to their respective maximum OASPL as displayed in the title. Measurement points are represented by white dots, and major contour lines are drawn every 6 dB below the maximum with minor contour lines every 3 dB. Consistent with other aircraft measurements, the OASPL increases and the directivity peak shifts towards the sideline with increase in engine condition, with a peak near 150° for 82% N2 and shifting to 120° for Afterburner.

Another visualization of the data gathered along the arcs is shown in Fig. 4.7. Each column of plots contains the OASPL (top) and the corresponding $\mathrm{Sk}\{\partial p/\partial t\}$ (bottom) for a given arc. The horizontal axis is the inlet angle, θ, relative to the MARP. The lines show the mean value across the six measurement repetitions and the error bars represent the minimum and maximum recorded

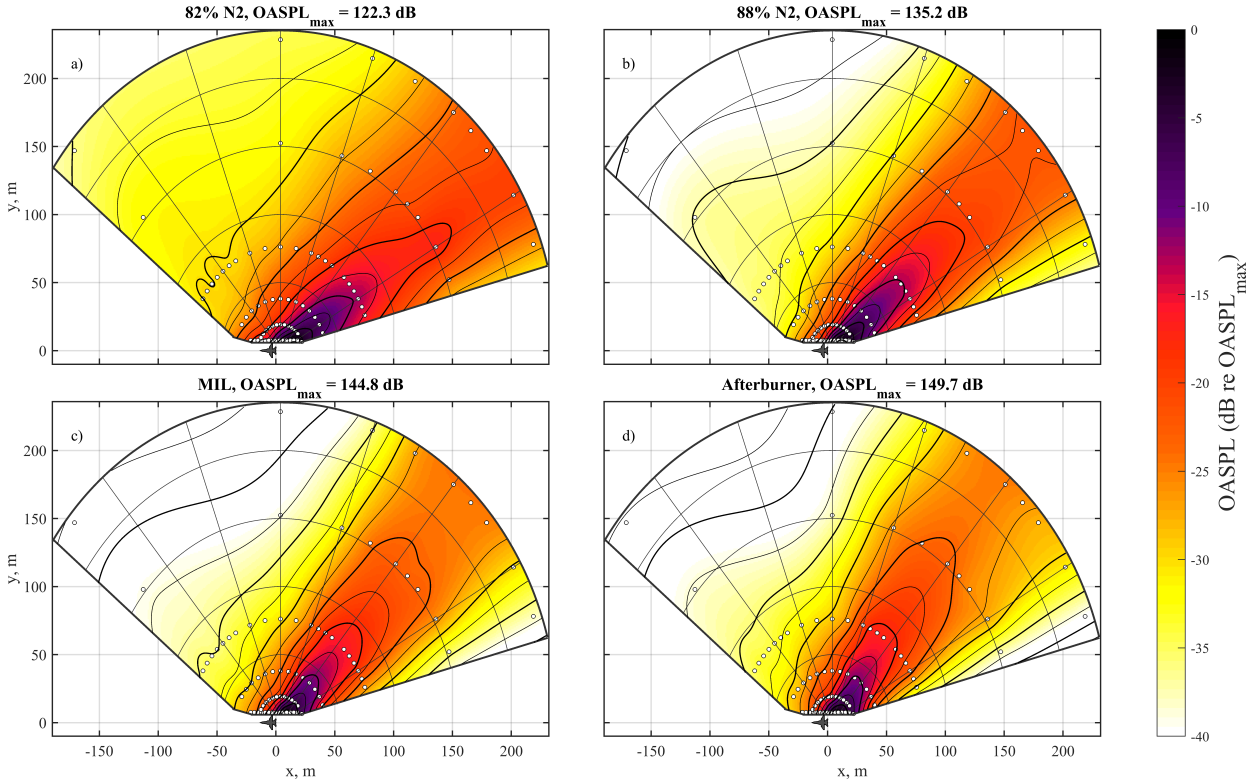

Figure 4.6 OASPL 5 feet off the ground in the mid to far field of the aircraft, interpolated between measurement points.

values. Each separate engine condition is represented by a different color, all on the same scale. The variability across measurements for the OASPL and the Sk$\{\partial p/\partial t\}$ is very low for the 19, 38, and 76 m arcs (noticeably lower than the near-field measurements) but increases for the 152 and 229 m arcs, suggesting that that is where meteorological and terrain effects become important to the propagation.

The directivity trends are easier to compare across engine conditions in Fig. 4.7. Comparisons of the top and bottom rows of Fig. 4.7 show that the Sk$\{\partial p/\partial t\}$ and the OASPL generally follow similar trends, except for 82% N2 in Fig. 4.7f) where the Sk$\{\partial p/\partial t\}$ peaks towards the sideline of the jet. For the OASPL, the peak directivity shifts upstream and broadens with engine condition for each arc, though the broadening and upstream shift is less pronounced at the 152 and 229

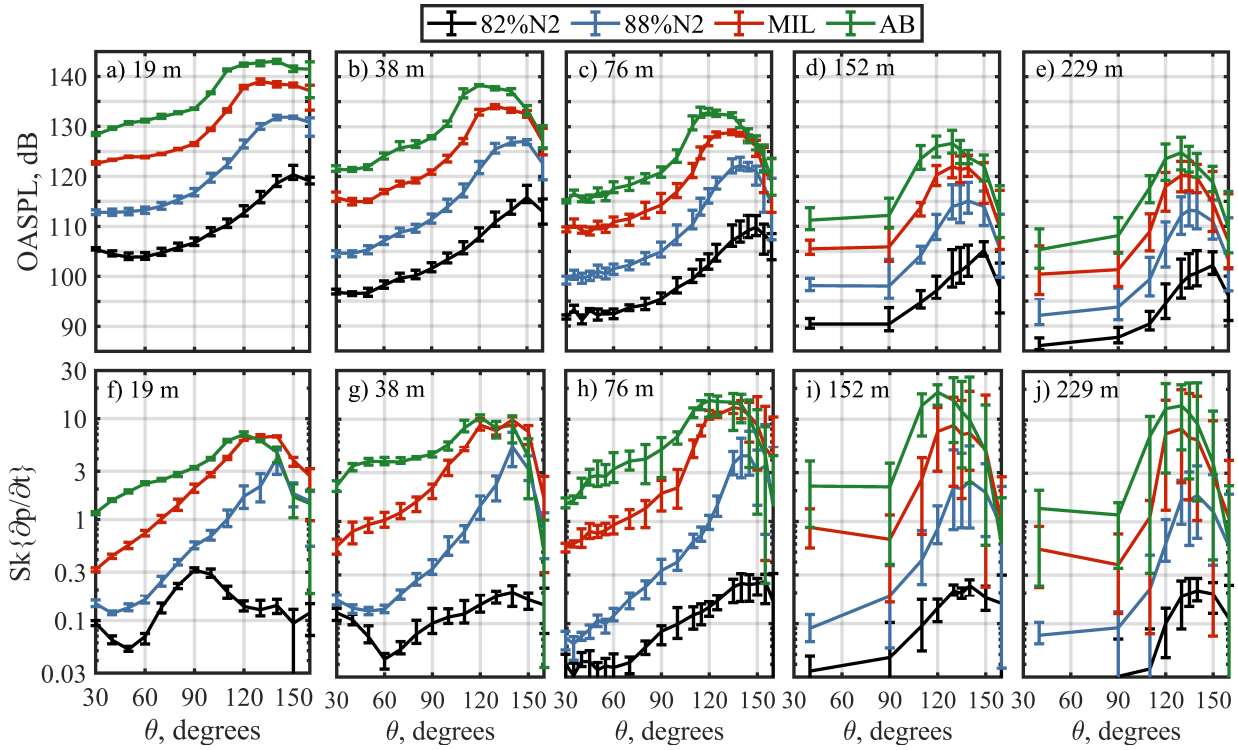

Figure 4.7 OASPL directivities for a) 19 m, b) 38 m, c) 76 m, d) 152 m, and e) 229 m arcs and Sk$\{\partial p/\partial t\}$ directivities for f) 19 m, g) 38 m, h) 76 m, i) 152 m, and j) 229 m arcs. Averages across six runs are shown with error bars denoting the minimum and maximum values across the runs.

m arcs. For any given location, the OASPL increases with engine power, but at some far aft locations, the Sk$\{\partial p/\partial t\}$ is greater at Military power than at Afterburner. This is partially due to the Sk$\{\partial p/\partial t\}$ peak being more broad at the 19, 38, and 76 m arcs for Military power than at Afterburner.

4.7 Conclusions

In this paper, we have reported on an extensive measurement of the noise emissions of a T-7A-installed GE F404 engine at four engine conditions. Over 200 microphones were used to capture levels, spectra, and statistical information in the near and far fields. The measurement design

and procedures are discussed. Overall repeatability across the six run-ups measured is good, but differences increase at far aft angles. Whether these differences are caused by variations in engine performance or propagation environment remains the subject of future work.

Aside from a prior F-35 static measurement in 2013, this is the most extensive run-up measurement of a military jet aircraft. Beyond far-field directivity analyses, the 120-microphone near-field array offers numerous possibilities for performing similar field and source-related analyses as those performed on previous aircraft. These analyses include spectral decompositions by noise source type, obtaining correlation and coherence functions, deriving source characteristics through holography and beamforming techniques, and reduced-order modeling using wavepackets. Use of similar analysis techniques on the T-7A will allow comparisons against other supersonic jet aircraft. Additionally, the fact that F404 engine nozzles have been used in jet numerical modeling and laboratory experiments allows opportunity to make further comparisons and validate the performance of large-eddy simulations and lab-scale rigs.

Appendix

4.7.1 Octave Band spatial maps

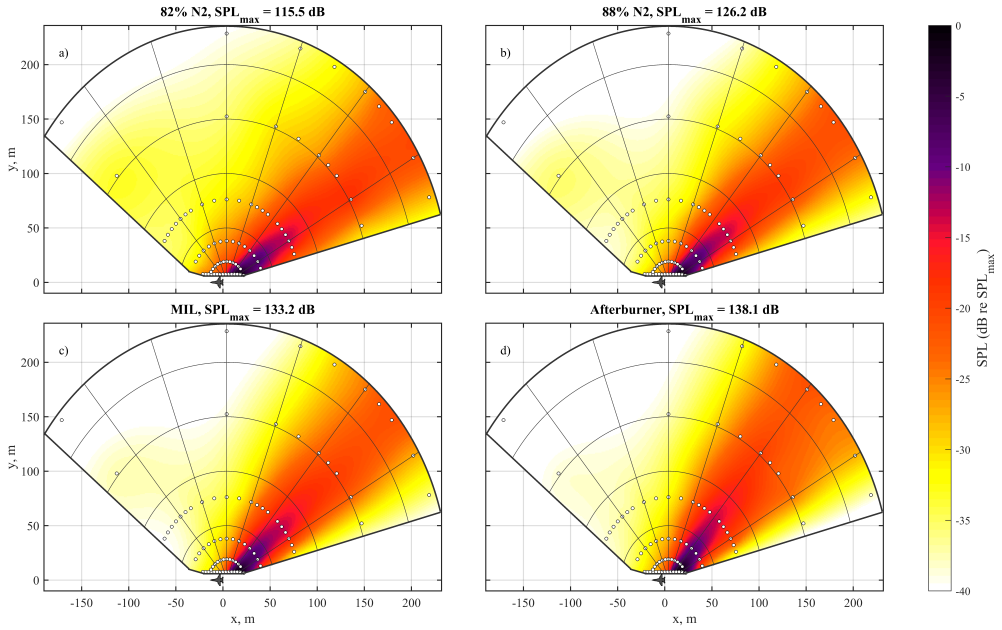

Figure 4.8 Sound pressure level 5′ off the ground for the 125 Hz octave band

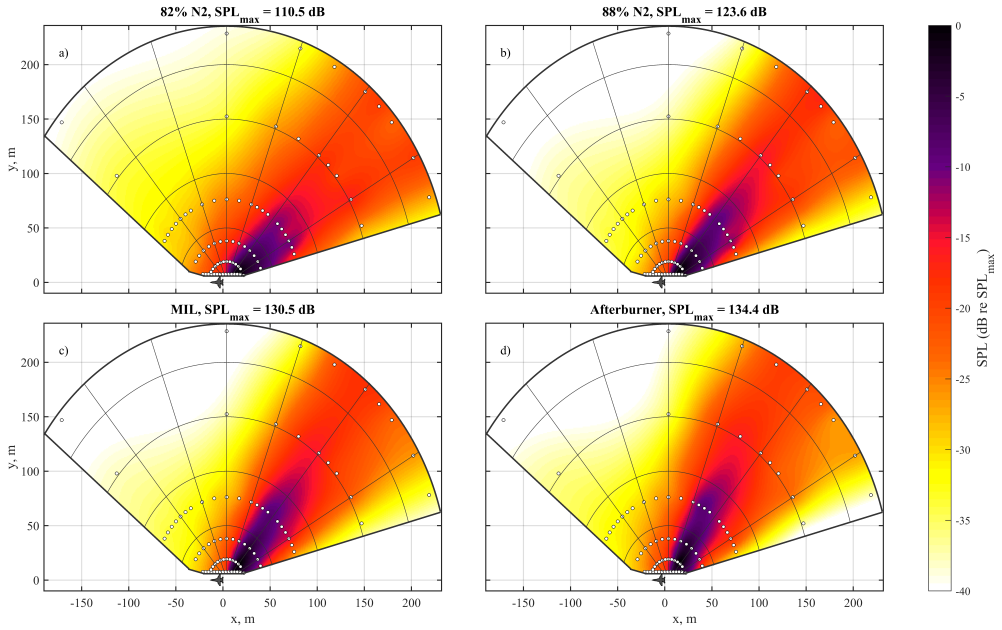

Figure 4.9 Sound pressure level 5′ off the ground for the 250 Hz octave band

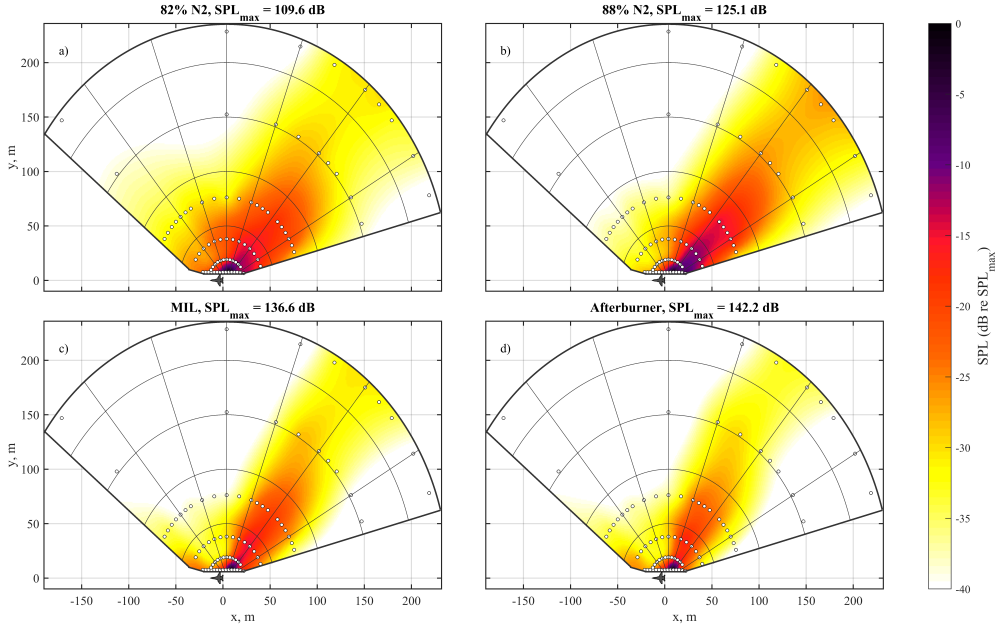

Figure 4.10 Sound pressure level 5′ off the ground for the 500 Hz octave band

Acknowledgments

The authors gratefully acknowledge funding for the measurements provided by Advanced Pilot Training System Program Office and the Air Force Research Laboratory. K. M. Leete and R. D. Rasband were funded by an appointment to the Student Research Participation Program at the U.S. Air Force Research Laboratory, 711th Human Performance Wing, Human Effectiveness Directorate, Warfighter Interface Division, Battlespace Acoustics Branch administered by the Oak Ridge Institute for Science and Education through an inter-agency agreement between the U.S. Department of Energy and USAFRL. Distribution A. Approved for public release; distribution unlimited 88ABW-2020-2171; Cleared 07 Jul 2020.

The authors would also like to thank the 586th Fighter Wing at Holloman Air Force Base for the use of the facilities and all the other individuals from various organizations who came together to make this measurement a success.

Chapter 5

Coherence-based Analysis of a Simulated Highly Heated Laboratory-scale Jet

This work has been published as "Coherence Analysis of the Noise from a Simulated Highly Heated Laboratory-Scale Jet" Kevin M. Leete, Kent L. Gee, Junhui Liu, and Alan T. Wall AIAA Journal 2020 58:8, 3426-3435. I hereby confirm that the use of this article is compliant with all publishing agreements.

5.1 Abstract

Measurements of full-scale, high-performance military aircraft reveal phenomena that are not widely seen at laboratory scales. However, recent modifications to large eddy simulation (LES) methods allow for simulations of jets operating at a high temperature ratio, in a similar regime as military aircraft operating at afterburner. This work applies coherence analyses that have been previously used to study the jet noise field produced by military aircraft to the LES of a highly-heated, laboratory-scale jet. The coherence of the complex pressures along a near-field line approximately parallel to the shear layer as well as along the nozzle lipline shows evidence of

distinct noise production mechanisms which transfer information differently from the flow to the field. A phenomenological comparison between the LES and measurements of an afterburning F-35 aircraft is then made. Though the LES is not run at the exact same conditions as the aircraft and does not reproduce all of the phenomena present in the aircraft's jet noise field, differences between noise production mechanisms observed in the LES may describe some of the spatiospectral lobe phenomena observed in the measurements of the F-35.

5.2 Introduction

The primary source of noise from high-performance military aircraft is the turbulent mixing of the jet exhaust with the ambient air. The complex nature of this sound source results in noise radiated to the aft of the aircraft that has spatially-dependent characteristics: the aft radiation has significant spatial coherence and a peaked spectrum while the radiation more towards the sideline has a broader spectrum with low coherence. Because these two main field regions were found to be consistent between many laboratory-scale jets of different shapes, sizes and speeds, Tam et al. [8] were able to generate similarity spectra fitted to the shape of the measured spectra in the two regions.

To connect the far-field acoustics to the measured jet flow, two-point correlation techniques have been used on laboratory-scale jets [13–15, 124]. This, along with the development of visualization methods [11, 12] of the flow, led to the understanding that the two field regions are attributed to two general noise production mechanisms, fine-scale turbulent structures and large-scale turbulent structures. Fine-scale turbulent structures are understood as small eddies or other perturbations in the mixing region of the flow, which exert an effective turbulence pressure on their surroundings [9, 16]. Large-scale turbulence structures are understood as Kelvin-Helmholtz instability waves generated in the shear layer of the jet at the nozzle [17], which grow as they move downstream. A useful framework for understanding the time-harmonic radiation of the coherent structures is in terms of

a wavepacket model–which has a growth, saturation, and decay of amplitude over space as well as a phase relationship [34]. If the phase velocity across the wavepacket is supersonic compared to ambient conditions, sound is radiated efficiently to the far-field at an angle related to the phase velocity. If the phase velocity is subsonic, the finite size of the wavepacket causes wavenumber leakage, ultimately resulting in only portions of the energy being radiated to the far field.

A difficulty in understanding jet noise has appeared when recent measurement of three different military aircraft [54, 55, 114] showed deviations from the two-source model in the aft radiation of the jet noise. Neilsen et al. [57, 58] and Tam et al. [114] observed errors in similarity spectra fits due to the measurements of the aircraft containing multiple peaks in the spectra of the aft radiation. To investigate the multiple peaks in the spectra of the F-35 [55], Leete et al. [105] used multisource statistically optimized near-field acoustical holography to reconstruct the pressure field surrounding the aircraft. They found that the region of maximum radiation can be represented as a superposition of several "spatiospectral" lobes. Spatiospectral lobes are local maxima in the space-frequency domain, where the spectra from multiple measurements across space are plotted side by side. Subsets of this phenomena are observed as a dual-peaked spectrum at a single microphone location in the field (such as observed by Refs. [57, 114]) or a split directivity pattern in space at a single frequency. The relative amplitudes and spatiospectral slopes of the multiple lobes, which can vary greatly with engine condition, determine the directivity and peak frequency(ies) of the jet noise. Some evidence for these multiple spatiospectral lobes are observed even in engine powers as low as 25% engine thrust request (ETR) for the F-35 [105].

Correlation and coherence analysis applied to field measurements of military aircraft [60, 61] have been useful in characterizing the spatiospectral lobes. Harker et al. [60] showed that the signals recorded in the region of maximum OASPL of a rectangular-nozzled afterburning aircraft have significant correlation with two different time delays, implying that there are two sets of waves with different phase speeds propagating across the array, resulting in different far-field directivities.

For the F-35, Swift et al. [61] showed that the lobes in the spatiospectral domain are mutually incoherent, and there is a measurable coherence between the BBSAN radiating upstream with the spatiospectral content in the aft radiation.

There have been limited reported observations of what could be considered spatiospectral lobes in measurements of laboratory-scale jets. Seiner et al. [125] reported multiple peaks in the directivity in the OASPL as well as at specific Strouhal numbers in Figs. 13 & 17 for a jet of total temperature ratio of 5.4. Another example is seen in the right pane of Fig. 7 of Ref. [87], where a spatiospectral map of the sound pressure levels measured at a dense array parallel to the jet centerline show maxima and minima. It is unknown if the phenomenon has gone largely unreported because laboratory-scale jets do not operate at the conditions required to produce the lobes (high temperature, Mach number, complicated nozzle geometry, etc.) or because many experiments do not sufficiently resolve the spatiospectral domain to observe it.

Large-eddy simulations (LES) of turbulent jets afford the opportunity to produce a finely-sampled spatiospectral domain in the radiated noise as well as simultaneous details about the flow. Efforts in the field over many years have allowed for the increasing accuracy in noise predictions [126, 127]. Within this large body of simulation work, a focus on the use of the simulations to gain insight on noise source mechanisms is abundant. This is generally accomplished by using various decomposition methods [26] to search for coherent wavepacket-like structures, whose radiation can then be interpreted more readily. Some of these methods include data-driven decompositions, such as the field into acoustic, hydrodynamic, and thermal modes using Doak's momentum potential theory [27], the spectral proper orthogonal decomposition (SPOD) [31], and dynamic mode decomposition [32]. Additionally, operator-based analysis such as global linear stability analysis [29] and resolvent analysis [30, 33] can add information about cause and effect relationships within the flow and between the flow and acoustic radiation.

Adaptation of LES to accurately represent conditions of full-scale military aircraft is an ongoing challenge. Liu et al. [39, 40, 91] adapted the Naval Research Laboratory's Jet Noise Reduction, JENRE®, finite-element LES solver to simulate temperatures similar to conditions of high-performance military aircraft at afterburner. Spatiospectral domain analysis of the aft radiation shows a smooth transition from high-frequency components peaking with a directivity at at jet inlet angle of about 115°, to lower-frequency content with a farther aft directivity of about 140° [39]. Based on instantaneous pressure maps of the field, they identify the higher-frequency, upstream content as Mach wave radiation due to its plane-wave like, unidirectional behavior. The lower frequency content which radiates at larger aft angles has a more stochastic radiation pattern with a less defined directivity, which they describe as large-scale turbulent structure noise. This distinction between Mach wave radiation and large scale-turbulent structure noise is new because often those terms are used interchangeably. Although these LES of jet noise with temperature ratio of 7 remain unvalidated due to lack of experimental data at that temperature, other LES studies at that temperature ratio report similar findings [41, 42].

Another example of multiple different source mechanisms contributing to the aft radiation in jet noise is found in the SPOD and resolvent analysis undertaken by Scmidt et al. [31]. They showed the shape and location of modes at frequencies where the field energy is dominated by low-rank behavior. In general, these were shown to fall into two categories: Kelvin-Helmholtz type and Orr [128] type. Kelvin-Helmholtz type wavepacket structures are present in the shear region starting near the nozzle exit and have a high phase velocity, while Orr-type wavepackets are present after the end of the potential core spread over a larger region with a lower phase velocity. With these observations of Scmidt et al. [31] and Liu et al. [39] it then becomes a question of if these source mechanisms are responsible for the spatiospectal lobe behaviour of full-scale military aircraft operating at afterburner.

Since flow measurements are not available for operating military aircraft, flow decomposition techniques to understand source phenomena are not possible, and thus a more roundabout method is needed to understand potential acoustic sources. The goal of this paper is to apply coherence analysis methods previously used to characterize the noise fields of high-performance military aircraft at afterburner [60, 61] to the large-eddy simulations of a laboratory-scale jet operating at a temperature ratio of 7 [39] to understand if the high temperature in the LES can produce spatiospectral lobe content. Of particular interest is the separation of the field and the flow into different regions, the characterization of their properties, then using the coherence between the flow and the field to understand possible noise production mechanisms. Then, spectral and coherence data from an F-35 [55, 61] jet noise field are phenomenologically compared to the LES for potential explanations of the spatiospectral lobe phenomena observed in that aircraft.

5.3 LES of the highly-heated laboratory-scale jet

The LES data set used in this work is provided by Liu et al. [39, 40, 91], which used the Jet Engine Noise Reduction (JENRE®) solver to calculate the heated flow passing through a convergent/divergent nozzle. The JENRE® solver uses a monotonically-integrated LES approach with a flux-corrected transport algorithm [129] and explicit Taylor-Galerkin scheme. Tetrahedral meshes were use to implement the complicated nozzle geometry, which had a nozzle exit diameter, D, of 2.868", a design Mach number of 1.5 and fully-expanded pressure ratio of 3.7. The thermodynamic quantities in the flow region were calculated out to a conical surface outside of the main flow, then the far-field pressures were predicted using the Ffowcs Williams and Hawkings integration method [130]. Cell sizes about $D/286$ are used near the nozzle lip which gradually increase to around $D/20$ near the Ffowcs Williams and Hawkings integration surface. Specifics of the choice of integration surface and grid resolutions can be found in Ref. [131].

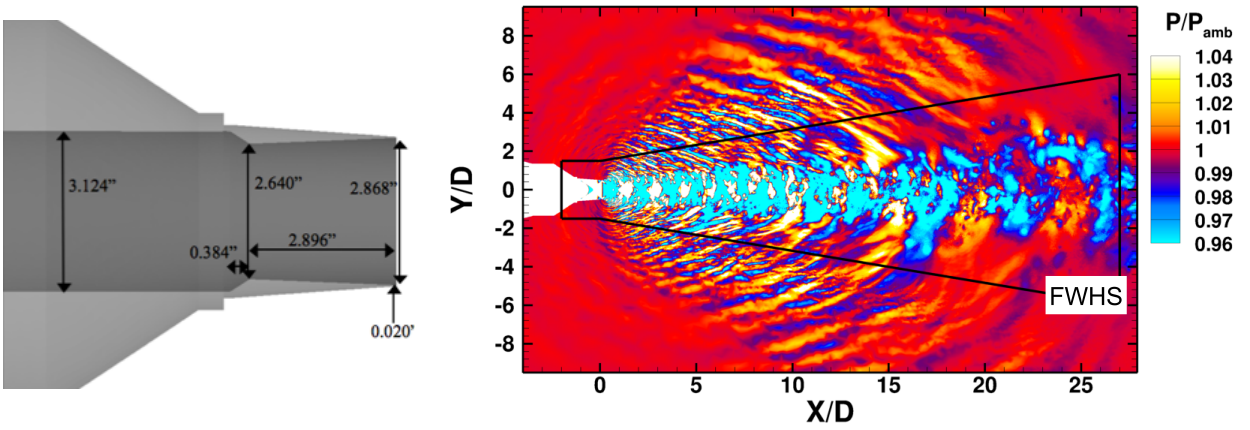

Figure 5.1 Left: Nozzle geometry. Right: representative pressure field of LES simulation. Solid lines show the FWHS.

The simulation was run at a nozzle pressure ratio of 4, a temperature ratio of 7, and a Mach number (referenced to the ambient condition) of 3.38, resulting in an underexpanded, shock containing jet with a temperature in the same regime as high-performance military aircraft operating at afterburner [132]. A method for calculating the temperature-dependent specific heat ratio was incorporated, which was found to match well with NIST databases for air under these conditions (see Fig. 2 of Ref. [39]). Time records of the LES simulation were split into 97 blocks and a Fourier transform applied to each block to give a complex pressure spectrum with a frequency spacing of about 150 Hz. Since the accuracy of the coherence calculation is dependent on the number of simulated measurement blocks and the frequency spacing in the spectra is dependent on the length of each block, it was necessary to run this simulation for much longer than generally is sufficient for analyses of LES. The total temporal duration of the simulation was 0.326 s, which covers 5260 convective time units (D/U_J). The nozzle geometry and a representative pressure field at the test condition used in this study can be seen in Fig. 5.1. Superimposed on the instantaneous pressure map of Fig. 5.1 is the location of the FWHS (solid black lines).

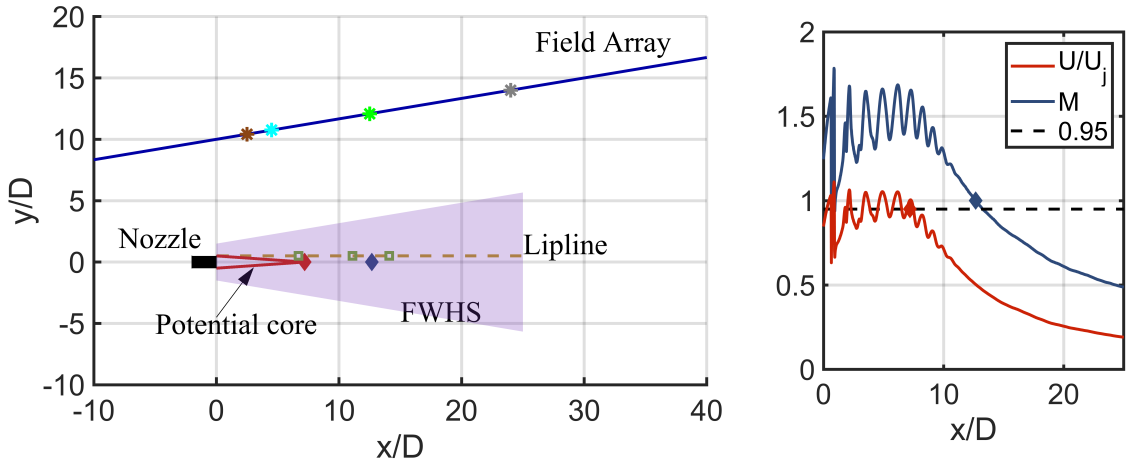

Figure 5.2 Left: Schematic of the nozzle exit location, the two simulated measurement arrays used in this paper, the FWHS, and the approximate location of the potential core. Right: The Mach number (M) and jet velocity ratio (U/U_j) along the jet centerline. The red and blue diamonds show the locations of the end of the potential and supersonic cores respectively.

Figure 5.2 includes a schematic of the simulation with the nozzle exit, the Ffowcs Williams-Hawkings integration surface (FWHS), and two simulated arrays where the field was sampled. All lengths are nondimensionalized by the exit diameter, D, with the flow in the positive x direction and the origin at the center of the nozzle exit. The flow field was sampled along the nozzle lipline of the jet from the nozzle exit to $x/D = 25$. The acoustic field was sampled along the line $y/D = \frac{1}{6}x/D + 10$, from $x/D = -10$ to $x/D = 40$. The right panel of Fig. 5.2 shows the local Mach number of the fluid along the jet centerline (blue) and the ratio of the fluid velocity, U, to the jet velocity, U_j (red). The end of the potential core is estimated as $x/D = 7.2$, where $U/U_j \approx 0.95$ (dashed line) and is marked with a red diamond. The end of the supersonic core is located at $x/D = 12.67$, where $M = 1$ and is marked with a blue diamond.

The normalized sound pressure levels along the field array are pictured in the left pane of Fig. 5.3. The spectra from each simulated array point between 0 and 7 kHz is shown. On the left, upstream of the nozzle exit, broadband shock-associated noise (BBSAN) is seen starting at about 3.5 kHz and shifting up in frequency to 7 kHz at about $x/D = 5$. Overall levels are the highest

between 5 D and 30 D where the directional portion of the turbulent mixing noise is present. From $x/D = 5$ to $x/D \approx 9$, the peak frequency of the spectrum decreases approximately as $1/x$, while from $x/D \approx 9$ to the end of the array the peak frequency decreases approximately as $1/x^2$. The far-field peak in the OASPL is at an inlet angle of 115°.

Work to use LES to predict radiated jet noise fields at these extreme temperatures is ongoing [41, 42, 133]. Because of lack of laboratory-scale experimental data at these high temperatures, direct validation of the simulation at a temperature ratio of 7 has not been completed. However, the LES methodology has been validated up to a temperature ratio of 3 (similar to Military aircraft operating at full power without afterburner) [39], and the peak directivity angle of the aft radiation (115°) agrees well with a predicted value of 112° based on Tam's vortex sheet model for Mach wave radiation [134]. Additionally, Chen and Mihaescu [42] in their simulations of jets at a temperature ratio of 7 show spatiospectral trends in the far-field which qualitatively match those seen here.

5.4 Coherence Analysis

5.4.1 Coherence function

The frequency-dependent coherence function, $\gamma^2(f)$, is a frequency-domain analog of the correlation function, and is defined as

$$\gamma^2(f) = \frac{|G_{xy}(f)|^2}{G_{xx}(f)G_{yy}(f)}, \tag{5.1}$$

where G_{xx} and G_{yy} are the autospectra of arbitrary signals x and y and G_{xy} is their cross spectrum. The coherence is restricted to range $0 \leq \gamma^2 \leq 1$, where a value of one signifies that all of the time-averaged energy in y is linearly related to the energy in x at that frequency, and a value of zero means there is no relation. For two measurement arrays, x and y, the complex pressures are arranged into $m \times n$ (m being the number of elements in the array and n the number of blocks) matrices $\mathbf{P}_x$ and $\mathbf{P}_y$. A coherence matrix, $\mathbf{\Gamma}^2(f)$ whose entries are the $\gamma^2(f)$ between all combinations of points

on two measurement arrays is calculated by

$$\mathbf{\Gamma}^2(f) = \frac{|\mathbf{P}_x\mathbf{P}_y^{\mathrm{H}}|^2}{\mathrm{diag}(\mathbf{P}_x\mathbf{P}_x^{\mathrm{H}})\,\mathrm{diag}(\mathbf{P}_y\mathbf{P}_y^{\mathrm{H}})^{\mathrm{H}}}, \tag{5.2}$$

where $\mathrm{diag}(\cdot)$ signifies extracting the main diagonal of the argument matrix as a column vector, and the magnitude squared ($|\cdot|^2$) and division operations are done element-wise. The i^{th} row of $\mathbf{\Gamma}^2(f)$ is the coherence between the element x_i and all of the y_j's, and the reverse is true for the columns. If x and y is the same array, $\mathbf{\Gamma}^2(f)$ is symmetric, square, and the values along the diagonal are unity.

In Bendat and Piersol [135], equation (9.82) gives the normalized random error of the coherence calculation, $\varepsilon[\gamma^2]$, which is reproduced here as Eq. 5.3,

$$\varepsilon[\gamma^2] \approx \frac{\sqrt{2}(1-\gamma^2)}{\sqrt{n}\sqrt{\gamma^2}}. \tag{5.3}$$

The error is a function of the calculated coherence itself as well as the inverse square root of the number of blocks, n. For the number of blocks used in this study, a coherence estimation of less than $\gamma^2 = 0.02$ results in a $\varepsilon[\gamma^2]$ value greater than 1, meaning the true coherence could be in fact, zero. This gives a practical lower limit to the possible values of γ^2 obtainable in this study, and all plots are limited to show values above this threshold.

A valuable measure of coherence that is often used is the coherence length, L_{γ^2}, which in this work is calculated as the distance between two points along an array in which the γ^2 drops from unity to 0.5. The concept of coherence lengths have been useful for wavepacket models [35, 136] to construct equivalent acoustic sources for jet noise. For comparison across multiple frequencies, L_{γ^2} is normalized by the acoustic wavelength as was done by Swift et a. [61]. If L_{γ^2}/λ is small such that γ^2 decays rapidly over space, it is often necessary to interpolate the calculation of γ^2 between array points to reach an estimation of the true value of L_{γ^2}.

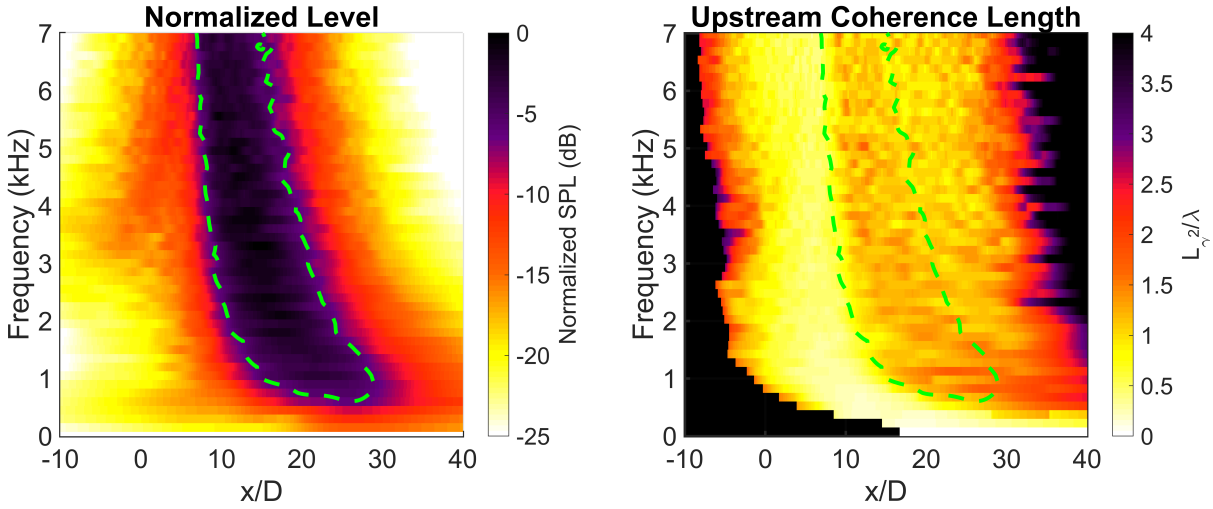

Figure 5.3 Normalized SPL and coherence lengths along the simulated field array between 0 and 7 kHz.

5.4.2 Field Coherence

The coherence matrix of a measurement array in the vicinity of a jet gives insight into the jet noise field properties. Since $\mathbf{\Gamma}^2(f)$ is a large matrix for each frequency, it is difficult to concisely visualize trends across frequencies. The coherence length, L_{γ^2}, then becomes a useful visualization tool. If L_{γ^2} is calculated in a single direction, it allows for a single value to be plotted for each frequency and array position, which can then be displayed in a single figure. Figure 5.3 shows the normalized sound pressure levels along the field array and the corresponding upstream ($-x$ direction) L_{γ^2}/λ. The plot is saturated to black at 4 or when there were not enough upstream microphones in the array to mark a drop in coherence to 0.5. The dashed line marks the level contour 6 dB down from the maximum and is repeated on the plot of the upstream coherence lengths for reference. This spatiospectral region is referred to as the region of maximum radiation in this work.

In Fig. 5.3, the largest values of L_{γ^2}/λ are found aft of $x/D = 30$, which appears to be due to the array being large compared to the aeroacoustic source, causing the propagating acoustic waves to impinge at grazing incidence. When this occurs, the coherence along subsequent points in the array

are large, as the information in the field is transported along the array. Upstream of $x/D = 0$, L_{γ^2}/λ is large in the 3-5 kHz band where the BBSAN signature is seen and increases towards the edge of the array. Coherence lengths are the lowest at about $x/D = 10$, where the radiation towards the sideline is broadband. In the maximum radiation region coherence lengths generally stay between 1-2 wavelengths. At 0.5-1.5 kHz, there is a general increase in L_{γ^2}/λ downstream of 20 D which continues to the end of the array. As frequency drops to zero and wavelengths become very large compared to the dimensions of the jet flow, normalized coherence lengths naturally drop to zero.

Though L_{γ^2} serves as a useful glance at the entire field in one plot, the full story of the field is only told by analysis of $\mathbf{\Gamma}^2(f)$. A single column of $\mathbf{\Gamma}^2(f)$ can be extracted for each frequency and compiled to create a coherence spectra of the array to the reference point corresponding to the chosen column. Parts a)-d) of Fig. 5.4 display the coherence spectrum of the array with respect to four reference points located at $x/D = 2.5$, 4.5, 12.5, and 24 respectively. These points were chosen to represent phenomenological trends observed as the coherence was examined for all points along the array. The vertical dotted lines represent the location of the reference, and their color matches the four asterisks marked on the field array in Fig. 5.2. The coherence spectrum in Fig. 5.4 a) uses a reference chosen where the BBSAN signature is observed in Fig. 5.3. Faint traces of coherence can be seen between the reference point and 10 D downstream between 4 and 6 kHz. This faint trace of coherence is in the frequency range where the BBSAN level is the largest at the reference. Figure 5.4 b) shows the coherence spectrum with a reference point chosen where the coherence lengths in Fig. 5.3 were the lowest, just upstream of the region of maximum radiation. The coherence is small across all but the lowest frequencies.

Figure 5.4 c) shows the coherence of the array with a reference located in the maximum radiation region. The coherence is generally larger than seen in parts a) and b) as well as over a larger spatial extent, as is seen by the increase in L_γ^2/λ in Fig. 5.3. What is unseen in Fig. 5.3 is that in the region of maximum radiation, a single point in space contains frequency information that is coherent with

the upstream BBSAN signature. Coherence between the BBSAN and the region of maximum radiation implies that either the BBSAN source is propagating downstream into the region of maximum radiation as well as upstream, or the source mechanisms (BBSAN source and the source contributing the region of maximum radiation) are not independent. An example of the sources not being independent could be if the actuation of the shock cells by instability waves [19] were to transfer some of the shock fluctuation information to the acoustic field via their Mach wave radiation. The coherence alone cannot distinguish between these two possible explanations. Swift et al. [61] shows a similar pattern with their coherence analysis of the F-35.

Part d) of Fig. 5.4 shows that as the reference point is moved farther downstream, the coherence of the field increases with a larger increase in the 0.5 to 1.5 kHz range. Even though the reference is not completely removed from the region of maximum radiation, any evidence of coherence with the BBSAN disappears. It is possible this is caused by some change in the source mechanism responsible for the radiation to the field in that direction, though there is some common coherence between parts c) and d) below 1 kHz. The coherence for frequencies above 1 kHz begin to saturate downstream of 25 D.

These observations of the field coherence allow for the separation of the field into four regions:

1. Region where the BBSAN signature dominates. The frequency-dependent signature peaks at a lower frequency upstream and shifts to higher frequency towards the sideline. Underneath the BBSAN there is uncorrelated noise present, so the coherence drops outside of the frequency band where the BBSAN peaks.

2. Region of low coherence, upstream of the contribution of the aft radiation and downstream of the BBSAN component.

3. The portion of the region of maximum radiation that shows traces of coherence with the BBSAN in region 1.

4. The portion of the region of maximum radiation where the coherence with region 1 disappears until the end of the array.

Regions 1, 3, and 4 as identified by the field coherence can be qualitatively observed in the instantaneous pressure map of Fig. 5.1. Upstream radiation not originating from the nozzle exit is seen characteristic of BBSAN. Highly directional, plane-like propagation of the waves originating from the plume upstream of the supersonic core are reminiscent of Mach wave radiation. Downstream of that, however, the radiated field looks significantly different. This observation motivates section 5.4.4, which uses the coherence between the pressures on the field array and the flow pressures along the nozzle lipline to identify source regions responsible for each of these identified field regions.

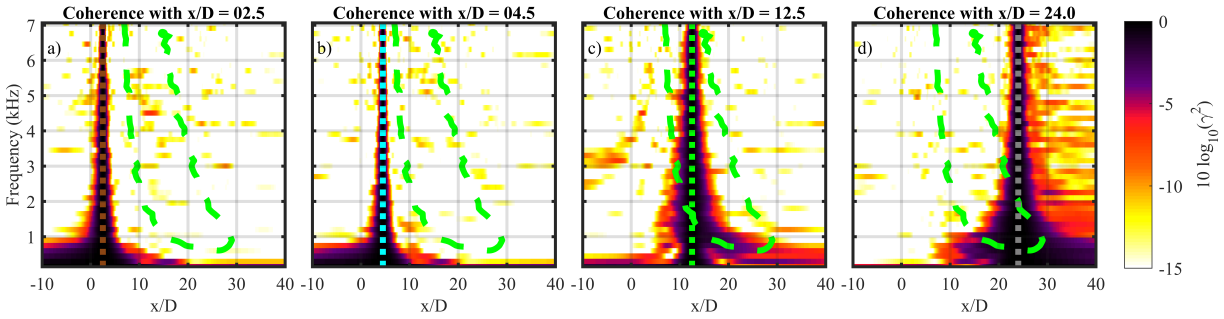

Figure 5.4 Coherence of the field array with four different reference points along it: $x/D = 2.5$, 4.5, 12.5, and 24. The colored dotted lines represent the reference locations and correspond to the colored asterisks on Fig. 5.2.

5.4.3 Flow Coherence

The advantage of investigating LES as opposed to full-scale aircraft is that flow velocities and pressures are known. Thus, the same coherence analysis that was performed on the field can be repeated for the pressures along the nozzle lipline. Figure 5.5 shows the normalized sound pressure levels (left) as well as the normalized upstream coherence lengths (right) along the nozzle lipline.

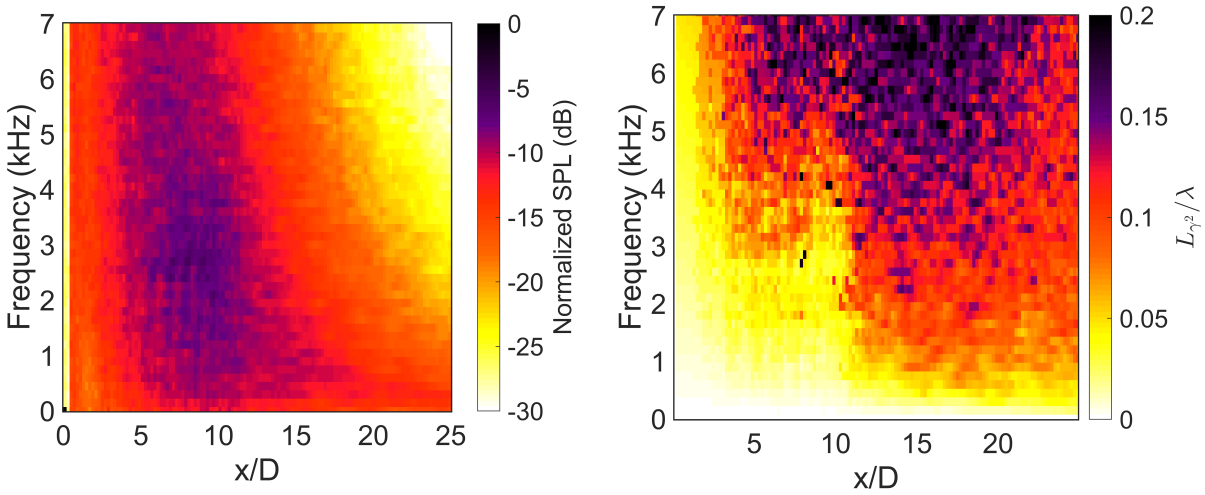

Figure 5.5 Level and normalized coherence lengths of the pressures along the nozzle lipline.

The wavelength used for normalization is the acoustic wavelength calculated using the local sound speed, $c = \sqrt{\gamma RT}$, where γ and T are respectively the ratio of specific heats and temperature, both of which vary with location, and R is the specific gas constant for air. The maximum levels along the lipline in Fig. 5.5 are between 3-15 D downstream of the nozzle. Downstream of 15 D, levels decrease at all frequencies, with the lowest frequencies decaying the slowest. At frequencies below 3.5 kHz and between 3 and 10 D, there are vertical stripes in the level that appear to be due to the influence of the shock cells seen in the fluctuations in Fig. 5.2. Coherence lengths start small at the nozzle exit and quickly increase as the reference is moved downstream, with larger normalized coherence lengths at high frequency. From 3 to 10 D, the coherence lengths are shortened at frequencies below 4 kHz. This is in the same region that vertical striations are visible in the level and where shock cells are present.

5.4.4 Coherence Between the Flow and the Field

Though coherence does not necessarily imply a cause and effect relationship, coherence between quantities in the flow and in the field show where similar information is included. First, $\mathbf{\Gamma}^2(f)$ is calculated between the sampled nozzle lipline positions and the field array. Each column (or row) of $\mathbf{\Gamma}^2(f)$ then represents the coherence between a single reference on one array to the entirety of the other. To gain an idea of where the information in the field originates in the flow, for each point along the field array, the frequency-averaged coherence was calculated with the pressures along the nozzle lipline. Each colored line in Figure 5.6 a) is the frequency-averaged coherence with respect to a particular reference point along the field array, the position of which is indicated by the color bar. For upstream references in the field (dark blues), the average coherence is low, with a small rise above the noise floor between $x/D = 5$ and 10 along the lipline. For references between $x/D = 5$ and 20 on the field array (light blues, teals, greens, and yellows) the coherence peaks, shifts downstream, and decays; all while maintaining a similar width. For references beyond $x/D = 20$ along the field array, the coherence peak widens, lowers in amplitude, and settles around $x/D = 15$ along the nozzle lip.

To visualize this transfer of information from the flow pressures to the field pressures, Fig. 5.6 b) shows a schematic of the jet with lines traced from points along the field array to the corresponding points on the nozzle lipline where the frequency-averaged coherence (plotted in part a)) peaks. Because the curves in Fig. 5.6 a) are quite noisy, they were each smoothed and fit to a sum of two Gaussians, and the peak of the fitted curve was used. The peak of the coherence between field region 1 and the nozzle lipline falls between $x/D = 6$ and $x/D = 7.2$. The region of maximum radiation, which in Fig. 5.3 is seen as between $10 < x/D < 30$ on the field array, shares information with the flow region $5 < x/D < 14.5$. Aft of the region of maximum radiation (x/D >30, the red lines), the peak of the coherence all originates from a compact region around $x/D = 15$ along the nozzle lipline, though as seen in Fig. 5.6 a) the relatively low coherence persists over a large area surrounding

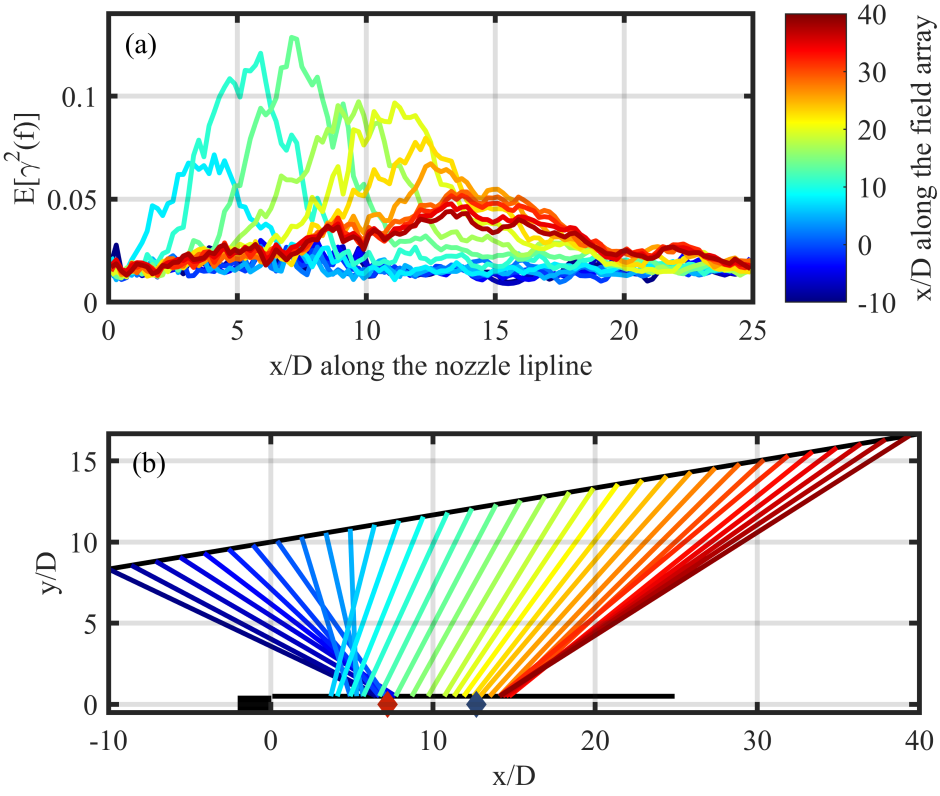

Figure 5.6 Part a) The frequency-averaged coherence between a reference point along the field array (indicated by color) and sampled points along the nozzle lipline. Part b) Lines traced between points along the field array and the corresponding point of maximum frequency-averaged coherence along the nozzle lipline.

that point. Region 2 in the field is characterized by low field coherence, and subsequently has low coherence between the field and the nozzle lipline and does not have a traceable corresponding flow region. Its influence is seen as extra disorder in the traced lines in the transition from region 1 to region 3.

The cyan, green, and yellow lines in part b) of Fig. 5.6 all share a similar slope and do not cross, suggesting that the radiation is superdirectional in that portion of the field. In conjunction with the coherence lengths observed in Figs. 5.5 and 5.3, the source could be described as a multiplicity of spatially-ordered, overlapping source regions (not unlike wavepackets) each with some sort of self-coherent phase relationship causing directional radiation (e. g. Mach wave radiation) that

propagates to the field. Beyond the end of the supersonic core, however, the qualitative nature in the transfer of information from near to far field changes. The entirety of the field array beyond $x/D = 30$ contains information from an extended region centered around $x/D = 15$ (just beyond the end of the supersonic core) along the lipline. It appears that the nature of the sound radiating from this region of the nozzle lipline switches to be more omnidirectional, instead of the highly directional radiation seen farther upstream. This switch explains why the aft portion of the field array has an increase in coherence as seen in Figs. 5.3 and 5.4. Omnidirectional radiation combined with the angle of the field array results in a small angle of incidence of the sound field at the far aft locations.

Based on Fig. 5.6, there appears to be three important regions in the flow:

1. Potential core region, where both the BBSAN and the directional, aft radiation are originating.

2. Region downstream of the potential core but upstream of the end of the supersonic core, where unidirectional radiation dominates.

3. Region downstream of the supersonic core.

To look for phenomenological differences in these regions of the flow, three references were chosen along the nozzle lipline with which to calculate the coherence spectrum with the field array. The first two were chosen as where the field array references for parts c) and d) of Fig. 5.4 trace back to the nozzle lipline via the analysis in Fig. 5.6 ($x/D = 6.7$ and 11.1, respectively). The third reference is where the farthest aft point on the field array traces back to the nozzle lipline, $x/D = 14.1$. Figure 5.7 shows the coherence spectrum of the field array with these three reference points along the nozzle lipline, with the 6 dB-down region of the levels as displayed in Fig. 5.3 for scale.

Figure 5.7 a) shows the coherence between $x/D = 6.7$ on the nozzle lipline, representing flow region 1 and the entirety of the field array. This position in the flow transmits information to the

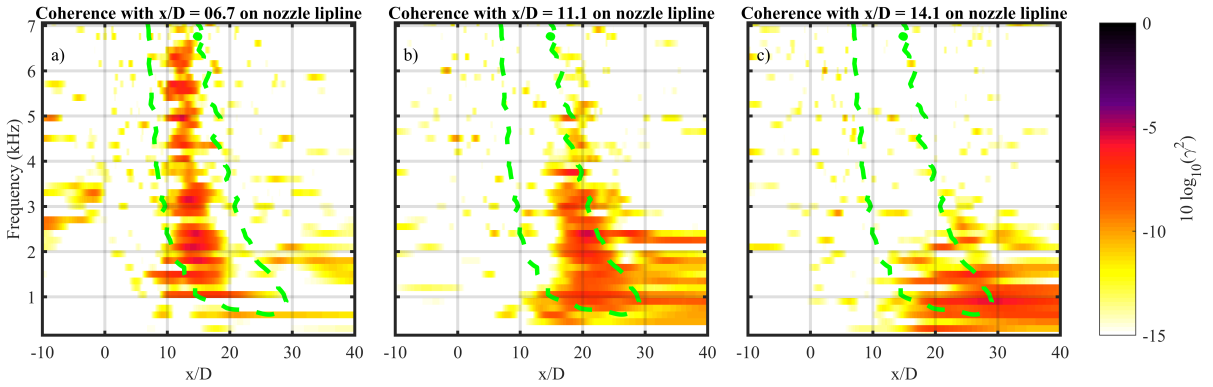

Figure 5.7 Coherence between select points along the nozzle lipline (marked on Fig. 5.2 by the hollow squares) and the field array.

acoustic field both upstream as BBSAN and downstream to the region of maximum radiation as Mach wave radiation. The transmitted information to the region of maximum radiation seems to segment itself into spatiospectral minima and maxima, with individual frequency bins dropping to low levels in the region. This is the first hint of spatiospectral lobe separation in the region of maximum radiation seen in this data set. Part b) shows the coherence spectrum of the field array with $x/D = 11.1$ at the nozzle lipline, which is a point between the end of the potential core and the end of the supersonic core, outside of the influence of shock cells. All evidence of coherence with the BBSAN region upstream disappears and the spatiospectral region with appreciable coherence fills out the region of maximum radiation that is not covered in part a), with the addition of some low-frequency content. Part c) uses a reference at $x/D = 14.1$, which seems to influence the field in a different way than parts a) and b). The coherence consists of low frequencies (predominantly under 2 kHz) and is spread over a larger spatial region in the field. It does overlap with some of the low frequency portion of part b), which suggests a gradual transition between the source mechanism responsible for the unidirectional radiation in parts a) and b) to this qualitatively different phenomenon in part c). This gradual transition between source mechanisms is supported by the red lines in the frequency-averaged coherence in part a) of Fig. 5.6. References at the end of the

field array contain information from an extended region along the nozzle lip – on the order of ten diameters wide.

The qualitative difference between the radiation originating upstream of and downstream of the supersonic core is easily described with the wavepacket analogy for jet noise [34]. If a wavepacket-type source description is used and is situated sufficiently upstream of the end of the supersonic core, then the phase relationship of the coherent wavepacket would likely be supersonic, which results in efficient, directional Mach wave radiation. As the jet velocity decelerates with distance from the nozzle exit, however, the effective convective velocity decreases to subsonic, causing the phase speed of their wavepacket representation to be subsonic as well, resulting in only a portion of their wavenumber spectrum radiating efficiently with a more omnidirectional directivity.

5.4.5 Coherence Analysis Summary

Combining the observations of the field, flow, and flow-to-field coherence calculations leads to a combination of four possible noise mechanisms in this simulation of a highly-heated laboratory-scale jet.

1. BBSAN
2. Fine-scale turbulent structure noise
3. Mach wave radiation from large scale turbulent structures
4. Large-scale turbulent structure noise

The BBSAN component is a well-documented and understood phenomenon which radiates primarily upstream (field region 1), though this work shows that portions of the aft radiation (field region 3) is coherent with the BBSAN. It is unknown if this is because the BBSAN radiates downstream as well as upstream, or if the large-scale turbulent structures which actuate the shock

cells imprint the shock cell information into the far-field via their Mach wave radiation. Fine-scale turbulent structure noise is present as a background to the BBSAN components and dominant just upstream of the region of maximum radiation (field region 2). Mach wave radiation of large-scale turbulent structures is seen as nearly unidirectional radiation originating from the flow upstream of the end of the supersonic core (flow regions 1 and 2) and radiating to the upstream portion of the region of maximum radiation (field region 3). A qualitative description of this source mechanism is of spatially-ordered, partially-overlapping wavepackets on the order of a few diameters in width with supersonic phase velocity. Though each wavepacket would be self coherent, coherence lengths are small (as seen in Fig. 5.5) because they are spatially compact.

The final noise mechanism discussed in this paper originates from the region of the flow which is centered around the end of the supersonic core (region 3), but which extends both upstream into region 2 and even farther downstream. It contributes to the latter half of the region of maximum radiation all the way to the end of the field array (field region 4) and is comprised of low-frequency components, primarily under 2 kHz or a Strouhal number of about 0.12. A wavepacket description would be a set of spatially large, self coherent but mutually incoherent wavepackets which overlap, resulting in nonzero coherence lengths because of their size. Here, it is simply called large-scale turbulent structure noise, similarly to previous work on this data set [40] and other works which use LES to simulate high-temperature jets [42].

The two different source phenomena responsible for the aft radiation as seen in this work are remarkably similar to the results of Schmidt et al. [31], which analyzed LES of subsonic and supersonic cold jets using SPOD and resolvent analysis. They found that the SPOD and resolvent modes take on wavepacket shapes which are qualitatively similar to the two source mechanisms described here, and are dubbed Kelvin-Helmholtz type or Orr-type. The Kelvin-Helmholtz type wavepackets originate along the upstream shear layer and are responsible for the majority of the radiation, while the Orr-type wavepackets are primarily active downstream of the potential core at

lower frequencies. The Orr-type modes are not low-rank, but are extended over a region and require many overlapping suboptimal modes to predict the overall response. The physical mechanism attributed to these modes is the Orr mechanism [128]. The characterization of this superposition of overlapping self-coherent modes to produce the field is important to linear analyses [30], which have had difficulty reproducing the far aft, low-frequency radiation. Adding coherence decay to wavepacket models [136] to the nominally coherent linear analyses is required to match the radiated field at large aft angles and low frequencies.

Table 5.1 Summary of the jet noise components observed by the coherence analysis and their estimated regions along the nozzle lipline and field arrays.

Noise Component	Flow extent	Field extent
BBSAN	$6 < x/D < 7.2$	$x/D < 2$
Fine-scale turbulent structure noise	-	$2 < x/D < 5$
Mach wave radiation	$x/D < 12.67$	$5 < x/D < 25$
Large-scale turbulent structure noise	$7.2 < x/D < 20$	$20 < x/D$

5.5 Comparison to the F-35B

High-fidelity measurements of the jet noise produced by military aircraft have been achieved in recent years [54, 55]. Analyses of near-field measurements of the noise from a tied-down F-35B aircraft have shown significant deviation from the traditional two-source model [61, 105], and are phenomenologically compared to the LES of the highly-heated jet here.

The measurement of the F-35B was performed at Edwards Air Force Base in 2013 [55]. The aircraft was tied down to a concrete run-up pad and its engine cycled from 13% engine thrust request (ETR) up through 150% ETR. Engine powers greater than 100% ETR are due to the addition of afterburner. The nozzle of the engine was 2.0 m from the ground and had a nominal 1 m diameter,

though the exact nozzle diameter changed with engine condition. The origin of the coordinate system used in this study is at the nozzle exit with the jet plume faced down the positive x-axis. The y-axis is the distance from the jet centerline and the z-axis is the height above the ground. The array was laid out to the left side of the aircraft as shown in Ref. [55], though for convenience it is mirrored to show it on the right side of the aircraft. This study focuses on a 32 m long, 71-element (0.45 m inter-element spacing) linear ground array placed approximately parallel to the shear layer, which is shown in Fig. 5.8. The recorded 30-second time waveforms (204.8 kHz sampling frequency) were split into multiple blocks with a 50% overlap, windowed with a Hann function, then the Fourier transform was applied to each block. Swift et al. [61] analyzed the full, high-resolution data set. For this work, to be able to compare more closely with the LES of the heated laboratory-scale jet, the block size was adjusted to give a frequency resolution of 15 Hz and only 97 blocks were used.

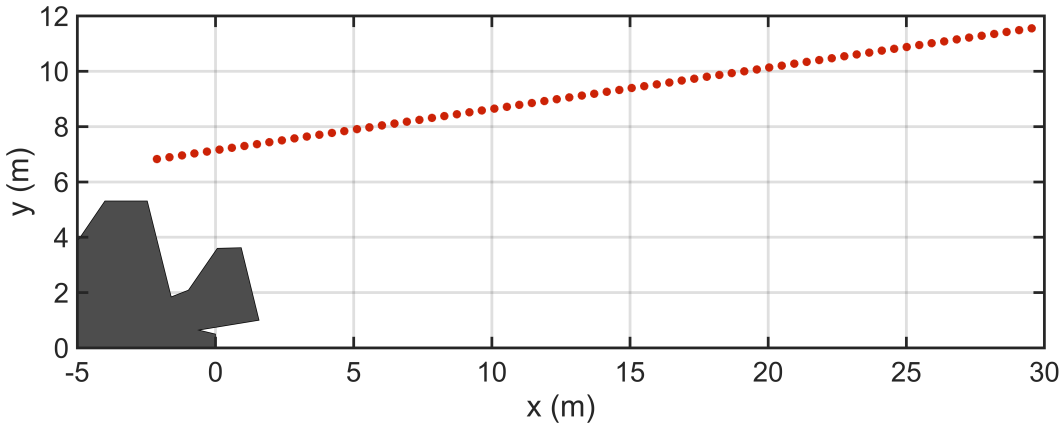

Figure 5.8 Schematic of the linear ground array used to measure the jet noise field of the F-35B.

The temperature ratio in the LES analyzed in this study was chosen to be similar to a tactical aircraft operating at afterburner, so the 150% ETR case of the F-35B measurement is studied here. The only attempt to scale either data set for comparison was the normalization of levels and choice of frequency range and resolution. The normalized spectrum measured along the array is displayed

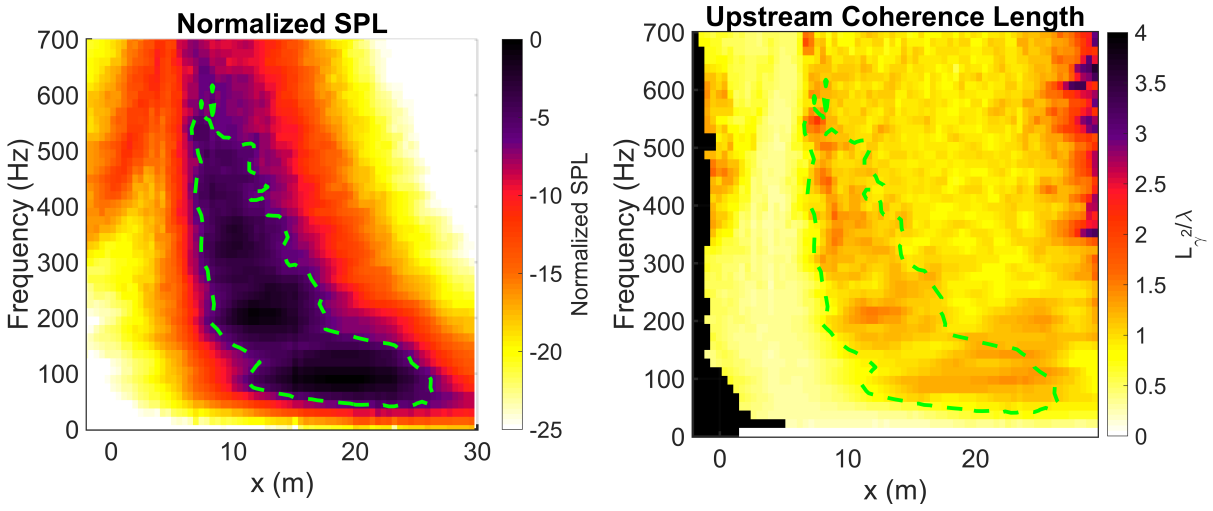

Figure 5.9 Normalized SPL and coherence lengths measured by the array in Fig. 5.8 while the F-35B aircraft was operating at 150% ETR.

in the left pane of Fig. 5.9. BBSAN is seen upstream starting at 350 Hz, increasing to 700 Hz at $x = 5$ m. The directional portion of the turbulent mixing noise dominates from 5-30 m downstream.

The calculated upstream coherence lengths for the F-35B measurement were first shown in Ref. [61] and are repeated here in Fig. 5.9 (though this study uses a coarser frequency resolution for comparison to the LES). The coherence lengths are large upstream in the 300-600 Hz band due to the presence of BBSAN, become uniformly smaller in the region dominated by sideline radiation and increase again in the region of maximum radiation. Aft of the region of maximum radiation, at high frequencies at the end of the array, the frequencies above 350 Hz begin to saturate, likely due to the array measuring a progressive wave field since it is large compared to the aeroacoustic sources. A striking feature of Fig. 5.9 is the oscillation in the level and the coherence length in the region of maximum radiation. This oscillation in the region of maximum radiation can modulate the level on the order of 5 dB and double the value of L_{γ^2}/λ. The oscillations in the spatiospectral domain are called spatiospectral lobes. These spatiospectral lobes were investigated more in depth by Refs. [36, 61, 105]. They represent either a dual peak in the frequency spectrum at a single measurement location or a split directivity pattern in the field at a single frequency.

Despite the fact that the operating conditions and nozzle geometries of this LES data set and the F-35 are not the same, general comparisons of the levels and coherence lengths are still favorable. All the coherence length trends appear to hold generally, except that L_{γ^2}/λ is slightly larger for the LES than for the F-35. The largest difference is, of course, the spatiospectral lobe content in the F-35. It is unknown at this point why the LES does not contain this phenomenon. In Fig. 5.3, the coherence lengths inside and just aft of the region of maximum radiation above 2 kHz are about the same, in Fig. 5.9 for the F-35 the coherence lengths are larger at the spatiospectral lobe peaks, almost as if an additional coherent noise source were superimposed on top of the general field. However, the horizontal portion of the farthest aft lobe of the F-35 matches the low-frequency, aft frequency content seen in the LES.

Since the F-35 measurement did not include flow measurements of the flow, other studies have used acoustic inverse methods in an attempt to identify source regions for the noise measured along this array. Leete et al. [105] (Chapter 2) used an advanced acoustical holography technique to reconstruct the acoustic field of the F-35 from this same data set from the nozzle lipline out to a large area surrounding the aircraft. Though limited to frequencies below 400 Hz, they were able to trace individual spatiospectral lobes to their apparent origins along the jet centerline. The low-frequency, far aft spatiospectral lobe was traced to a source location downstream of $x/D = 12$, while the next two lowest lobes were traced to the an upstream region between $x/D = 5$ and $x/D = 10$. The low-frequency lobe also had an appreciably shallower directivity than the two higher lobes. When compared with the current work, the lowest frequency, farthest-aft lobe could be identified as large-scale turbulent structure type radiation while the higher-frequency lobes could be identified as Mach wave radiation.

5.6 Conclusions

Level and coherence analyses of the simulated noise from a highly-heated jet leads to the identification of distinct regions of interest in the flow and in the field. Field region 1 is characterized by the presence of BBSAN, where the spatially-dependent self-coherent spectra appears upstream. The BBSAN information originates from the nozzle lipline in flow region 1, which is upstream of the end of the potential core. Field region 2 is the region of low coherence towards the sideline of the jet, just upstream of the region of maximum radiation. Field region 3 is the upstream portion of the region of maximum radiation. It is self-coherent and partially coherent with the BBSAN upstream. It originates from flow region 1 as well as flow region 2, which is between the end of the potential and supersonic cores. Field region 4 begins with the low-frequency portion of the region of maximum radiation and extends downstream to the end of the array, and contains information from flow region 2 as well as region 3, which is downstream of the supersonic core.

Analysis of the transfer of information between the nozzle lipline and the field array illuminates four different potential noise mechanisms at play in this jet. Broadband shock-associated noise, fine-scale turbulent structure noise, Mach wave radiation of large-scale turbulent structures, and large-scale turbulent structure noise. Traditionally, the directional radiation in the aft direction has been attributed solely to the Mach wave radiation of large-scale turbulent structures. It is seen with this LES that the large-scale turbulent structure noise originating from the supersonic portion of the flow transmits its energy more efficiently to the field in the characteristic unidirectional pattern associated with Mach wave radiation. However, as the jet velocity decreases with distance from the nozzle, a qualitatively new noise source begins to appear where the frequency content shifts lower and the directivity becomes more omnidirectional. This noise source is centered just downstream of the end of the supersonic core, though it is on the order of 10 diameters wide.

Though the idea of multiple noise production mechanisms contributing to the aft radiation is heartening for understanding the spatiospectral lobes measured in the F-35 field, the observations of

the LES only show a smooth transition from one noise production mechanism to another, which does not generate a split directivity in the field or a dual peak in the spectrum. However, previous work [61, 105] has shown qualitative similarities between the farthest aft lobe of the F-35 with the Large-scale turbulent structure noise observed in this study and the coherence calculated between a point in the flow where shock cells are present does split the Mach wave radiation component into what looks like spatiospectral lobe shapes. At this point, bringing LES of a laboratory-scale jet to high temperatures (designed to be in the same regime as high-performance military aircraft operating at afterburner) does not account for all of the spatiospectral lobe content that is observed in the F-35. Additional laboratory-scale tests or LES operating at even more realistic high-performance military aircraft conditions are needed to fully understand the spatiospectral characteristics of the F-35.

5.7 Acknowledgments

This research was supported in part by the Office of Naval Research through the Jet Noise Reduction Project. The authors also gratefully acknowledge funding for the F-35 measurements provided through the F-35 Joint Program Office and Air Force Research Laboratory. K. M. Leete was funded by an appointment to the Student Research Participation Program at the U.S. Air Force Research Laboratory, 711$^{\text{th}}$ Human Performance Wing, Human Effectiveness Directorate, Warfighter Interface Division, Battlespace Acoustics Branch administered by the Oak Ridge Institute for Science and Education through an interagency agreement between the U.S. Department of Energy and USAFRL. (Distribution A: Approved for public release; distribution unlimited. Cleared 09/27/2019 JSF19-903).

Chapter 6

Holography and Acoustic Intensity Analyses of the Simulated Jet

6.1 Introduction

Since the beginnings of jet noise research more than a half-century ago, an ongoing problem has been to understand the origin of the jet noise source. A variety of methods have played a role in experimentally deriving the locus of acoustic energy in jets over many years. Some of these include measurements using acoustical mirrors [99], ray-traced measurements of acoustical intensity [103, 137], phased arrays including near-field acoustical holography [79, 83, 138] and beamforming [65, 70, 72, 74, 75], and correlations between the measured flow and fields [13–15, 23, 86, 139]. Additionally, numerical simulations [126, 127] allow for entire flow field decomposition techniques [26, 27, 31, 32], linear stability analyses [29], and resolvent analysis [30, 33], which give insight into noise source mechanisms and source locations. Generally, for supersonic jets the noise can be separated into components such as broadband shock associated noise, screech, large-scale

turbulence structure noise, fine-scale turbulence structure noise, and Mach wave radiation. All these components have unique source localizations based on the operating conditions of the jet.

Parallel to the investigations of jet noise source phenomena, research done to understand the noise generated by rockets on liftoff have focused on semi-empirical methods. NASA SP-8072 [43] provides normalized spectra, estimates of axial distributions of overall sound power, and sound source position as a function of frequency, which were generated using laboratory-scale supersonic jet and full-scale rocket data [44, 45]. The document presents a method to apply these generalized spectra by scaling to the specific test at hand to create an equivalent source model of the jet noise, consisting of a distribution of sources along the jet centerline. The strength of these sources is related to the mechanical power of the jet through an assumed acoustic efficiency of about 0.5%. Since then, several studies focused on adapting these empirical relations so that they match more recent data as they became available [46–48], often tuning the definitions of characteristic lengths [49], as well as including the integration of computational schemes [50, 51] for generation and propagation of the sound field. Recent work [52] has shown that a plotting error propagated in the NASA SP-8072 document has led to an understanding in the rocket noise community that the main source of noise is the subsonic portion of the flow [46], while in the jet noise community it is understood that the main acoustic power originates between the potential and supersonic cores [45].

Of interest to this work is the recent measurement and analysis of high-performance military aircraft, which may provide a link between the supersonic jet noise research and rocket noise research. Inverse methods such as beamforming [75] and near-field acoustical holography [83, 138] have been successful in reconstructing the jet noise field over a large area from limited measurements. Wall et al. [83] applied multisource statistically optimized near-field acoustical holography (M-SONAH) to a scan-based, two-dimensional measurement hologram of a rectangular-nozzled aircraft and Leete [138] used the same method applied to a ground-based linear array to reconstruct the field of a round-nozzled aircraft. For both cases, they provide estimations of the acoustically relevant

source region by reconstructing the field along the nozzle lipline. The main locus of the energy along the lipline is found to decrease in width and shift upstream towards the nozzle as frequency is increased. Additionally, discrete lobes in the spatiospectral domain are present, reflective of the multiple spatiospectral lobes observed in the field of both those aircraft. These time-harmonic pressures along the nozzle lipline can be thought of as describing the aeroacoustic noise source pertinent to the near- and far-field radiation, because they contain all the information needed to reproduce the field. What is unknown, however, is whether these pressures are representative of actual measurements of acoustic variables along the nozzle lipline, because measurements of flow variables of these military aircraft are unavailable.

Advancements in numerical simulations of jets have allowed for increasingly accurate reproductions of the aeroacoustic flow field [126, 127] and now provide an opportunity to use inverse methods that are generally applied to laboratory and full-scale measurements to the simulated dataset [140]. The purpose of the current work is as follows: to sample the numerically generated acoustic field as if it were measured in a field test, apply statistically optimized near-field acoustical holography (SONAH), then evaluate the accuracy of the SONAH reconstructions against the simulations. The finely sampled pressure and particle velocity fields of the numerical simulation allow for calculations such as the vector intensity, and to test the ability of the holography technique to reproduce the pressure, particle velocity, and acoustic intensity in the field and within the plume. Using the acoustic intensity from the simulations and the holographic reconstructions, the overall sound power of the simulated jet, the acoustic efficiency, and the axial distribution of sound power are calculated.

6.2 Large Eddy Simulations

The LES dataset used in this work is provided by Liu et al. [39, 40, 91], which used the Jet Engine Noise Reduction (JENRE®) solver to calculate the heated flow passing through a conver-

gent/divergent nozzle. The JENRE® solver uses a monotonically-integrated LES approach with a flux-corrected transport algorithm [129] and explicit Taylor-Galerkin scheme. Tetrahedral meshes were used to implement the complicated nozzle geometry, which had a nozzle exit diameter, D, of 2.868", a design Mach number of 1.5 and fully expanded pressure ratio of 3.7. The thermodynamic quantities in the flow region were calculated out to a conical surface outside of the main flow, then the far-field pressures were predicted using the Ffowcs Williams and Hawkings (FW-H) integration method [130]. Cell sizes about $D/286$ are used near the nozzle that gradually increase to around $D/20$ near the FW-H integration surface (FWHS). Specifics of the choice of integration surface and grid resolutions can be found in Ref. [131].

The simulation was run at a nozzle pressure ratio of four and a temperature ratio of seven, resulting in an underexpanded, shock-containing jet with a temperature in the same regime as high-performance military aircraft operating at afterburner [132]. A method for calculating the temperature-dependent specific heat ratio was incorporated, which was found to match well with NIST databases for air under these conditions (see Fig. 2 of [39]). Time records of the LES simulation were split into 97 blocks and a Fourier transform applied to each block to give a complex pressure spectrum with a frequency spacing of about 150 Hz. The total temporal duration of the simulation was 0.326 s, which covers 5260 convective time units (D/U_j, the nozzle diameter divided by the fully expanded jet velocity).

The fluctuating component of pressure and particle velocity generated by the LES are sampled along three simulated arrays: along the jet centerline and the nozzle lipline, sampled from the nozzle exit to $x/D = 25$ in increments of $x/D = 0.2$ and along the FWHS on the line $y/D = \frac{1}{6}x/D + 1.5$ sampled from $x/D = 0$ to $x/D = 25$ in x/D increments of 0.1. The acoustic pressures generated from the FW-H integration are then sampled along three simulated arrays in the field. The first, which is the Hologram, is parallel to the FWHS and is described by the equation $y/D = \frac{1}{6}x/D + 10$, with x/D sampled in increments of 0.1 from $x/D = -10$ to $x/D = 40$. This array is expanded by

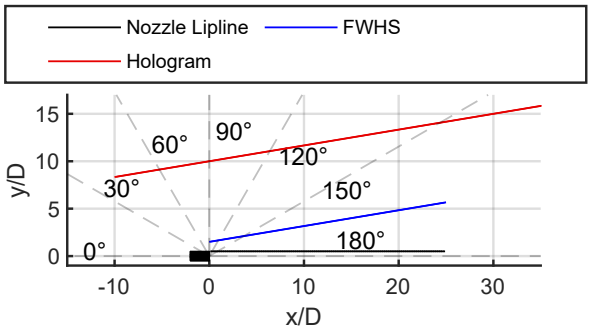

Figure 6.1 Sampled arrays in the near field: Jet lipline, FWHS, and Hologram. Dashed lines show the jet inlet angle (θ).

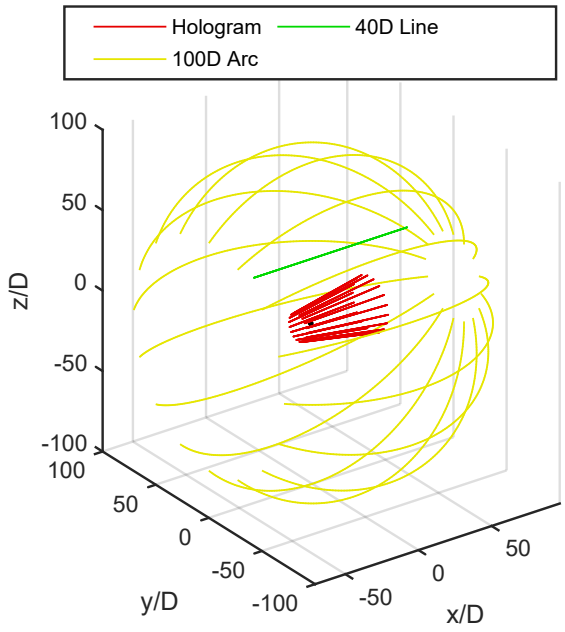

Figure 6.2 Additional sampled arrays, Hologram, 40D Line, and 100D Arc.

rotating it around the x-axis in 20° increments to make a set of 18 finely sampled lines. Another is a single line above the x-axis extending from $x/D = -40$ to $x/D = 65$ at $y = 0$ and $z/D = 40$ in steps of 0.1 diameters. The last is a far-field arc with radius of 100 D, spanning jet inlet angles (θ) of 45° to 165° in 1° increments, which is rotated about the x- axis in 22.5° increments to make a

surface covering the angular range of interest. Figure 6.1 contains a two-dimensional plot of the location of the nozzle, the sampled arrays along the lipline, FWHS, and Hologram, while Fig. 6.2 shows a three dimensional plot of the expanded Hologram, the 40D Line, and 100D Arc.

The local Mach number of the fluid along the jet centerline (solid) and the ratio of the axial fluid velocity, U, to the fully-expanded jet velocity, U_j (dashed) is plotted in Fig. 6.3. The end of the potential core (L_c) is estimated as $x/D = 7.2$, where $U/U_j \approx 0.95$ and is marked with a square. The end of the supersonic core (L_s) is located at $x/D = 12.7$, where $M = 1$ and is marked with a blue diamond.

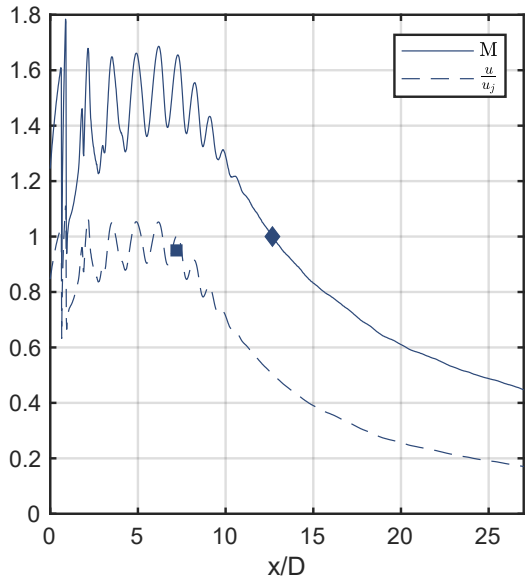

Figure 6.3 The Mach number (solid) and jet velocity ratio (dashed) along the jet centerline, with the locations of L_c (square) and L_s (diamond).

The frequency-dependent complex pressure (p) and particle velocities (u) shown in this work are the outputs of the discrete Fourier transform, scaled to give the correct single-sided power spectrum (in Pa^2) when the modulus squared is averaged over measurement blocks. Sound pressure levels

(SPL) are referenced to 20 μPa. The turbulence kinetic energy per unit mass (TKE) is one half times the sum of the power spectra of the three Cartesian components of the particle velocity.

$$\mathrm{TKE} = \frac{1}{2}(|u_x|^2 + |u_y|^2 + |u_z|^2), \tag{6.1}$$

and is displayed as a level referenced to 50 nm/s (the choice of reference for a sound velocity level) in this work.

6.3 Intensity and Power

The instantaneous acoustic intensity is the product of the pressure and particle velocity fluctuations at a given point in space. The time-averaged intensity (also called the active intensity) describes the net flow of energy carried by the propagating acoustic wave and can be calculated in the frequency domain [141] by

$$\vec{I}(f,\vec{r}) = \mathrm{Re}\{G_{p\vec{u}}(f,\vec{r})\}, \tag{6.2}$$

where $G_{p\vec{u}}(f,\vec{r})$ is the single-sided cross spectrum between the pressure and particle velocity. The sound intensity level (SIL) is referenced to 1 pW/m^2, so that it is identical to the SPL in the case of plane and spherical wave propagation.

The total sound power (W_a) of a source can be calculated by defining a closed surface, S, surrounding it and integrating the intensity flowing out of that surface,

$$W_a = \int_S \vec{I}(\vec{r}) \cdot d\vec{n}, \tag{6.3}$$

where $\vec{n}$ is the normal vector of the surface pointed outward. Computation of W_a is made simple when the integration surface is situated in the far field, such that the acoustic field can be approximated as locally planar. Then, for reasonably chosen surfaces the dot product in Eq. 6.3 reduces to

multiplication of the intensity magnitude with the corresponding area of the surface element, and the intensity vector magnitude is approximated by the autospectrum of the pressure ($G_{pp}(f,\vec{r})$),

$$|\vec{I}(f,\vec{r})| \approx \frac{G_{pp}(f,\vec{r})}{\rho_0 c}. \tag{6.4}$$

The single-sided autospectra of the pressures and particle velocities are estimated by averaging the magnitude of the Fourier transform over the 97 measurement blocks. The cross-spectra between the pressure and particle velocities are estimated by the block average of the product of the complex pressures with the conjugate of the complex velocity.

The acoustic efficiency (ε) of a jet is the ratio of radiated acoustic power, W_a, to the total mechanical power of the jet, W_m. The mechanical power is determined by the kinetic energy density ($\frac{1}{2}\rho U^2$) of the exhaust multiplied by the flow rate ($\pi(\frac{D}{2})^2 U$) at the nozzle exit. Since the axial velocity and the density change over the nozzle exit plane (especially because the underexpanded condition of the jet caused shocks in the nozzle), the average kinetic energy density is calculated over the exit plane from the average of the densities and axial velocities. The mechanical power is then calculated by

$$W_m = \left(\frac{1}{2}\rho_{\text{ave}} U_{\text{ave}}^2\right)\left(\pi\left(\frac{D}{2}\right)^2 U_{\text{ave}}\right), \tag{6.5}$$

and the subsequent acoustic efficiency

$$\varepsilon = \frac{W_a}{W_m} = \frac{8W_a}{\pi D^2 \rho_{\text{ave}} U_{\text{ave}}^3}. \tag{6.6}$$

The mechanical power thus calculated for this jet is $W_m = 736.9$ kW.

6.4 Holography Method

The holography method used in this work is called statistically optimized near-field acoustical holography (SONAH), which was developed by Steiner and Hald [93] to overcome limitations

of Fourier-based holography in requiring a measurement much larger than the size of the source. Section 6.4.1 discusses the basic formulation of the technique to estimate the pressures of a coherent field, Sec. 6.4.2 discusses how the formulation is altered to estimate the particle velocity fluctuations, and Sec. 6.4.3 discusses application to the partially-coherent jet noise field of the LES.

6.4.1 SONAH formulation

Statistically optimized near-field acoustical holography can be thought of as a two-step process: 1) an equivalent wave model (EWM) is fit to a hologram surface, h, and 2) evaluated at a reconstruction surface, q. The EWM used in this study is a set of m cylindrical basis functions, $\Psi(\vec{r})$, where

$$\Psi_{l,k_x}(\vec{r}) \equiv \frac{H_l^1(k_r r)}{H_l^1(k_r r_0)} e^{il\phi} e^{ik_x x}, r \geq r_0 \tag{6.7}$$

and r, ϕ, and x are the radial, azimuthal, and axial spatial components of $\vec{r}$. H_l^1 is the lth-order Hankel function of the first kind; i is the imaginary unit, r_0 is some small reference radius (traditionally the assumed source radius [96]), and k_x and k_r are the axial and radial wavenumbers, respectively. For this study, only $l = 0$ wavefunctions were used for consistency with previous work on military aircraft [83, 138]. The number of wavefunctions, m, is therefore only dependent on the number of k_x values used. The k_x values for this study were regularly spaced between $-\frac{\pi}{\mathrm{d}x}$ and $\frac{\pi}{\mathrm{d}x}$, in steps of $\frac{2\pi}{8\Delta x}$ with dx as the interelement spacing of the array in x and Δx is the total span of the array in x. This simulates an aperture eight times larger than what was measured, which was necessary to eliminate wraparound errors within the aperture investigated in this work. The radial wavenumbers are

$$k_r = \begin{cases} \sqrt{k^2 - k_x^2} & \text{for } |k| \geq |k_x|, \\ i\sqrt{k_x^2 - k^2} & \text{for } |k| < |k_x|, \end{cases} \tag{6.8}$$

where $k = \frac{\omega}{c}$ is the acoustic wavenumber, ω is the angular frequency, and c is the speed of sound. This choice for wave function and definition of k implies a time harmonicity of $e^{-i\omega t}$.

For a hologram measurement of n_h sample points, the EWM evaluated at that location is constructed into a matrix $\mathbf{A}$ where the ijth element of $\mathbf{A}$ is the ith wavefunction evaluated at the jth point

$$\mathbf{A}_{ij} = \Psi_{k_{xi}}(\vec{r}_j), \tag{6.9}$$

where the size of $\mathbf{A}$ is m by n_h. A similar matrix, $\boldsymbol{\alpha}$, is generated in the same way, but with the EWM evaluated at the reconstruction surface. This matrix then has the same number of rows as $\mathbf{A}$, but with columns equal to the number of points at which to reconstruct, n_q.

At this point, the SONAH process [93] calculates the column vector of pressures at q, $\mathbf{p}_q$, from the column vector of pressures on h, $\mathbf{p}_h$,

$$\mathbf{p}_q^{\mathrm{T}} = \mathbf{p}_h^{\mathrm{T}} \mathbf{R}_{\mathbf{A}^{\mathrm{H}}\mathbf{A}} \mathbf{A}^{\mathrm{H}} \boldsymbol{\alpha}, \tag{6.10}$$

where the superscript T is the transpose, H is the Hermitian transpose, and $\mathbf{R}_{\mathbf{A}^{\mathrm{H}}\mathbf{A}}$ is the regularized inverse of $\mathbf{A}^{\mathrm{H}}\mathbf{A}$. Regularization is performed using a modified Tikhonov filter with the generalized cross validation procedure for the selection of the regularization parameter as outlined in Ref. [97].

Since the matrix $\boldsymbol{\alpha}$ is simply the set of chosen wavefunctions evaluated at q, all the preceding multiplications in Eq. 6.10 can be combined to represent the transpose of the column vector of coefficients corresponding to those wavefunctions ($\mathbf{c}^{\mathrm{T}}$). Thus, Eq. 6.10 can be simplified to

$$\mathbf{p}_q^{\mathrm{T}} = \mathbf{c}^{\mathrm{T}} \boldsymbol{\alpha}. \tag{6.11}$$

6.4.2 Particle velocity

It is a straightforward procedure to use the EWM to reconstruct the three components of particle velocity in addition to the pressures at the desired location. Following the process outlined in [142],

the particle velocity of acoustic waves in a source-free medium is related to the pressure via Euler's equation for a linearized acoustic process,

$$\vec{u}(\vec{r}) = -\frac{i}{\omega\rho_0}\nabla p(\vec{r}), \tag{6.12}$$

for an e^{-iwt} time harmonic wave where ω and ρ_0 are the angular frequency of interest and the ambient density of the medium, respectively. Applying Eq. 6.12 to Eq. 6.10, the matrix of velocity vectors at the reconstruction surface, $\vec{\mathbf{u}}_q$ is calculated by

$$\vec{\mathbf{u}}_q^{\mathrm{T}} = \mathbf{p}_h^{\mathrm{T}}\mathbf{R}_{\mathbf{A}^{\mathrm{H}}\mathbf{A}}\mathbf{A}^{\mathrm{H}}(\frac{-i}{\omega\rho_0})\nabla\boldsymbol{\alpha}, \tag{6.13}$$

since the $\boldsymbol{\alpha}$ matrix is the only variable that depends on the reconstruction location where the gradient is taken. The gradient of the $\boldsymbol{\alpha}$ matrix is constructed by evaluating the gradient of the pressure wavefunctions at each reconstruction location. The analytic solutions for the three components of the gradient in cylindrical coordinates are

$$\nabla_r\Psi_{l,k_x}(\vec{r}) = \frac{\frac{l}{r}H_l^1(k_r r) - k_r H_{l+1}^1(k_r r)}{H_l^1(k_r r_0)}e^{il\phi}e^{ik_x x}, \tag{6.14}$$

$$\nabla_\phi\Psi_{l,k_x}(\vec{r}) = \frac{il}{r}\Psi_{l,k_x}(\vec{r}), \tag{6.15}$$

and

$$\nabla_x\Psi_{l,k_x}(\vec{r}) = ik_x\Psi_{l,k_x}(\vec{r}). \tag{6.16}$$

It is convenient to define new matrices corresponding to each velocity component,

$$\boldsymbol{\alpha}_r = \frac{-i}{\omega\rho_0}\nabla_r\boldsymbol{\alpha}, \tag{6.17}$$

$$\boldsymbol{\alpha}_\phi = \frac{-i}{\omega\rho_0}\nabla_\phi\boldsymbol{\alpha}, \tag{6.18}$$

and

$$\boldsymbol{\alpha}_x = \frac{-i}{\omega\rho_0}\nabla_x\boldsymbol{\alpha} \tag{6.19}$$

so that Eq. 6.13 simplifies to the same form of Eq. 6.11 for each component of $\vec{\mathbf{u}}_q$:

$$\mathbf{u}_{rq} = \mathbf{c}^{\mathrm{T}} \boldsymbol{\alpha}_r, \tag{6.20}$$

$$\mathbf{u}_{\phi q} = \mathbf{c}^{\mathrm{T}} \boldsymbol{\alpha}_\phi, \tag{6.21}$$

and

$$\mathbf{u}_{xq} = \mathbf{c}^{\mathrm{T}} \boldsymbol{\alpha}_x. \tag{6.22}$$

Note that for the axisymmetric assumption ($l = 0$) made in this work, the ϕ component of the gradient in Eq. 6.15, and the subsequent $\mathbf{u}_{\phi q}$ in Eq. 6.21, are identically zero for any choice of q.

6.4.3 Application to LES

A fundamental assumption of SONAH is that the field at each frequency is a solution to the homogeneous Helmholtz equation, meaning that the field is coherent and contains no acoustic sources in the region between the hologram and the reconstruction location. It is well known that the jet noise field is not self-coherent, so care must be taken to extract self-coherent partial fields, apply the holography process to each partial field individually, then sum the partial fields together at the reconstruction location to arrive at a final answer. The partial field extraction is accomplished through spectral proper orthogonal decomposition [143]. A data matrix is constructed where the ijth element is the complex pressure measured for the jth block at the ith measurement point along the array, then this matrix is multiplied by its Hermitian transpose to generate the cross spectral matrix (CSM) of the array. The singular value decomposition of the CSM is then used to obtain the partial fields, which are simply each singular vector scaled by the square root of its corresponding singular value.

For the current experiment, each simulated array in use contains many more elements than there are measurement blocks, so the rank of the CSM (and therefore the number of physically

meaningful partial fields) is limited to the number of blocks, which is 97. Each of the 97 partial fields has a unique shape, though a common trend of these decompositions is that the partial field shapes are reminiscent of modes on a string, where the first has a single antinode at the point of maximum SPL, the second has two antinodes to the sides of the maximum, the third has three straddling the two from the second field, and so on. This causes the higher-order partial fields to have large amplitudes at the edges of the array relative to their peak.

To minimize wavenumber leakage caused by abrupt changes at the edges of the array, each partial field is extended two acoustic wavelengths in both directions using analytic continuation [144], then windowed with a Tukey window to enforce a graceful taper to zero. For this paper, the vectors $\mathbf{p}_h$ and $\mathbf{p}_q$ used in equation 6.10 are populated by the complex pressures at a particular partial field after this extension has been applied.

The bulk of the computation time at each frequency is spent in the regularization and inversion of the matrix $\mathbf{A}^{\mathrm{H}}\mathbf{A}$, whose size is n_h by n_h. To reduce the size, the hologram can be resampled so that the interelement spacing is larger, as long as spatial aliasing is avoided at that frequency. For this experiment, the array was decimated to an interelement spacing so that there were three points per wavelength, with a minimum of 97 elements to preserve the rank of the CSM.

Azimuthal considerations

Previous work investigating the field produced by military aircraft [83,138] has shown that imposing an azimuthal assumption by only including the zeroth-order Hankel functions in the EWM still allows for accurate reconstructions of the level of the sound field over the azimuthal aperture of the corresponding measurements. The axisymmetric EWM used in SONAH reconstructions, however, do not accurately represesent the coherence properties in the azimuthal direction. Leete et al. [145] measured the coherence angle (the angle over which the the coherence between two points reliably stayed over 0.5) and compared to predictions based on M-SONAH reconstructions.

The axisymmetric wavefunctions in the EWM predict unit coherence in the azimuthal direction, (a coherence angle of 360 degrees) while the measured values remained at least as large as 20 degrees below 400 Hz (two times the peak frequency of that jet).

For laboratory-scale jets, the acoustic field from jets with circular nozzles have been found to be axisymmetric in level [146]. For the circular nozzle of this simulation then, the most important consideration for accurate holographic reconstructions of the field would be the ability to replicate the coherence properties in the azimuthal direction. Though not displayed here, preliminary investigation of the coherence angles were found to be on the order of those found in the military aircraft field in Ref. [145]. Therefore, holographic reconstructions in this study using the axisymmetric EWM are expected to be accurate in level, though only faithfully reproduce coherence properties within a finite, frequency-dependant azimuthal range of the hologram. Additional investigation of the azimuthal limitations of the axisymmetric EWM is needed.

6.5 Results

This section discusses the similarity of the holographic reconstruction of the pressure, particle velocity, and acoustic intensity to the LES.

6.5.1 EWM fit

The Hologram array was designed to be large enough to cover the pertinent energy that radiates to the field, densely sampled to eliminate spatial aliasing, and emulate the locations of measurements near high-performance military aircraft [89, 138]. To test the ability of the EWM to fit the simulated data, the holography procedure is completed where the reconstructed location is at the Hologram itself, being the theoretical best-case scenario for the field to be accurately reconstructed.

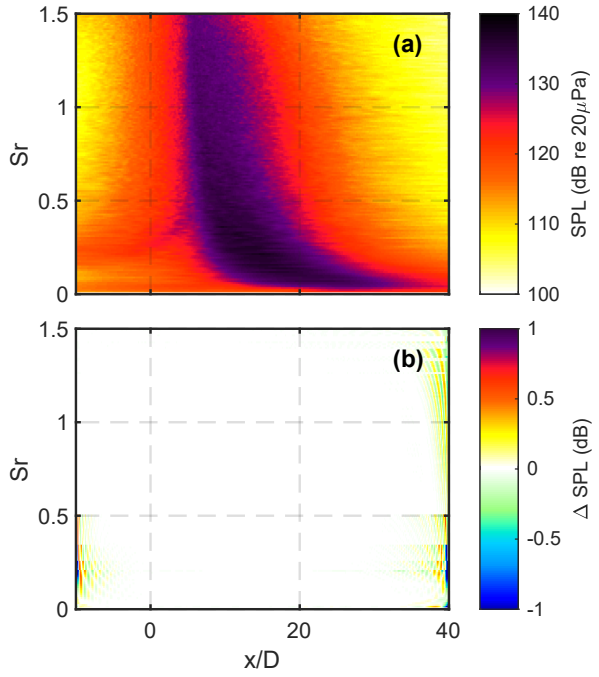

Figure 6.4 (a) Sound Pressure level along the Hologram and (b) error of the reconstructions as a function of distance from the nozzle in diameters and Strouhal number.

Figure 6.4(a) shows the spectra along the Hologram (red line in Fig. 6.1) as a function of normalized downstream distance, the color representing the narrowband SPL. The frequencies are expressed in terms of Strouhal number, which for this work is calculated as $Sr = fD/U_{\text{ave}}$. Figure 6.4(b) shows the difference between the reconstructed level and the level from part (a). Reconstruction errors are essentially zero over the frequency band and spatial aperture of interest, except at edge points, where error can creep up to 1 dB. This shows that the chosen EWM is able to fit the simulations well along the array and the regularization process is not too aggressive. This EWM is now used to reconstruct the pressure and velocity fields at location other than the Hologram.

6.5.2 Far-field Reconstructions

Sound pressure level and reconstruction accuracy at the 100D Arc in the far field (yellow lines in Fig. 6.2) are displayed in Fig. 6.5, displaying the SPL as a function of Sr and the angle from the $-x$ axis to each position along the arc (θ). Less than 1 dB error for the majority of the spatiospectral domain is observed, except at Sr < 0.06 and aft of 155°. Underestimation in the far aft is due to windowing of the pressures outside of the hologram to zero as discussed in Sec. 6.4.3.

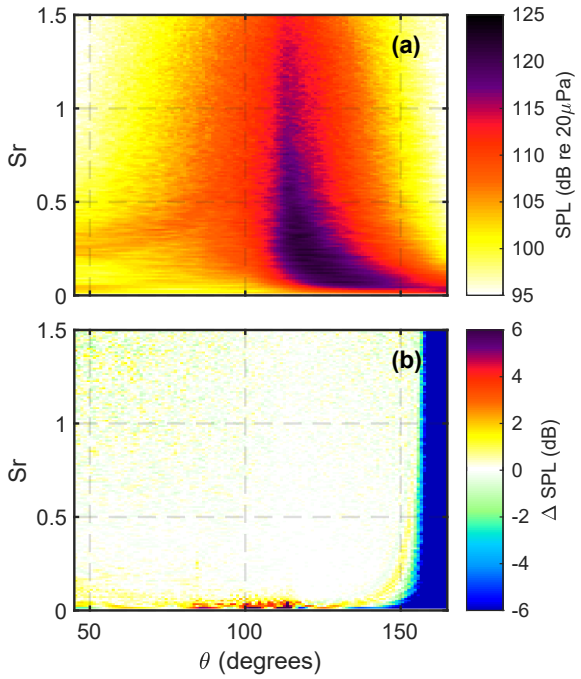

Figure 6.5 (a) Pressures along the far-field arc and (b) error in the reconstruction as a function of jet inlet angle (θ) and Strouhal number.

6.5.3 FWHS Reconstructions

Reconstructing the field inside the hologram at the FWHS, Fig. 6.6 shows the pressures generated by the LES in part (a) and reconstruction errors in part (b) in the same format as Figs. 6.4. The

reconstructions are accurate to within 2 dB error in most of the frequency and spatial range shown, though with large errors at the lowest frequencies and near the nozzle exit. Overestimations of the field by about 6 dB are found at Sr > 1 for $x/D > L_s$.

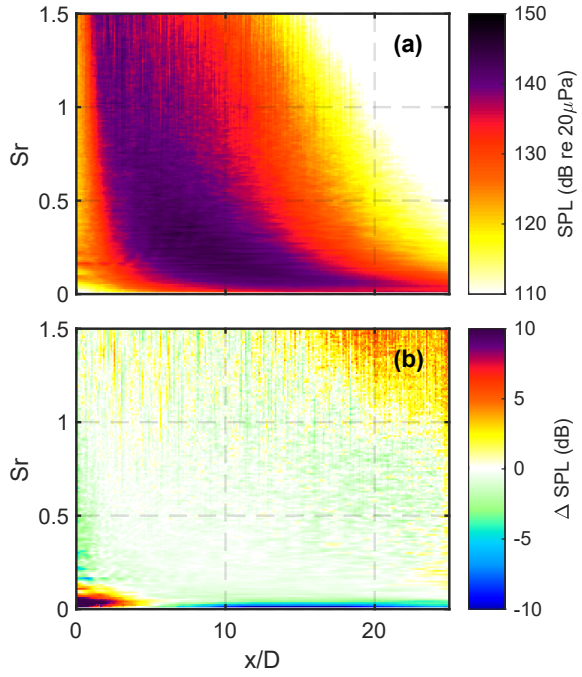

Figure 6.6 (a) Pressures along the FWHS and (b) error in the reconstruction as a function of distance from the nozzle in diameters and Strouhal number.

The LES-generated data contain velocities as well as pressures along the FWHS, so the TKE reconstructed at the FWHS array is compared to the simulation in Fig. 6.7. Errors are similar to those of Fig. 6.6, though with slightly larger amplitudes and the addition of large underestimations of the field far downstream. These underestimations in the far aft region indicate that the Hologram was not quite large enough to fully capture the aperture necessary to reconstruct the energy over this sampled array.

The SIL calculated along the FWHS array are displayed in Fig. 6.8. The similarity of the SIL and SPLs of the LES over most of the spectrum indicates that nearly plane-wave propagation is

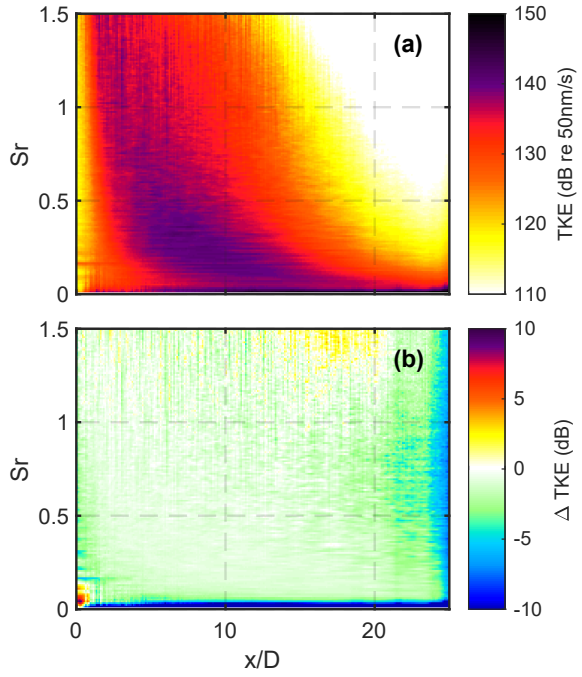

Figure 6.7 (a) TKE along the FWHS and (b) error in the reconstruction as a function of distance from the nozzle in diameters and Strouhal number.

present. Generally, the SPL, TKE, and SIL are overestimated by NAH in areas where amplitudes are low: by the nozzle exit at low frequency and far aft at high frequency. Low-frequency levels are underestimated downstream of the nozzle, and the TKE is underestimated at the far aft edge of the array at all frequencies. Since the pressures along the FWHS are the output from the LES, it is unclear if the error in the reconstruction at low frequencies is due to the holography process or if this low-frequency information was not transferred to the Hologram from the FWHS in the FW-H integration step. As the errors are low at the Hologram in Fig. 6.4, the latter is suspected to be the case, indicating that the low-frequency energy along the FWHS is hydrodynamic in nature.

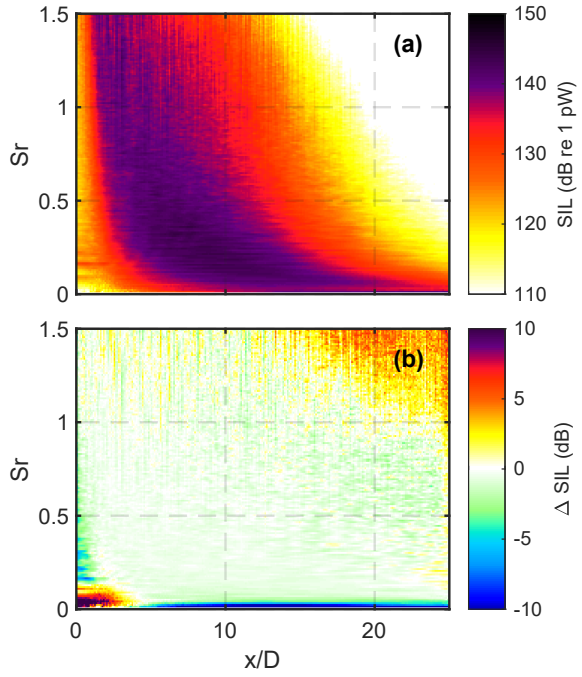

Figure 6.8 (a) Intensity magnitude along the FWHS and (b) error in the reconstruction as a function of distance from the nozzle in diameters and Strouhal number.

6.5.4 Lipline Reconstructions

Reconstructions along the nozzle lipline (black line in Fig. 6.1) are undertaken to test the application of holography within the jet plume. Figure 6.9 a) shows the LES-generated pressures sampled along the nozzle lipline, Fig. 6.10 a) shows the TKE, and Fig. 6.11 a) the acoustic intensity. Unlike previous figures, these show the reconstructions in part (b) and the errors of the reconstructions in part (c) to demonstrate the differences in spectral shape of the reconstructions from the benchmark. To separate errors in the level of the spectra from misrepresentations of the shape of the spectra, the color map in part (c) of each figure is chosen such that white, instead of representing zero error, now represents an offset in the error, calculated as the mean error in the region 3 dB down from the maximum level.

The pressure reconstructions in Fig. 6.9 b) follow the relative shape of the spectra well, though with a general underestimation of the energy by about 4 dB. After adjustment for this offset, errors in the main lobe are within about 2 dB. Large errors occur outside of this main locus of energy, however, which are truncated by the range of the color bar so details in the main radiation region can be seen. The TKE reconstructions in part (b) of Fig. 6.10 show a spectral shape similar to the pressure reconstructions, while the data in part (a) of Fig. 6.10 peak at lower frequencies than the pressure and have a steeper roll-off at high frequency. In part (c), the TKE reconstructions are shown to underestimate the flow by 26 dB, which is set to white. The deviations from the -26 dB offset are from the misrepresentation of the spectral shape, overestimation of the field near the nozzle exit (the LES fluctuations go to zero at the nozzle exit, but the holographic reconstructions do not), and severe underestimations of the field at low frequencies and aft of the main radiation lobe.

The holographic reconstruction of the pressure and velocity is not expected to match the actual LES-generated data. The EWM used in the holography method represents waves emanating from a small cylindrical surface which contains all the pertinent sources; the only situation in which the pressures along the nozzle lipline would match the reconstructions is if all the acoustic sources were located within a similar cylinder whose surface is on the lipline. Additionally, the velocity and pressure fluctuations generated by the LES are not correlated with the sound radiated to the far-field hologram, from which the EWM is derived. An ongoing research problem is to identify the components of the pressures and velocities which do correspond to the far-field acoustics, such as the application of Doak's momentum potential theory [28] or other flow field decompositions [26].

The quantitative agreement of reconstructions of the SIL along the nozzle lipline in Fig. 6.11 suggest that the holography technique is representing the acoustically relevant component of the pressure and particle velocity fluctuations in the flow. However, the axisymmetric nature of the EWM used forces the vector intensity to be pointed radially outward from the jet centerline, while

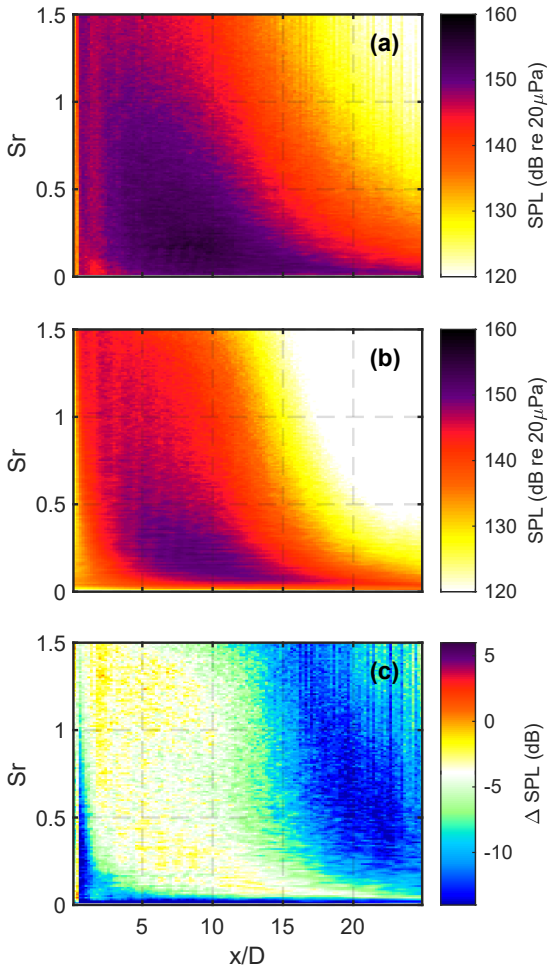

Figure 6.9 (a) LES Pressures, (b) reconstructed pressures, and (c) error in the reconstruction along the nozzle lipline as a function of distance from the nozzle in diameters and Strouhal number. The color bar is centered at an offset of -4 dB.

the directions of the calculated intensity vectors (not shown here) are pointed in seemingly random directions at this sampled array. Since jet noise sources are usually thought of as a volumetric distribution throughout the plume, it is likely that the holographic reconstructions would more closely resemble an integration of the sources over the volume within the cylinder of the nozzle lipline. This line of comparison is recommended for future work. The fact that the reconstructed

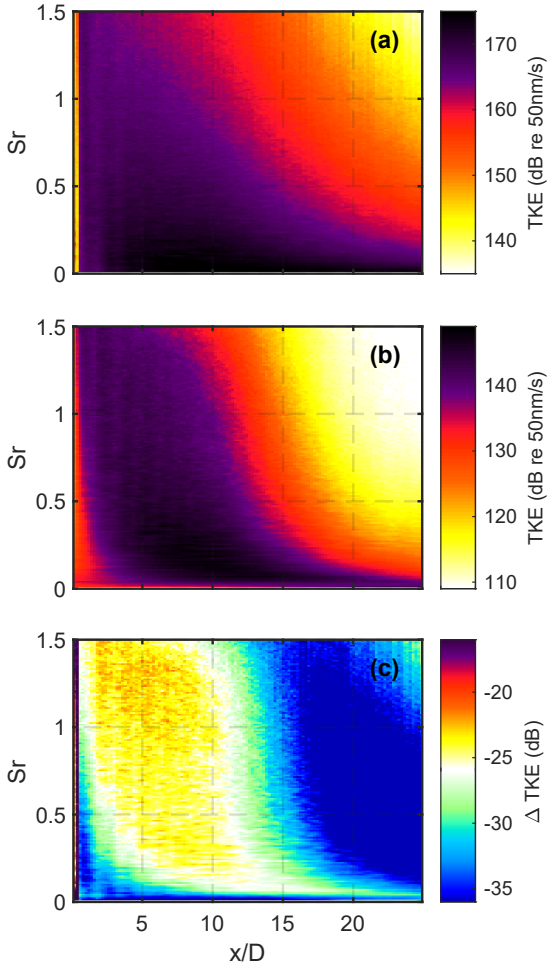

Figure 6.10 (a) LES TKE, (b) reconstructed TKE, and (c) error in the reconstruction as a function of distance from the nozzle in diameters and Strouhal number. The color bar is centered at an offset of -26 dB.

acoustic intensity matches the acoustic intensity magnitude at all is heartening, suggesting that the simple calculation of Eq. 6.2 can be applied to LES or measured data of laboratory jets in the future to investigate its ability to isolate the acoustically-relevant components of the jet flow.

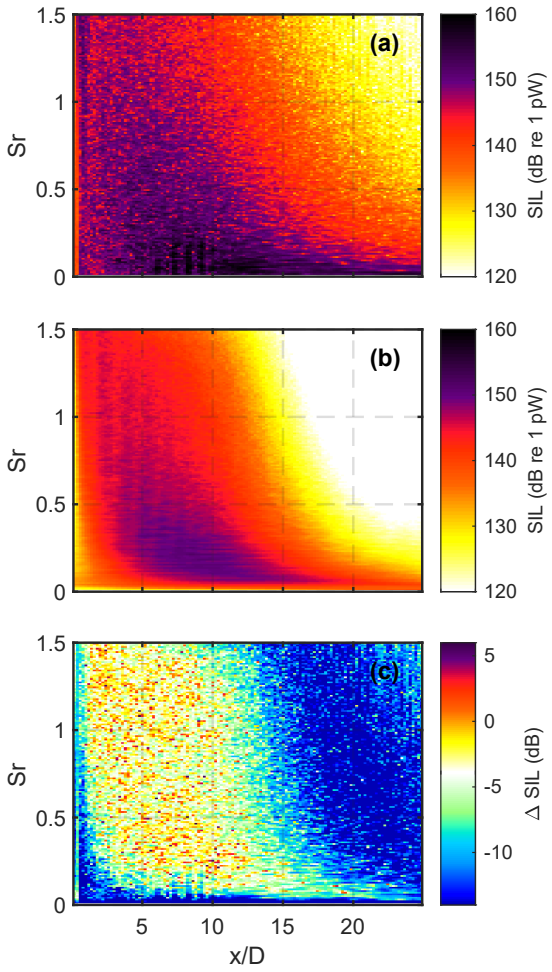

Figure 6.11 (a) LES intensity magnitude, (b) reconstructed intensity magnitude, and (c) error in the reconstruction on the nozzle lipline as a function of distance from the nozzle in diameters and Strouhal number. The color bar is centered at an offset of -4 dB.

6.6 Analysis

Prior works have used pressure fluctuations along the nozzle lipline as a representation of an equivalent acoustic source distribution which represents the field [36, 138]. From Figs. 6.9 and 6.11 it appears that holographic reconstructions at the lipline of the are a fair representation of the shape

of the LES-generated pressures and acoustic intensities. The open question, then, is whether these distributions are accurate representation of the actual locus of acoustic source power.

To characterize the acoustic power of the jet, Eq. 6.3 is applied along the FWHS from the LES directly and at other near and far field surfaces using the holographic reconstructions of the vector intensity. Axial distributions of sound power are also developed by raytracing the intensity vectors to the jet centerline.

6.6.1 Sound Power

Calculations of W_a can be achieved with direct application of Eq. 6.3 if the dataset in question has both pressure and particle velocity sampled in sufficient density on a surface surrounding the jet. For each of the sampled arrays mentioned in Section 6.2, the calculation of overall sound power level is completed using the LES data directly where both pressure and particle velocities are available and from the holographic reconstructions elsewhere. The process is then repeated using Eq. 6.4 to estimate the intensity magnitude and assuming the vector is perpendicular to the sampled surface. Table 6.1 shows the overall sound power level calculated in each of these situations, with the left column denoting the array used to calculate the sound power and the four remaining columns whether the LES data or holographic reconstructions were used along with the method of calculating the vector intensity.

For the extended Hologram and 100D Arcs where there is azimuthal information, the calculation is done twice, once using a single array which is rotated around the x-axis, and once with the full array. The addition of more azimuthal coverage changed the calculation of the overall sound power level by less than 0.01 dB, confirming the axisymmetry of the levels of the jet noise in this simulation.

The only significant deviation in sound power calculation is noticed when the autospectrum of the pressures is used to estimate the vector intensity magnitude along the FWHS, which overestimates

Table 6.1 Overall sound power level (dB re 1 pW) calculated from various arrays.

	LES		Holography	
	$\mathrm{Re}\{G_{pu}\}$	$G_{pp}/(\rho_0 c)$	$\mathrm{Re}\{G_{pu}\}$	$G_{pp}/(\rho_0 c)$
FWHS	160.6	161.8	159.2	161.4
Hologram	-	160.5	160.3	161.5
40D Line	-	160.4	160.2	161.0
100D Arc	-	160.5	160.2	160.5
EWM source	-	-	160.3	161.8

the overall sound power. The overestimation is a combination of two phenomena: 1) using G_{pp} instead of G_{pu} to calculate the acoustic intensity does not filter out the low-frequency hydrodynamic components which do not propagate to the far field and 2) the actual intensity vectors are not perpendicular to the surface represented by the array. In the far-field, however, deviations are remarkably small, signifying that the overall sound power level is a relatively forgiving calculation.

To view the spectral distribution of sound power, the sound power spectral density in Watts per Strouhal number (W/Sr) are displayed as a level referenced to 1 pW in Fig. 6.12. Each line represents the calculation using the pressures and particle velocities of the holographic reconstructions, except for the red line, which uses the LES data directly. The only significant difference between these curves are that all the holography-based calculations slightly underestimate the calculations direct from the LES, while using the assumptions of Eq. 6.4 on the FWHS overestimates the levels.

The sound power calculated for this simulated jet (corresponding to the level of 160.6 dB reported in table 6.1) is 11.5 kW, which results in an acoustic efficiency (η) calculation of 1.56 %. This percentage is larger than is recommended by NASA SP-8072, which uses 1% as a conservative upper bound. It is possible that η of this jet is augmented due to its underexpanded nature, where shocks within the nozzle cause a reduction in mechanical power calculated at the nozzle exit.

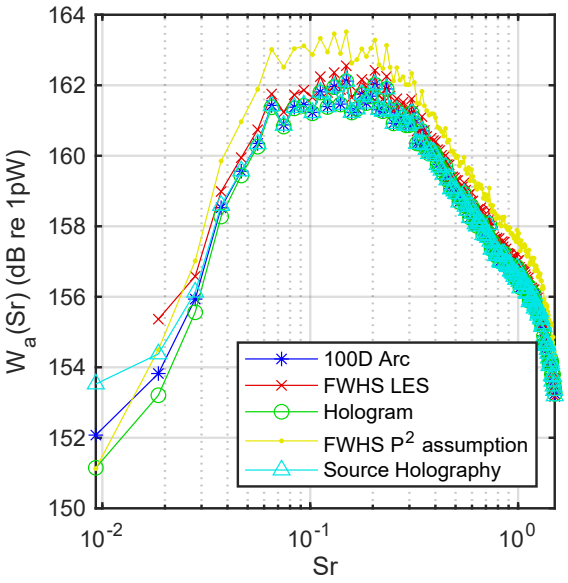

Figure 6.12 Sound power spectral density (W/Sr) level (dB re 1 pW) calculated by integration over various surfaces.

6.6.2 Axial Distribution of Sound Power

Sound power calculations for the entire jet are helpful in describing its overall acoustical efficiency, though information about the origin of this noise can lend insight into noise generation mechanisms within the plume. Equation 6.3 is interpreted as calculating the energy flux through an enclosing surface, which, in practice, is discretized into a finite number of patches, each represented by a measurement point. Therefore, the dot product of the intensity vector with the normal vector of each patch is the power contribution from that patch. The origin of this small portion of the overall power can be found by raytracing the intensity vector at that patch back to the jet centerline. Figure 6.13 shows a schematic of this process on the FWHS superimposed on a snapshot of the pressure fluctuations calculated by the LES. The red arrow represents the the calculated intensity vector at a particular sampled location and the black arrow the normal vector to the surface, with the insert showing a zoomed in version of the point in question. The red dashed lines represents the

calculation of the source location for this particular patch's worth of power. The dotted black line represents the assumption of the source location if the intensity vector is not actually known and its vector magnitude needs to be estimated using Eq. 6.4. The red and black dashed lines would be identical if the integration surface was chosen to be parallel to the acoustic wavefronts.

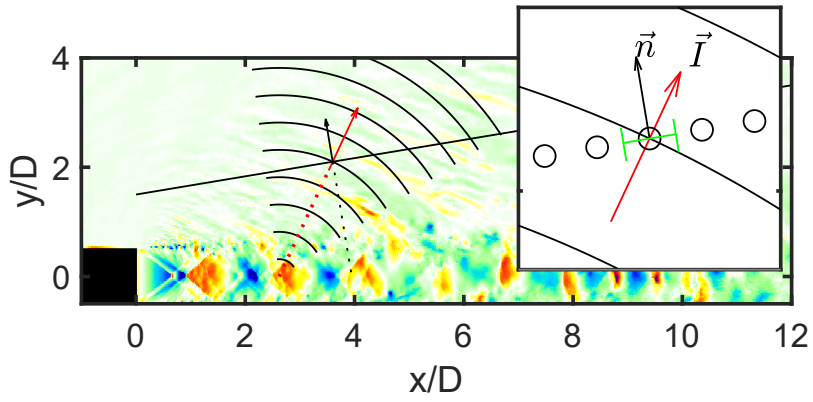

Figure 6.13 Schematic of raytracing procedure overlayed on a snapshot of the instantaneous pressures generated by the LES.

When this raytracing is completed for all the patches over the enclosing surface S, it results in a list of origins for all the individual patches with their contributing power values. These can be binned into a histogram to create a distribution of the source sound power along the jet centerline, so that integration of the distribution results in the total sound power. Figure 6.14 shows the results of this raytracing for holographic reconstructions of the vector intensity along the 100D Arc, the Hologram, the direct computation of the vector intensity along the FWHS from the LES, and repeated using just the squared pressures along the FWHS.

An additional method of determining the source sound power is calculated and added as the cyan line in Figs. 6.12 and 6.14 and as the last row of Table 6.1. The EWM used in Eq. 6.7 is equivalent to a radially vibrating cylinder of radius r_0 located along the jet centerline, with arbitrary

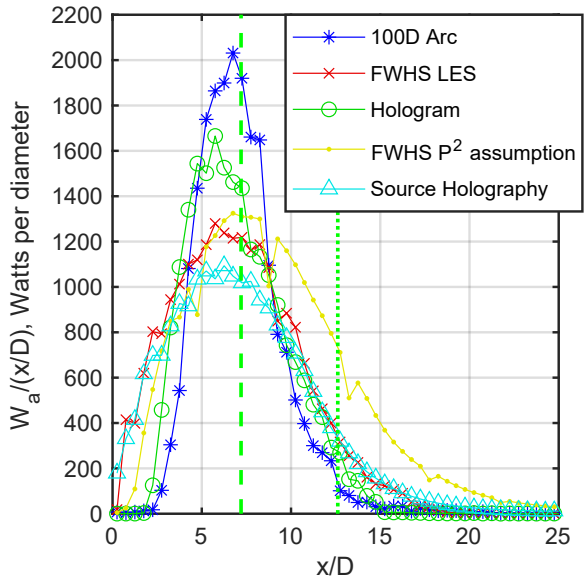

Figure 6.14 Sound power per diameter along the jet centerline, raytraced from various field arrays and calculated from SONAH reconstructions on a cylinder of radius r_0 (cyan). The dashed and dotted lines represent L_c and L_s, respectively.

axial phase relationship. Reconstructing the vector intensity field at r_0 can then directly compute the sound power generated by this cylinder as a function of x. This results in an approximation of the axial distribution of source power along the jet centerline because the radius is very small (0.5 mm in this case).

To look at ray-traced source distributions as a function of frequency, Fig. 6.15 shows the sound power spectral density level traced back to each $\frac{1}{2}D$ bin along the jet centerline from (a) the LES on the FWHS and (b) the holographic reconstructions to the 100D Arc. The green dashed and dotted lines on Figs. 6.14 and 6.15 represent L_c and L_s, respectively.

Both Figs. 6.14 and 6.15 show a trend in the localization of the sound power depending on the placement of the array. The calculation of the axial source distribution from the FWHS and the cylinder of the EWM are broad, and the rise on the upstream side match the linear rise in sound power observed in Ref. [45]. Though the far-field estimations integrate to the same overall sound

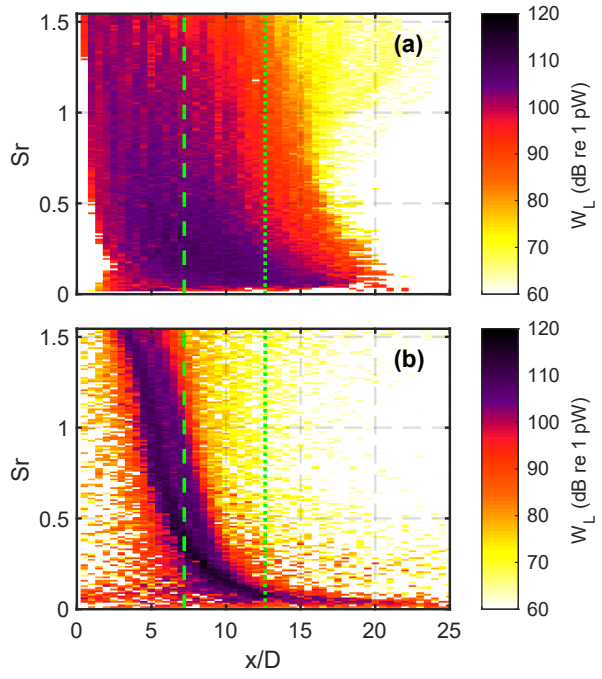

Figure 6.15 Sound power spectral density (W/Sr) level (dB re 1 pW). For the power traced back to $\frac{1}{2}D$ bins along the jet centerline, the dashed and dotted lines represent L_c and L_s, respectively.

power level as those derived from the FWHS, they concentrate the energy into a more compact source that is highly frequency dependent. This result suggests that if the correlated nature of the source is not incorporated in the equivalent source model (e.g., the distributed uncorrelated monopole source suggested by NASA SP-8072), then different source distributions would need to be used depending on whether the source model is used to represent the near field or the far field.

Differences in source power localization may change the interpretation of which region of the jet is contributing most to the acoustic power [52]. Table 6.2 shows the percent of W_a that originates from the potential core ($x < L_c$), between the potential and supersonic cores ($L_c < x < L_s$), and the subsonic portion of the flow ($L_s < x$). Even with the differences between the distribution calculated from the 100D Arc and the FWHS, the physical interpretation remains the same, with the vast majority of the power split between the potential core region and the region between L_c and L_s.

If, however, the direction of the intensity vectors are estimated as perpendicular to the integration surface, the amount of power localized to the subsonic portion of the flow is doubled. In conjunction with the results of Chapter 5, this suggests that one would overestimate the contribution to the field from the large-scale turbulent structure noise generated in the region around L_s and underestimate the contribution from the Mach wave radiation.

Table 6.2 Percent of W_a originating from upstream, between, and downstream of the potential (L_c) and supersonic (L_s) cores

	$x < L_c$	$L_c < x < L_s$	$L_s < x$
100D Arc	52 %	45 %	3 %
Hologram	54 %	42 %	4 %
FWHS G_{pu}	53 %	40 %	7 %
FWHS G_{pp}	37 %	43 %	20 %
Source Holography	51 %	39 %	10 %

6.7 Conclusions and Recommendations

Statistically optimized near-field acoustical holography has successfully reconstructed the noise produced by a LES of a highly heated laboratory-scale jet. The pressure reconstructions match the near and far fields with minimal error in the measurement aperture but underestimate the pressure fluctuations along the nozzle lipline by 4 dB. The particle velocity and vector intensity reconstructions match the LES at the FWHS, and though reconstructions inside the plume at the nozzle lipline severely underestimate the velocity fluctuations, the vector intensity magnitudes are only underestimated by the same factor as the pressure reconstructions. The fact that the pressure and intensity fluctuations underestimate the LES-generated values by the same amount suggest that the correct phase relationship between the pressure and particle velocity are maintained and the

holography process is extracting acoustically relevant pressures and particle velocity components of the flow.

Acoustic intensity reconstructions in the field allow for predictions of the sound power level of the jet. With knowledge of the mechanical power of the simulation, an acoustic efficiency of 1.56% is calculated. The axisymmetric nature of the jet in level allows for axisymmetric assumptions in the calculation of the sound power. Further simplification of the the sound power calculation by using the squared pressure instead of the full pressure and particle velocity calculations are suitable, even in the geometric near-field (with overestimations of the overall level of as little as 1 dB). However, using the squared pressures in the near field does not accurately localize the source distribution of sound power, shifting it a few diameters aft in this case. The calculation of acoustic efficiency is more sensitive than the calculation of sound power level. For example, an increase of sound power level by 1 dB increases the calculated acoustic efficiency to about 1.9%.

This calculation of the acoustic efficiency of a jet could be easily applied to any simulated jet database that includes the density and velocity at the nozzle exit and the pressure and particle velocities along a Rayleigh or FW-H type surface. If axisymmetry is assumed, a single sampled line can be used as well. Using a simple tool such as the acoustic efficiency of the jet may be valuable for evaluation of noise reduction technologies to isolate whether the noise reduction is due to a fundamental change in radiation characteristics, or if simply the thrust of the jet is being controlled to reduce the radiated noise. Though the acoustical efficiency calculated for this particular jet is larger than that assumed of rockets, the data point provided by this jet is a single one over a large domain. It would be to the benefit of the rocket and jet noise communities to report their calculations of acoustic efficiency so more robust investigation of this space can be accomplished.

Raytracing the vector intensity back to the jet centerline, the axial power per unit length is derived, which shows most of the energy originating from upstream of L_c, similar to experiments of other heated laboratory scale jets [147]. The strong Mach waves generated by the supersonic

portion of the jet are likely the reason, as they dominate in this region [92]. The sound power source distributions depend on whether the vector intensity is calculated in the near or far field, with the apparent source distribution becoming more compact and peaked when tracing from the far-field. The theory of Nagamatsu and Horvay [45] for a linear increase in sound power from the nozzle exit to the peak of the power distribution matches well for the distributions derived in the near field. Estimations of the axial distribution of sound power by use of the squared pressures is not encouraged, as it will shift the apparent jet noise source downstream.

Estimations of the source sound power can also be directly calculated from the holography process, by reconstructing the pressures and particle velocities to the small reference radius of the EWM. This calculates an equivalent vibrating cylinder that reproduces the jet noise field, and whose sound power closely resembles the intensity raytracing of the LES generated intensity vectors. The frequency-dependent source power of part (a) of Fig. 6.15 is similar in shape to the pressure and intensity reconstructions along the nozzle lipline of Figs. 6.9 and 6.11, suggesting that the pressure disturbances in the flow are more closely correlated to the far-field acoustics than the velocity fluctuations [148]. This striking similarity between the shape of the source power and the pressure reconstructions along the lipline suggest that they may be interchangeable. More direct investigations within the flow pressures, perhaps as a function of radius, could be employed to investigate further. Holography is found to be a robust tool in calculating frequency-dependent source sound powers for jet noise, with estimations of the axial distribution of source power mirroring those calculated directly from the LES. Past successful implementations at the laboratory and full scales to reconstruct the acoustic field [79, 84, 138] suggests that holography can be a viable alternative to calculating axial distributions of sound power if direct measurements using acoustic intensity probes or other methods are unfeasible.

Chapter 7

Conclusions

This compilation of investigations has provided important insight into the fields generated by high-performance military aircraft and a simulated highly heated laboratory-scale jet. Comparisons between the two illuminate aspects of the jet noise field that are still not understood and accounted for in modelling efforts. Validation of holography on the LES dataset provides encouraging results that holography may be a valid method of extracting the acoustically relevant pressure and velocity perturbations in the flow, as well as a practical tool for calculation of sound power distributions of military aircraft or other high-velocity flows. These conclusions lead to an enhanced understanding of the jet noise source of high-temperature and high-velocity jets.

7.1 Military Aircraft Field

It has become increasingly clear that the sound field produced by military aircraft does not match the previously established two-source model [8]. Both the F-35 and T-7A aircraft discussed here contain multiple peaks in the aft spectra, which, as seen in Figs. 2.3, 2.7, and 4.4, are better characterized as spatiospectral lobes. Dense measurements of the near field show upwards of five spatiospectral lobes present in the F-35 and potentially more in the T-7A. The lobes are slanted, with the peak

frequency increasing with downstream distance, consistent with the observation that the spatial directivity of the lobes shift aft with increasing frequency.

The measurement of multiple engine powers shows that the shift in directivity towards the sideline is mainly driven by the increase in the number of lobes and the larger relative amplitudes of the upstream lobes compared to the downstream ones. This is most clearly seen in the jump between intermediate conditions; between 50% ETR and 75% ETR for the F-35 and between 83% N2 and 88% N2 for the T-7A. Additionally, each lobe becomes more spatially compact with increase in engine power, with a smaller deviation in spatial directivity as frequency is increased, exemplified by the difference in the top and bottom plots in the rightmost columns of Figs. 4.4 and 2.3.

Though the shape and relative amplitudes of the lobes change with engine power, the spatiospectral location of the lobes remain fairly constant. Qualitative comparison of the lobe structure of the F-35 and T-7A shows that there is likely a scaling that would collapse the two aircraft spectra on top of each other.

The application of M-SONAH on the F-35 field extends the dense sampling of the near-field array into the far field, mapping the spatiospectral lobe trends across space. Figure 2.12 displays the trends of the lobes as a function of frequency and engine power; how each individual lobe shifts aft with increase in frequency while new lobes appear upstream to take their place. As engine power is increased, the forward-most lobe increases in its relative contribution to the field, causing the overall directivity at that frequency to shift towards the sideline. The source regions of the lobes are investigated in Fig. 2.9 by reconstructing the field along the nozzle lipline and Fig. 2.13, which traces the peak of each lobe to the jet centerline. The lowest-frequency lobe originates far downstream, while the second and third originate from similar locations further upstream, but several diameters aft of the nozzle.

7.2 LES Sound Field

Treatment of the LES database as if it were a measurement similar to the F-35 and T-7A has incentivized the use of coherence and NAH analyses, as opposed to more complicated full-field decomposition analyses that have been trending in jet noise research. The coherence of the field was calculated, which showed four distinct regions dominated by different radiation mechanisms: BBSAN, fine-scale turbulent structure noise, Mach wave radiation, and low-frequency aft radiation. Splitting the aft radiation into two regions based on their coherence properties follows observations of qualitative differences in the propagation of the waves in these regions [40, 41]. Quantitatively, these two aft regions are divided based on the presence of coherence with the upstream-radiating BBSAN.

Calculation of the coherence between the flow pressures sampled along the nozzle lipline and the acoustic pressures in the field show how information is transferred from the plume to the field. BBSAN is seen to originate in the potential core where shock cells are present, Mach wave radiation is seen to originate from the supersonic portion of the flow ($x/D < L_s$), and the far-aft, low-frequency information is seen originating just aft of L_s. The Mach wave radiation, which dominates over a large portion of the array, appears to translate information laterally, with spatially ordered packets of coherence lined up one after another along the lipline, beaming at a nearly constant angle to the field. Alternately, the low-frequency, far-aft radiation originates from an extended region around the end of the supersonic core and radiates over a large area less directionally.

The far aft radiation is therefore interpreted as large-scale turbulent structure noise, where the pressures caused by the structures create a coherent wavepacket over a finite area, causing the broad wavenumber spectrum to radiate some portion of their energy, even if the peak energy is subsonic. This causes less directional radiation, and as the acoustic field is sampled farther and farther aft beyond the end of the plume localizes the noise to this same region, instead of shifting source regions correspondingly far aft of the supersonic core.

The holography analysis in Chapter 6 shows that the vast majority of the radiated acoustic energy is due to the efficient Mach wave radiation in the supersonic portion of the flow, contrary to conclusions made by Sutherland et al. [46] and interpretation of the axial power per unit length of NASA SP-8072 [43]. Pressure reconstructions along the nozzle lipline follow the sound power reconstructions in terms of shape, which adds value to the lipline reconstructions of the F-35 in Fig. 2.9 as well as previous investigations of the jet noise source [36].

7.3 Holography Performance and Significance

Near-field acoustical holography provides a physics-based extrapolation of the measured field and allows for a more detailed investigation of the spatiospectral lobe phenomenon than measurement alone. Chapters 2 and 3 discuss the holographic reconstructions of the field of the F-35. The holography process is found to accurately represent the field within the aperture of the array, with an extended region where errors are found to be less than 2 dB. There exists some discrepancy between the ground interference effects observed in the measurement and predicted by the M-SONAH formulation, with reconstructions estimating the location of the interference null correctly towards the sideline but overestimating its depth. In the region of maximum radiation in the aft, well-defined nulls do not seem to appear in the spectra at all, though the holographic reconstructions predict something between that of cylindrically and spherically propagating waves. The M-SONAH procedure, therefore, does not completely capture the ground interference effects of the F-35 measurement, attesting to the extended, volumetric, and partially coherent nature of the jet noise source. For future extensions of the M-SONAH process to higher frequencies, more extensive investigations of the ground interference effects will be needed.

The SONAH algorithm is successfully applied to the LES in Chapter 6, with a number of notable improvements over the work in Chapters 2 and 3. First, the formulation from Ref. [142] was applied,

so that particle velocity fluctuations in addition to the pressures are reconstructed. Second, the aperture extension protocol was changed. Instead of the brute force method of Chapter 2 where the aperture of the hologram was extended large distances to either side of the array, the aperture extension in Chapter 6 was incorporated into the formulation of the EWM. By choosing a finer resolution of axial wavenumbers used in the EWM, the same effect as extending the aperture by a large number of points (compare sections 2.4.3 and 6.4.3) was achieved. This allowes for faster computation times and leaves less room for artifacts of the aperture extension to corrupt the data at the array edges.

Because pressure and particle velocities are now available from the holographic reconstructions, the acoustic intensity can be calculated as well. Chapter 6 investigates the overall sound power as well as axial distribution of sound power along the jet centerline from raytracing the intensity vectors. The overall levels match those derived directly from the LES vector intensity at the FWHS and from the squared pressures in the far-field, showing consistency with the FW-H integration method used to generate the pressures at the hologram. The interpretation of the reconstructions inside the flow along the nozzle lipline still remain somewhat ambiguous: the reconstructed pressures and reconstructed vector intensities are underestimated by about 4 dB and the TKE are underestimated by 26 dB. It is well understood that not all the pressure and velocity fluctuations are related to the far-field radiation, so underestimations are expected. However, the exact meaning of these specific offset values is elusive; the fact that the vector intensity magnitude calculations from the LES along the lipline agree fairly well is heartening, though more analytical work is needed to understand the effects of the axisymmetric assumptions on the holography inside the flow and the applicability of vector intensity calculations in a vortical, nonlinear flow.

The axial sound power distributions, however, do fit the overall shape of the lipline intensity magnitude and pressure fluctuations, suggesting that previous methods of obtaining sound source distributions by decomposing reconstructed pressures along the nozzle lipline are valid [36]. Spatial

integration of the sound power distributions shows that the majority (upwards of 90%) of the sound power is generated by radiation originating from the supersonic portion of the flow, with an almost half-and-half split of that energy coming from the potential core or between the potential and supersonic cores in the case of the LES. The coherence analysis of Chapter 5 shows this energetic portion of the flow to be dominated by Mach wave radiation.

7.4 Contributions

This works supplies significant new evidence for the presence of spatiospectral lobes in the aft radiation of high-performance military aircraft and, in conjunction with the LES, allows for explanations for part of the phenomenon.

The addition of the T-7A dataset to the growing number of measurements of military aircraft continues to show that the spatiospectral lobes are an important aspect of jet noise produced by high-performance military aircraft. Similar to previous aircraft measurements, considerable effort was put into organizing the collected data into a single package and writing functions where the waveforms corresponding to a particular channel or array of channels can be loaded easily. This has allowed, and will continue to allow, for ease of data analysis on this dataset for many students for years to come.

Though prior publication of parts of the F-35 dataset has been done, Chapter 2 represents the first peer-reviewed publication to explicitly examine in detail the spatiospectral lobes of the F-35. Preliminary investigation of the noise source region of each of the individual lobes is completed, though the limitation of not knowing specific jet flow data, such as Mach number or the length of the potential or supersonic cores of the jet at the various engine conditions halts further understanding.

The largest contribution of this work (and simultaneously, its greatest limitation) to the understanding of jet noise is the comparison of the F-35 and T-7A aircraft to LES of a highly heated

supersonic laboratory-scale jet. The qualitative comparisons provided herein allow for a broader description of the aft radiation of jet noise, but because of the lack of information of the military aircraft's exhaust, direct comparison between the F-35, the T-7A and LES cannot be done to conclusively verify these claims.

7.4.1 Source Narrative

The traditional description of supersonic flow exiting a nozzle is described thusly: flow exits the nozzle uniformly, with Kelvin-Helmholtz type perturbations originating at the nozzle lip growing as they are convected downstream. At some point, the turbulent shear layer grows on the boundary of the jet until the uniform flow is completely overtaken, marking the end of the potential core. The turbulent interaction of these eddies causes extensive mixing and the traditional turbulence cascade transfers this energy from large to smaller and smaller scales until they are dissipated at the Kolmogorov scale. The velocity thus decreases until reaching ambient conditions, with the point where the velocity is no longer supersonic being called the end of the supersonic core. When the jet is operated under nonideal conditions, shock cells appear in the flow, generally only seen in the potential core region.

The fine-scale turbulent structures throughout the flow radiate high-frequency noise nearly omnidirectionally, and are found throughout the plume, which dominates towards the sideline. The large-scale turbulent structures, as they convect downstream, create pressure fluctuations that are coherent over a large area, which generates directional radiation pointed towards the aft. As these structures pass through the shock cells, the actuated shock cells generate BBSAN that primarily radiates upstream.

The addition of the current work is the expansion of this understanding for highly heated laboratory-scale jets and military aircraft. With the extreme temperatures and velocities present, the phase relationship of the coherent structures upstream of the supersonic core (and particularly

of the potential core) are supersonic, creating efficient Mach wave radiation. As the phase speed decreases as the flow slows down, the peak frequency of the Mach wave radiation decreases until the phase relationship of the correlated pressures becomes subsonic, generally near the end of the supersonic core. At this point, though the peak of the wavenumber spectrum of the coherent pressures is subsonic, since it is of finite width there are still significant portions of the energy that are supersonic. This causes less efficient, more omnidirectional radiation from an extended area.

The characterization of these two regions and radiation types are shown in the coherence analysis of Fig. 5.7. The frequency-averaged coherent envelopes upstream of the potential core are spatially ordered and partially overlapping, with the directional radiation creating parallel rays or quasi plane-wave like radiation in this region. Farther aft, the frequency-averaged coherence becomes markedly smaller, but spread over a broader spatial range. This suggests a multiplicity of overlapping, inefficiently radiating wavepackets in the region around the end of the supersonic core.

7.4.2 Potential Causes of the Spatiospectral Lobes

The difference between the highly efficient Mach wave radiation originating from the supersonic portion of the flow and the less efficient radiation from the subsonic portion of the flow describe the underlying pattern of the radiation in the spatiospectral domain. As seen in the LES, the field has a smooth transition from one mechanism to the other, creating the overall “L” or “backwards J” signature seen in Fig. 6.4, as well as in the F-35 and T-7A measurements in Figs. 2.3 and 4.4. The foot of the “L” (or in the case of the F-35, lobe 1) is then interpreted as the radiation from the subsonic wavepackets centered along the end of the supersonic core and the shaft of the “L” (or lobes 2-5 in the F-35) is due to the Mach wave radiation from supersonic wavepackets lining the shear layer from the nozzle exit on down.

Recent decomposition work [31] has shown a similar description of the jet noise field in unheated subsonic and supersonic jets. The fields from several simulated jets were decomposed using SPOD

and resolvent analysis, finding differences between the noise generation mechanisms in the potential core and the developed jet downstream.Schmidt et al. [31] describe the two noise production mechanisms (and corresponding wavepacket types) as Kelvin-Helmholtz instability waves and Orr waves. Kelvin-Helmholtz instabilities in the potential core region along the shear layer are generally accepted as the mechanism that generates the large-scale turbulent structures in subsonic and supersonic jets. Qualitative similarity between the wavepacket shapes educed in Ref. [31] and the coherent envelopes in Chapter 5 suggest that the large-scale turbulent structure noise, or the foot of the "L", is due to the Orr mechanism.

However, the additional diagonal streaks that splits the smoothly-varying field exemplified by the LES into the discrete lobes exemplified by the F-35 and T-7A measurements remain unexplained. The shaft of the "L" is only observed to be segmented into spatiospectral lobes in the LES when the coherence is calculated between a point on the nozzle lipline where shock cells are present to the field, in the same region where coherence between the BBSAN and the aft radiation is found, suggesting that shock cells are a potential candidate for this undiagnosed phenomenon.

Because of the observed relationship between the spatiospectral lobes and the potential core region where shocks are observed, these spatiospectral lobes may also be related to recent derivations of "trapped" waves in the potential core of jets [149, 150], which have been measured in the extreme near field of laboratory-scale jets [23].

7.5 Future work

Though hypotheses are presented to explain the difference between the two sections of the "L" shape, there still is no explanation of lobing behavior of the Mach wave radiation, other than it may be related to the presence of shock cells. A fundamental limitation to this work is the fact that

flow parameters are not available for military aircraft jets so publicly released LES have not been generated using the same parameters for comparison.

The introduction of the T-7A database provides the perfect pivoting point for a robust investigation of the spatiospectral lobes. Due to the training purpose of the aircraft and its use of the F-404 engine (which has been widely used by multiple governments for many years) disclosure of nozzle geometry and operating conditions are in the works. This allows for LES similar to those that were undertaken in Chapters 5 and 6 to be repeated with the exact nozzle geometry and exit conditions for the T-7A at the various engine powers. Not only will this provide for validation of the LES methodology (which, as of yet, has not been reproduced at the laboratory scale) but reproduction (or not) of the multiple lobes in the LES will allow for targeted investigations of the necessary parameters to reproduce this phenomenon. Such investigations could include the addition of a ground reflecting plane, a more realistic representation of the gas mixture in the exhaust, or inclusions of additional turbomachinery components upstream of the nozzle.

All of the conclusions in this work can then be rigorously explored. Wavepacket decompositions, holographic reconstructions, and coherence analyses of the LES can be undertaken to validate the differences between the supersonic and subsonic portions of the flow. Direct investigation of the Orr mechanism using stability analyses like in Ref. [128] is possible. If an idealized LES with the same parameters as the T-7A still does not reproduce the additional spatiospectral lobes within the Mach wave radiation, then differences between the simulations and full-scale aircraft measurements can be systematically explored to find the true cause.

If large-eddy simulations are successful in reproducing the spatiospectral lobe phenomenon, additional analyses can be undertaken to understand their properties. For example, knowledge of the directivity of the individual lobes can be connected to the convective Mach number of the flow region where they are originating. These convective Mach numbers could then be compared against various Mach number estimates that can be calculated from the LES flow. One promising

observation was made by Oertel [151, 152] (and further discussed by Tam and Hu [153]) that suggests the existence of multiple types of waves present in the flow with differing Mach numbers. With the flow and extreme near-field data available from the LES, comparisons of the spatiospectral lobes can be made to other potentially related phenomena such as trapped waves [23, 149, 150], where quasi-periodic structures in the spatiospectral domain have been observed in laboratory-scale jet measurements.

Along with understanding the physics of the spatiospectral lobe phenomenon, if LES simulations are deemed to be sufficiently accurate, this may eliminate the need for future measurement of military aircraft for environmental and community impact assessment altogether. Axial distributions of sound power or other reduced-order models of the jet noise may be derived, and a representation of the noise generated by the T-7A at all engine powers can be created. A database of jet noise models for many aircraft could eventually lead to a more complete understanding of scaling laws as has been done for subsonic jets.

Investigations of military aircraft jet noise are almost always limited by the lack of disclosure of pertinent flow variables. This work, however, has taken what is available from various datasets and has been able to draw significant conclusions about the spatiospectral lobe phenomenon and laid the groundwork for the next step of military aircraft research. Using the techniques and work provided herein as a starting point, development of a joint full-scale measurement and LES simulation analysis of the T-7A aircraft can begin. Quantitative, direct understanding of the as-yet undiagnosed reason for spatiospectral lobing in the Mach wave radiation of military aircraft can now be investigated.

Appendix A

List of Files Used to Generate Figures

This Appendix is a list of MATLAB scripts which were used to generate the results in this dissertation. The file structure relates to the Department of Physics and Astronomy's Git server (AKA "Pulsar").

Figure #	.m file location
2.1	BYU Acoustics/Jet Noise/Holography/AIAA2018/figure1.m
2.2	BYU Acoustics/Jet Noise/Holography/AIAA2018/figure27.m
2.3	BYU Acoustics/Jet Noise/Holography/AIAA2018/figure11.m
2.4	BYU Acoustics/Jet Noise/Holography/AIAA2018/new figures for review/ PartialFieldDecompositions.m
2.5	BYU Acoustics/Jet Noise/Holography/AIAA2018/figure21.m
2.6	BYU Acoustics/Jet Noise/Holography/AIAA2018/figure20.m
2.7-8	BYU Acoustics/Jet Noise/Holography/AIAA2018/new figures for review/ spatiospectralmap38marc.m

Figure #	.m file location
2.9	BYU Acoustics/Jet Noise/Holography/AIAA2018/figure23.m
2.10	BYU Acoustics/Jet Noise/Holography/AIAA2018/figure25.m
2.11	BYU Acoustics/Jet Noise/Holography/AIAA2018/figure26.m
2.12	BYU Acoustics/Jet Noise/Holography/AIAA2018/figure20.m
2.13	BYU Acoustics/Jet Noise/Holography/AIAA2018/figure24.m
3.1	BYU Acoustics/Jet Noise/Holography/JASA f35 holography/figure1.m
3.2	BYU Acoustics/Jet Noise/Holography/JASA f35 holography/figure2.m
3.3	BYU Acoustics/Jet Noise/Holography/JASA f35 holography/figure5.m
3.4	BYU Acoustics/Jet Noise/Holography/JASA f35 holography/figure12.m
3.5	BYU Acoustics/Jet Noise/Holography/JASA f35 holography/figure9.m
3.6	BYU Acoustics/Jet Noise/Holography/JASA f35 holography/figure8.m
3.7	BYU Acoustics/Jet Noise/Holography/JASA f35 holography/figure13.m
4.1	BYU Acoustics/Jet Noise/T-7A/Aaron/T7A_Plotting_MeasurementSchematic.m
4.3	BYU Acoustics/Jet Noise/T-7A/Aaron/T7A_Plotting_dSk_OASPL_Imaging.m
4.4	BYU Acoustics/Jet Noise/T-7A/Kevin/Script3.m
4.5	BYU Acoustics/Jet Noise/T-7A/Aaron/T7A_Plotting_ground_vs_aerial_spectra.m
4.6, 8-10	BYU Acoustics/Jet Noise/T-7A/reeses-stuff/Interpolation_plotting.m
4.7	BYU Acoustics/Jet Noise/T-7A/Aaron/T7A_Plotting_dSk_OASPL_Arcs.m
5.2	kleete/NumericalDataAnalysis/coherence/figure17.m
5.3	kleete/NumericalDataAnalysis/coherence/figure3.m
5.4	kleete/NumericalDataAnalysis/coherence/figure14.m
5.5	kleete/NumericalDataAnalysis/coherence/figure15.m
5.6	kleete/NumericalDataAnalysis/coherence/figure20.m

Figure #	.m file location
5.7	kleete/NumericalDataAnalysis/coherence/figure5.m
5.8	kleete/NumericalDataAnalysis/coherence/figure21.m
5.9	kleete/NumericalDataAnalysis/coherence/figure6.m
6.1	kleete/NumericalDataAnalysis/Holography/Script29.m
6.2	kleete/NumericalDataAnalysis/Holography/Script29.m
6.3	kleete/NumericalDataAnalysis/Holography/Script30.m
6.4-6.11	kleete/NumericalDataAnalysis/Holography/Script31.m
6.12, 6.14, 6.15	kleete/NumericalDataAnalysis/Holography/Script28.m
6.13	kleete/NumericalDataAnalysis/Holography/Script33.m

Bibliography

[1] D. Casalino, F. Diozzi, R. Sannino, and A. Paonessa, "Aircraft noise reduction technologies: a bibliographic review," Aerospace Science and Technology **12,** 1–17 (2008).

[2] S. A. McInerny, "Rocket noise - A review," AIAA Aeroacoustics Conference 1990-3891 (1990), https://doi.org/10.2514/6.1990-3981.

[3] C. P. Lubert, "Sixty years of launch vehicle acoustics," Proceedings of Meetings on Acoustics **31,** 040004 (2017), https://asa.scitation.org/doi/abs/10.1121/2.0000704.

[4] M. J. Lighthill and M. H. A. Newman, "On sound generated aerodynamically I. General theory," Proceedings of the Royal Society of London. Series A. Mathematical and Physical Sciences **211,** 564–587 (1952), https://royalsocietypublishing.org/doi/abs/10.1098/rspa.1952.0060.

[5] A. W. Morley, "Estimation of Aeroplane Noise Level: Some Empirical Laws with an Account of the Present Experiments on which they are Based," Aircraft Engineering and Aerospace Technology **11,** 187–189 (1939), https://doi.org/10.1108/eb030480.

[6] M. Goldstein, *Aeroacoustics*, *Advanced book program* (McGraw-Hill International Book Company, 1976).

[7] T. Suzuki, "A review of diagnostic studies on jet-noise sources and generation mechanisms of subsonically convecting jets," Fluid Dynamics Research **42,** 014001 (2010), https://doi.org/10.1088/0169-5983/42/1/014001.

[8] C. Tam, M. Golebiowski, and J. Seiner, "On the two components of turbulent mixing noise from supersonic jets," AIAA Aeroacoustics Conference 1996-1716 (1996), https://doi.org/10.2514/6.1996-1716.

[9] C. K. W. Tam, K. Viswanathan, K. K. Ahuja, and J. Panda, "The sources of jet noise: experimental evidence," Journal of Fluid Mechanics **615,** 253–292 (2008), https://doi.org/10.1017/S0022112008003704.

[10] H. K. Lee and H. S. Ribner, "Direct Correlation of Noise and Flow of a Jet," The Journal of the Acoustical Society of America **52,** 1280–1290 (1972).

[11] S. C. Crow and F. H. Champagne, "Orderly structures in jet turbulence," Journal of Fluid Mechanics **48,** 547–591 (1971), https://doi.org/10.1017/S0022112071001745.

[12] G. L. Brown and A. Roshko, "On density effects and large structures in turbulent mixing layers," Journal of Fluid Mechanics **64,** 775–816 (1974), https://doi.org/10.1017/S002211207400190X.

[13] C. Bogey and C. Bailey, "An analysis of the correlations between the turbulent flow and the sound pressure fields of subsonic jets," Journal of Fluid Mechanics **583,** 71–97 (2007), https://doi.org/10.1017/S002211200700612X.

[14] J. Panda and R. G. Seasholtz, "Experimental investigation of density fluctuation in high-speed jets and correlation with generated noise," Journal of Fluid Mechanics **450,** 97–130 (2002), https://doi.org/10.1017/S002211200100622X.

[15] J. Panda, R. G. Seasholtz, and K. A. Elam, "Investigation of noise sources in high-speed jets via correlation measurements," Journal of Fluid Mechanics **537,** 349–385 (2005), https://doi.org/10.1017/S0022112005005148.

[16] C. K. W. Tam and L. Auriault, "Jet mixing noise from fine-scale turbulence," AIAA Journal **37,** 145–153 (1999), https://doi.org/10.2514/2.691.

[17] C. K. W. Tam and K. C. Chen, "A statistical model of turbulence in two-dimensional mixing layers," Journal of Fluid Mechanics **92,** 303–326 (1979), https://doi.org/10.1017/S002211207900063X.

[18] H. K. Tanna, "An experimental study of jet noise part ii: shock associated noise," Journal of Sound and Vibration **50,** 429–444 (1977), https://doi.org/10.1016/0022-460X(77)90494-1.

[19] C. Tam, "Stochastic model theory of broadband shock associated noise from supersonic jets," Journal of Sound and Vibration **116,** 265 – 302 (1987), https://doi.org/10.1016/S0022-460X(87)81303-2.

[20] G. Raman, "Supersonic Jet Screech: Half-Century from Powell to the Present," Journal of Sound and Vibration **225,** 543–571 (1999), https://www.sciencedirect.com/science/article/pii/S0022460X99921818.

[21] T. B. Neilsen, A. B. Vaughn, K. L. Gee, S. H. Swift, A. T. Wall, J. M. Downing, and M. M. James, "Inclusion of Broadband Shock-Associated Noise in Spectral Decomposition of Noise from High-performance Military Aircraft," AIAA/CEAS Aeroacoustics Conference 2018-3146 (2018), https://doi.org/10.2514/6.2018-3146.

[22] K. L. Gee, T. B. Neilsen, A. T. Wall, J. M. Downing, and M. M. James, "The 'sound of freedom': Characterizing jet noise from high-performance military aircraft," Acoustics Today **9,** 8–21 (2013).

[23] A. F. Fagan and K. Q. Zaman, "Rayleigh-scattering-based measurement of 'trapped waves' in high-speed jets," AIAA Aviation Forum 2020-2524 (2020), https://arc.aiaa.org/doi/abs/10.2514/6.2020-2524.

[24] R. J. Adrian, "Twenty years of particle image velocimetry," Experiments in fluids **39,** 159–169 (2005).

[25] G. S. Settles and M. J. Hargather, "A review of recent developments in schlieren and shadowgraph techniques," Measurement Science and Technology **28,** 042001 (2017).

[26] K. Taira, S. L. Brunton, S. T. M. Dawson, C. W. Rowley, T. Colonius, B. J. McKeon, O. T. Schmidt, S. Gordeyev, V. Theofilis, and L. S. Ukeiley, "Modal Analysis of Fluid Flows: An Overview," AIAA Journal **55,** 4013–4041 (2017), https://doi.org/10.2514/1.J056060.

[27] S. Unnikrishnan and D. V. Gaitonde, "Acoustic, hydrodynamic and thermal modes in a supersonic cold jet," Journal of Fluid Mechanics **800,** 387–432 (2016), https://doi.org/10.1017/jfm.2016.410.

[28] S. Unnikrishnan, K. Goparaju, and D. Gaitonde, "Energy-Dynamics Resulting in Turbulent and Acoustic Phenomena in an Underexpanded Jet," Aerospace 5 (2018), https://doi.org/10.3390/aerospace5020049.

[29] V. Theofilis, "Global Linear Instability," Annual Review of Fluid Mechanics **43,** 319–352 (2011), https://doi.org/10.1146/annurev-fluid-122109-160705.

[30] P. Jordan, M. Zhang, G. Lehnasch, and A. V. Cavalieri, "Modal and non-modal linear wavepacket dynamics in turbulent jets," AIAA/CEAS Aeroacoustics Conference 2017-3379 (2017), https://doi.org/10.2514/6.2017-3379.

[31] O. T. Schmidt, A. Towne, G. Rigas, T. Colonius, and G. A. Brès, "Spectral analysis of jet turbulence," Journal of Fluid Mechanics **855,** 953–982 (2018), https://doi.org/10.1017/jfm.2018.675.

[32] P. J. Schmid and J. Sesterhenn, "Dynamic Mode Decomposition of Numerical and Experimental Data," Journal of Fluid Mechanics **656,** 5–28 (2010), https://doi.org/10.1017/S0022112010001217.

[33] A. Towne, O. T. Schmidt, and T. Colonius, "Spectral proper orthogonal decomposition and its relationship to dynamic mode decomposition and resolvent analysis," Journal of Fluid Mechanics **847,** 821–867 (2018), https://doi.org/10.1017/jfm.2018.283.

[34] P. Jordan and T. Colonius, "Wave Packets and Turbulent Jet Noise," Annual Review of Fluid Mechanics **45,** 173–195 (2013), https://doi.org/10.1146/annurev-fluid-011212-140756.

[35] B. M. Harker, K. L. Gee, T. B. Neilsen, A. T. Wall, and M. M. James, "Beamforming-Based Wavepacket Model for Noise Environment Predictions of Tactical Aircraft," AIAA/CEAS Aeroacoustics Conference 2017-4048 (2017), https://doi.org/10.2514/6.2017-4048.

[36] A. T. Wall, K. L. Gee, K. M. Leete, T. B. Neilsen, T. A. Stout, and M. M. James, "Partial-field decomposition analysis of full-scale supersonic jet noise using optimized-location virtual references," The Journal of the Acoustical Society of America **144,** 1356–1367 (2018), https://doi.org/10.1121/1.5053580.

[37] A. S. Lyrintzis and M. Coderoni, "Overview of the use of large-eddy simulations in jet aeroacoustics," AIAA Journal **58,** 1620–1638 (2020).

[38] J. E. Ffowcs Williams, D. L. Hawkings, and M. J. Lighthill, "Sound generation by turbulence and surfaces in arbitrary motion," Philosophical Transactions of the Royal Society of London. Series A, Mathematical and Physical Sciences **264,** 321–342 (1969).

[39] J. Liu, A. T. Corrigan, K. Kailasanath, and B. D. Taylor, "Impact of the Specific Heat Ratio On the Noise Generation in a High-Temperature Supersonic Jet," AIAA SciTech Forum 2016-2125 (2016), https://doi.org/10.2514/6.2016-2125.

[40] J. Liu, K. Kailasanath, and E. J. Gutmark, "Similarity Spectra Analysis in Highly Heated Supersonic Jets Using Large-Eddy Simulations," AIAA SciTech Forum 2017-0926 (2017), https://doi.org/10.2514/6.2017-0926.

[41] S. Chen, R. Gojon, and M. Mihaescu, "High-temperature effects on aerodynamic and acoustic characteristics of a rectangular supersonic jet," AIAA/CEAS Aeroacoustics Conference 2018-3303 (2018), https://doi.org/10.2514/6.2018-3303.

[42] S. Chen and M. Mihaescu, "Nozzle Pressure Ratio Effects on Aerodynamics and Acoustics of a Highly-Heated Rectangular Supersonic Jet," AIAA/CEAS Aeroacoustics Conference 2019-2753 (2019), https://arc.aiaa.org/doi/abs/10.2514/6.2019-2753.

[43] K. M. Eldred, *Acoustic Loads Generated by the Propulsion System*, No. 8072 in *NASA SP* (1971), https://ntrs.nasa.gov/citations/19710023719.

[44] R. Potter, "An investigation to locate the acoustic sources in a high speed jet exhaust stream," NASA CR-101105 (1968).

[45] G. Horvay and H. Nagamatsu, "Supersonic jet noise," AIAA Aerospace Sciences Meeting (1970), https://doi.org/10.2514/6.1970-237.

[46] L. C. Sutherland, "Progress and problems in rocket noise prediction for ground facilities," AIAA Aeroacoustics Conference 1993-4383 (1993), https://doi.org/10.2514/6.1993-4383.

[47] K. Plotkin, L. Sutherland, and B. Vu, "Lift-Off Acoustics Predictions for the Ares I Launch Pad," AIAA/CEAS Aeroacoustics Conference 2009-3163 (2009).

[48] S. A. Kumar and N. Karthikeyan, "Prediction of Launch Vehicle Noise during Lift-off using a Modified Eldred's Method," The 14th Asian Congress of Fluid Mechanics (2013).

[49] M. M. James, A. R. Salton, K. L. Gee, and T. B. Neilsen, "Comparative Analysis of NASA SP-8072's Core Length with Full-Scale Rocket Data," Transactions of the Japan Society for Aeronautical and Space Sciences, Aerospace Technology Japan 14 (2016), https://doi.org/10.2322/tastj.14.Po_2_17.

[50] J. Varnier, "Experimental Study and Simulation of Rocket Engine Freejet Noise," AIAA Journal **39,** 1851–1859 (2001), https://doi.org/10.2514/2.1199.

[51] D. Casalino, M. Barbarino, M. Genito, and V. Ferrara, "Hybrid Empirical/Computational Aeroacoustics Methodology for Rocket Noise Modeling," AIAA Journal **47,** 1445–1460 (2009), https://doi.org/10.2514/1.38634.

[52] K. L. Gee, "A tale of two curves and their influence on rocket and supersonic jet noise research," the Journal of the Acoustical Society of America (Accepted 2021).

[53] D. Long and R. Arndt, "The role of Helmholtz number in jet noise," 22nd Aerospace Sciences Meeting (1984), https://doi.org/10.2514/6.1984-403.

[54] A. T. Wall, K. L. Gee, M. M. James, K. A. Bradley, S. A. McInerny, and T. B. Neilsen, "Near-field noise measurements of a high performance military jet aircraft," Noise Control Engineering Journal **60,** 421–434 (2012), https://doi.org/10.3397/1.3701021.

[55] M. M. James, A. R. Salton, J. M. Downing, K. L. Gee, T. B. Neilsen, B. O. Reichman, R. McKinley, A. T. Wall, and H. Gallagher, "Acoustic Emissions from F-35 Aircraft during Ground Run-Up," 21st AIAA/CEAS Aeroacoustics Conference 2015-2375 (2015), https://doi.org/10.2514/6.2015-2375.

[56] C. K. Tam, A. C. Aubert, J. T. Spyropoulos, and R. W. Powers, "On the dominant noise components of tactical aircraft: Laboratory to full scale," Journal of Sound and Vibration **422,** 92–111 (2018), https://doi.org/10.1016/j.jsv.2018.02.023.

[57] T. B. Neilsen, K. L. Gee, A. T. Wall, and M. M. James, "Similarity spectra analysis of high-performance jet aircraft noise," The Journal of the Acoustical Society of America 133 (2013), https://doi.org/10.1121/1.4792360.

[58] T. B. Neilsen, A. B. Vaughn, K. L. Gee, S. H. Swift, A. T. Wall, J. M. Downing, and M. M. James, "Three-Way Spectral Decompositions of High-Performance Military Aircraft Noise," AIAA Journal **57,** 3467–3479 (2019), https://doi.org/10.2514/1.J057992.

[59] C. K. W. Tam and S. A. Parrish, "Noise of high-performance aircraft at afterburner," Journal of Sound and Vibration **352,** 103–128 (2015), https://doi.org/10.1016/j.jsv.2015.04.010.

[60] B. M. Harker, T. B. Neilsen, K. L. Gee, A. T. Wall, and M. M. James, "Spatiotemporal-Correlation Analysis of Jet Noise from a High-Performance Military Aircraft," AIAA Journal **54,** 1554–1566 (2016), https://doi.org/10.2514/1.J054442.

[61] S. H. Swift, K. L. Gee, T. B. Neilsen, A. T. Wall, J. M. Downing, and M. M. James, "Spatiotemporal-correlation analysis of jet noise from a round nozzle high-performance aircraft," AIAA/CEAS Aeroacoustics Conference 2018-3938 (2018), https://doi.org/10.2514/6.2018-3938.

[62] R. W. Powers, D. K. McLaughlin, and P. J. Morris, "Noise Reduction in Supersonic Jets Exhausting over a Simulated Aircraft Carrier Deck," Journal of Aircraft **55,** 310–324 (2018), https://doi.org/10.2514/1.C034213.

[63] T. J. Worden, C. Shih, and F. S. Alvi, "Supersonic Jet Impingement on a Model-Scale Jet Blast Deflector," AIAA Journal **55,** 2522–2536 (2017), https://doi.org/10.2514/1.J055664.

[64] U. H. von Glahn, J. H. Goodykoontz, and J. M. Wagner, "Nozzle geometry and forward velocity effects on noise for CTOL engine-over-the-wing concept," NASA Technical Reports Server (1973), https://ntrs.nasa.gov/search.jsp?R=19730025009.

[65] G. G. Podboy, "Jet-Surface interaction test: phased array noise source localization results," ASME Turbo Expo 2012: Turbine Technical Conference and Exposition pp. 381–414 (2012), https://doi.org/10.1115/GT2012-69801.

[66] C. A. Brown, "Jet-Surface Interaction Test: Far-Field Noise Results," Journal of Engineering for Gas Turbines and Power 135 (2013), https://doi.org/10.1115/1.4023605.

[67] L. Rego, D. Casalino, F. Avallone, and D. Ragni, "Noise Amplification Effects due to Jet-Surface Interaction," AIAA Scitech Forum 2019-0001 (2019), https://doi.org/10.2514/6.2019-0001.

[68] E. G. Williams, *Fourier Acoustics* (Academic Press, 1999), .

[69] P. Chiariotti, M. Martarelli, and P. Castellini, "Acoustic beamforming for noise source localization – Reviews, methodology and applications," Mechanical Systems and Signal Processing **120,** 422–448 (2019), https://doi.org/10.1016/j.ymssp.2018.09.019.

[70] R. P. Dougherty, "Improved Generalized Inverse Beamforming for Jet Noise," International Journal of Aeroacoustics **11,** 259–289 (2012), https://doi.org/10.1260/1475-472X.11.3-4.259.

[71] G. G. Podboy, J. E. Bridges, and B. S. Henderson, "Phased Array Noise Source Localization Measurements of an F404 Nozzle Plume at Both Full and Model Scale," Turbo Expo: Power for Land, Sea, and Air pp. 179–208 (2010), https://doi.org/10.1115/GT2010-22601.

[72] D. Papamoschou, D. Morata, and P. Shah, "Inverse Acoustic Methodology for Continuous-Scan Phased Arrays," AIAA Journal (2019).

[73] R. Schlinker, S. Liljenberg, D. Polak, K. Post, C. Chipman, and A. Stern, "Supersonic Jet Noise Characteristics & Propagation: Engine and Model Scale," AIAA/CEAS Aeroacoustics Conference 2007-3623 (2007), https://arc.aiaa.org/doi/abs/10.2514/6.2007-3623.

[74] L. Brusniak, J. Underbrink, E. Nesbitt, D. Lynch, and M. Martinez, "Phased Array Measurements of Full-Scale Engine Exhaust Noise," AIAA/CEAS Aeroacoustics Conference 2007-3612 (2007), https://arc.aiaa.org/doi/abs/10.2514/6.2007-3612.

[75] B. M. Harker, K. L. Gee, T. B. Neilsen, A. T. Wall, and M. M. James, "Source characterization of full-scale tactical jet noise from phased-array measurements," The Journal of the Acoustical Society of America **146,** 665–680 (2019), https://doi.org/10.1121/1.5118239.

[76] J. D. Maynard, E. G. Williams, and Y. Lee, "Nearfield acoustical holography: 1. Theory of generalized holography and the development of NAH," The Journal of the Acoustical Society of America **78,** 1395–1413 (1985), https://doi.org/10.1121/1.392911.

[77] J. Hald, "Basic theory and properties of statistically optimized near-field acoustical holography," The Journal of the Acoustical Society of America **125,** 967–977 (2009), https://doi.org/10.1121/1.3079773.

[78] M. Lee and J. Bolton, "Source characterization of a subsonic jet by using near-field acoustical holography," The Journal of the Acoustical Society of America **121,** 967–977 (2007), https://doi.org/10.1121/1.2404626.

[79] D. Long, "Evaluation of Jet and Shock Cell Noise via Acoustic Holography," AIAA Aerospace Sciences Meeting and Exhibit (2008), https://doi.org/10.2514/6.2008-5.

[80] P. Shah, H. Vold, and M. Yang, "Reconstruction of Far-Field Noise Using Multireference Acoustical Holography Measurements of High-Speed Jets," AIAA/CEAS Aeroacoustics Conference 2011-2772 (2011), https://doi.org/10.2514/6.2011-2772.

[81] P. N. Shah, H. Vold, D. Hensley, E. Envia, and D. Stephens, "A High-Resolution Continuous-Scan Acoustic Measurement Method for Turbofan Engine Applications," Journal of Turbomachinery 137 (2015), https://doi.org/10.1115/1.4031341.

[82] A. T. Wall, K. L. Gee, and T. B. Neilsen, "Multisource statistically optimized near-field acoustical holography," The Journal of the Acoustical Society of America **137,** 963–975 (2015), https://doi.org/10.1121/1.4906585.

[83] A. T. Wall, K. L. Gee, T. B. Neilsen, R. L. McKinley, and M. M. James, "Military jet noise source imaging using multisource statistically optimized near-field acoustical holography," The Journal of the Acoustical Society of America **139,** 1938–1950 (2016), https://doi.org/10.1121/1.4945719.

[84] A. T. Wall, Ph.D. thesis, Brigham Young University, 2013.

[85] A. T. Wall, K. M. Leete, K. L. Gee, T. B. Neilsen, M. M. James, and R. L. McKinley, "Preliminary Investigation of Multilobe Fighter Jet Noise Sources Using Acoustical Holography," AIAA/CEAS Aeroacoustics Conference 2017-3520 (2017), https://doi.org/10.2514/6.2017-3520.

[86] J. A. Ward, S. H. Swift, K. L. Gee, T. B. Neilsen, K. Okamoto, and M. Akamine, "Frequency-dependent jet noise source localization using cross-correlation between near and far-field microphone arrays," Proceedings of Meetings on Acoustics **31,** 040005 (2017), https://asa.scitation.org/doi/abs/10.1121/2.0000810.

[87] D. Long, "Jet Noise Source Location via Acoustic Holography and Shadowgraph Imagery," AIAA/CEAS Aeroacoustics Conference 2008-2888 (2008), https://doi.org/10.2514/6.2008-2888.

[88] A. B. Vaughn, T. B. Neilsen, K. L. Gee, A. T. Wall, J. Micah Downing, and M. M. James, "Broadband shock-associated noise from a high-performance military aircraft," The Journal of the Acoustical Society of America **144,** EL242–EL247 (2018), https://doi.org/10.1121/1.5055392.

[89] K. M. Leete, A. B. Vaughn, M. S. Bassett, R. D. Rasband, D. J. Novakovich, K. L. Gee, S. C. Campbell, F. S. Mobley, and A. T. Wall, "Jet Noise Measurements of an Installed GE F404 Engine," AIAA Scitech Forum 2021-1638 (2021), https://doi.org/10.2514/6.2021-1638.

[90] J. Liu, A. T. Corrigan, K. Kailasanath, N. S. Heeb, and E. J. Gutmark, "Numerical Study of Noise Sources Characteristics in An Underexpanded Jet Flow," AIAA/CEAS Aeroacoustics Conference 2014-2604 (2014), https://doi.org/10.2514/6.2014-2604.

[91] J. Liu, A. T. Corrigan, K. Kailasanath, and E. J. Gutmark, "Impact of Chevrons on Noise Source Characteristics In Imperfectly Expanded Jet Flows," AIAA/CEAS Aeroacoustics Conference 2015-2835 (2015), https://doi.org/10.2514/6.2015-2835.

[92] K. M. Leete, K. L. Gee, J. Liu, and A. T. Wall, "Coherence Analysis of the Noise from a Simulated Highly Heated Laboratory-Scale Jet," AIAA Journal **58,** 3426–3435 (2020), https://doi.org/10.2514/1.J059112.

[93] R. Steiner and J. Hald, "Near-field acoustical holography without the errors and limitations caused by the use of spatial DFT," International Journal of Acoustics and Vibration **6,** 83–89 (2001).

[94] J. Hald, "STSF - a unique technique for scan-based Near-field Acoustic Holography without restrictions on coherence," Bruel & Kjaer Technical Review (1989).

[95] A. T. Wall, K. L. Gee, D. W. Krueger, T. B. Neilsen, S. D. Sommerfeldt, and M. M. James, "Aperture extension for near-field acoustical holography of jet noise," Proceedings of Meetings on Acoustics **14,** 065001 (2013), https://doi.org/10.1121/1.4794833.

[96] Y. T. Cho, J. S. Bolton, and J. Hald, "Source Visualization by using statistically optimized near-field acoustical holography in cylindrical coordinates," The Journal of the Acoustical Society of America **118,** 2355–2364 (2005), https://doi.org/10.1121/1.2036252.

[97] E. G. Williams, "Regularization methods for near-field acoustical holography," The Journal of the Acoustical Society of America **110,** 1976–1988 (2001), https://doi.org/10.1121/1.1404381.

[98] K. M. Leete, A. T. Wall, K. L. Gee, T. B. Neilsen, J. M. Downing, and M. M. James, "Numerical validation of using multisource statistically-optimized near-field acoustical holography in the vicinity of a high-performance military aircraft," Proceedings of Meetings on Acoustics **31,** 040007 (2017), https://doi.org/10.1121/2.0000895.

[99] J. Laufer, R. H. Schlinker, and R. E. Kaplan, "Experiments on supersonic jet noise," AIAA Journal **14,** 489–497 (1976), https://doi.org/10.2514/3.61388.

[100] J. I. Hileman, B. S. Thurow, E. J. Caraballo, and M. Samimy, "Large-scale structure evolution and sound emission in high-speed jets: real-time visualization with simultaneous acoustic measurements," Journal of Fluid Mechanics **544,** 277–307 (2005), https://doi.org/10.1017/S002211200500666X.

[101] N. E. Murray and W. J. Baars, "Passive Nozzle-Based Technology for the Reduction of Heated Supersonic Jet Noise," AIAA/CEAS Aeroacoustics Conference 2019-2729 (2019), https://doi.org/10.2514/6.2019-2729.

[102] T. A. Stout, K. L. Gee, T. B. Neilsen, A. T. Wall, and M. M. James, "Acoustic intensity near a high-powered military jet aircraft," The Journal of the Acoustical Society of America **138,** EL1–EL7 (2015), https://doi.org/10.1121/1.4921746.

[103] T. A. Stout, K. L. Gee, T. B. Neilsen, A. T. Wall, and M. M. James, "Source characterization of full-scale jet noise using acoustic intensity," Noise Control Engr. J. **63,** 522 – 536 (2015), https://doi.org/10.3397/1/376346.

[104] A. T. Wall, K. L. Gee, T. B. Neilsen, D. W. Krueger, and M. M. James, "Cylindrical acoustical holography applied to full-scalle jet noise," The Journal of the Acoustical Society of America **136,** 1120–1128 (2014).

[105] K. M. Leete, A. T. Wall, K. L. Gee, T. B. Neilsen, M. M. James, and J. M. Downing, "Dependence of High-performance Military Aircraft Noise on Frequency and Engine Power," AIAA/CEAS Aeroacoustics Conference 2018-2826 (2018), https://doi.org/10.2514/6.2018-2826.

[106] T. B. Neilsen, A. B. Vaughn, K. L. Gee, M. Akamine, K. Okamoto, S. Tsutsumi, and S. Teramoto, "Level-educed Wavepacket Representation of Mach 1.8 Laboratory-Scale Jet Noise," AIAA/CEAS Aeroacoustics Conference 2017-4049 (2017), https://arc.aiaa.org/doi/abs/10.2514/6.2017-4049.

[107] J. Morgan, T. B. Neilsen, K. L. Gee, A. T. Wall, and M. M. James, "Simple-source model of high-power jet aircraft noise," Noise Control Engineering Journal **60,** 435–449 (2012).

[108] D. Papamoschou, "Wavepacket modeling of the jet noise source," International Journal of Aeroacoustics **17,** 52–69 (2018).

[109] B. Greska, A. Krothapalli, J. Seiner, B. Jansen, and L. Ukeiley, "The effects of microjet injection on an F404 jet engine," AIAA/CEAS Aeroacoustics Conference 2005-3047 (2005), https://doi.org/10.2514/6.2005-3047.

[110] J. Seiner, L. Ukeiley, and B. Jansen, "Aero-performance efficient noise reduction for the F404-400 engine," AIAA/CEAS Aeroacoustics Conference 2005-3048 (2005), https://doi.org/10.2514/6.2005-3048.

[111] N. E. Murray and B. J. Jansen, "Performance Efficient Jet Noise Reduction for Supersonic Nozzles," International Journal of Aeroacoustics **11,** 937–956 (2012), https://doi.org/10.1260/1475-472X.11.7-8.93.

[112] J. Seiner, B. Jansen, and N. Murray, "Aero-performance efficient noise suppression of a supersonic model twin jet nacelle," AIAA/CEAS Aeroacoustics Conference (2009), https://doi.org/10.2514/6.2009-3130.

[113] J. Liu and R. Ramamurti, "Numerical Study of Supersonic Jet Noise Emanating from an F404 Nozzle at Model Scale," AIAA Scitech 2019 Forum 2019-0807 (2019), https://doi.org/10.2514/6.2019-0807.

[114] C. K. Tam, A. C. Aubert, J. T. Spyropoulos, and R. W. Powers, "On the Dominant Noise Components of Tactical Aircraft: Laboratory to Full Scale," AIAA/CEAS Aeroacoustics Conference 2017-3516 (2017), https://doi.org/10.2514/6.2017-3516.

[115] R. D. Rasband, A. T. Wall, K. L. Gee, S. H. Swift, C. M. Wagner, W. J. Murphy, and C. A. Kardous, "Impulse noise measurements of M16 rifles at Marine Base Quantico," Proceedings of Meetings on Acoustics **33,** 040003 (2018).

[116] B. O. Reichman, B. Harker, T. Stout, E. Whiting, K. Gee, and T. Neilsen, "Acoustical measurements during a static firing of the Space Launch System solid rocket motor," Proceedings of Meetings on Acoustics **25,** 045006 (2015).

[117] B. O. Reichman, B. M. Harker, T. B. Neilsen, K. L. Gee, and W.-S. Ohm, "Acoustic measurements in the far field during QM-2 solid rocket motor static firing," Proceedings of Meetings on Acoustics **29,** 045008 (2016).

[118] J. E. Ffowcs Williams, J. Simson, and V. J. Virchis, "'Crackle': An annoying component of jet noise," Journal of Fluid Mechanics **71,** 251–271 (1975).

[119] A. B. Vaughn, K. L. Gee, S. H. Swift, A. T. Wall, J. M. Downing, and M. M. James, "Beamforming of supersonic jet noise for crackle-related events," Proc. Mtgs. Acoust. **35,** 040003 (2018).

[120] A. B. Vaughn, K. L. Gee, S. H. Swift, K. M. Leete, A. T. Wall, J. M. Downing, and M. M. James, "Crackle-related beamforming of military jet aircraft noise," AIAA/CEAS Aeroacoustics Conference 2019-2664 (2019), https://doi.org/10.2514/6.2019-2664.

[121] P. B. Russavage, T. B. Neilsen, K. L. Gee, and S. H. Swift, "Rating the perception of jet noise crackle," Proc. Mtgs. Acoust. **33,** 040001 (2018).

[122] S. H. Swift, K. L. Gee, and T. B. Neilsen, "Testing two crackle criteria using modified jet noise waveforms," The Journal of the Acoustical Society of America **141,** EL549–EL554 (2017).

[123] A. T. Wall, K. L. Gee, T. B. Neilsen, S. A. McInerny, and M. M. James, "Investigation of multi-lobed fighter jet noise sources using acoustical holography and partial field decomposition methods," AIAA/CEAS Aeroacoustics Conference 2015-2379 (2015), https://doi.org/10.2514/6.2015-2379.

[124] K. Viswanathan, J. R. Underbrink, and L. Brusniak, "Space-Time Correlation Measurements in Nearfields of Jets," AIAA Journal **49,** 1577–1599 (2011), https://doi.org/10.2514/1.J050750.

[125] J. M. Seiner, M. K. Ponton, B. J. Jansen, and N. T. Lagen, "The effects of temperature on supersonic jet noise emission," DGLR/AIAA Aeroacoustics Conference **1,** 295–307 (1992).

[126] D. J. Bodony and S. K. Lele, "Current Status of Jet Noise Predictions Using Large-Eddy Simulation," AIAA Journal **46,** 364–380 (2008), https://doi.org/10.2514/1.24475.

[127] G. A. Bres and S. K. Lele, "Modelling of jet noise: a perspective from large-eddy simulations," Philosophical Transactions of the Royal Society A: Mathematical, Physical and Engineering Sciences **377,** 20190081 (2019), https://royalsocietypublishing.org/doi/abs/10.1098/rsta.2019.0081.

[128] G. Tissot, F. C. Lajús, A. V. G. Cavalieri, and P. Jordan, "Wave packets and Orr mechanism in turbulent jets," Phys. Rev. Fluids **2,** 093901 (2017), https://link.aps.org/doi/10.1103/PhysRevFluids.2.093901.

[129] R. Löhner, K. Morgan, J. Peraire, and M. Vahdati, "Finite element flux-corrected transport (FEM–FCT) for the euler and Navier–Stokes equations," International Journal for Numerical Methods in Fluids **7,** 1093–1109 (1987), https://onlinelibrary.wiley.com/doi/abs/10.1002/fld.1650071007.

[130] A. S. Lyrintzis, "Surface integral methods in computational aeroacoustics—From the (CFD) near-field to the (Acoustic) far-field," International journal of aeroacoustics **2,** 95–128 (2003), https://doi.org/10.1260/147547203322775498.

[131] J. Liu, K. Kailasanath, J. Boris, N. Heeb, D. Munday, and E. Gutmark, "Effect of Nozzle-exit Flow Conditions on the Flow and Acoustic Properties of Imperfectly Ex-

panded Supersonic Jets," AIAA/CEAS Aeroacoustics Conference 2012-2161 (2012), https://doi.org/10.2514/6.2012-2161.

[132] J. T. Walton and F. W. Burcham, "Exhaust-gas pressure and temperature survey of F404-GE-400 turbofan engine," NASA Technical Memorandum 88273 (1986), https://ntrs.nasa.gov/archive/nasa/casi.ntrs.nasa.gov/19880010923.pdf.

[133] G. A. Bres, A. Towne, and S. K. Lele, "Investigating the effects of temperature non-uniformity on supersonic jet noise with large-eddy simulation," AIAA/CEAS Aeroacoustics Conference 2019-2730 (2019), https://arc.aiaa.org/doi/abs/10.2514/6.2019-2730.

[134] C. K. W. Tam, "Mach Wave Radiation from High-Speed Jets," AIAA Journal **47,** 2440–2448 (2009), https://doi.org/10.2514/1.42644.

[135] J. S. Bendat and A. G. Piersol, *Random Data*, 2nd ed. (Wiley-interscience, 605 Third Avenue, New York, N.Y. 10158, 1986).

[136] I. A. Maia, P. Jordan, A. V. G. Cavalieri, and V. Jaunet, "Two-point wavepacket modelling of jet noise," Proceedings of the Royal Society A: Mathematical, Physical and Engineering Sciences **475,** 20190199 (2019), https://royalsocietypublishing.org/doi/abs/10.1098/rspa.2019.0199.

[137] K. L. Gee, M. Akamine, K. Okamoto, T. B. Neilsen, S. Tsutsumi, S. Teramoto, T. Okunuki, and M. Cook, "Characterization of Supersonic Laboratory-Scale Jet Noise with Vector Acoustic Intensity," AIAA/CEAS Aeroacoustics Conference 2017-3519 (2017), https://doi.org/10.2514/6.2017-3519.

[138] K. M. Leete, A. T. Wall, K. L. Gee, M. M. James, and J. M. Downing, "Acoustical Holography-based Analysis of Spatiospectral Lobes in High-performance Aircraft Jet Noise," AIAA Journal (Accepted Feb. 2021).

[139] M. Fisher, M. Harper-Bourne, and S. Glegg, "Jet engine noise source location: The polar correlation technique," Journal of Sound and Vibration **51,** 23–54 (1977), https://www.sciencedirect.com/science/article/pii/S0022460X77801119.

[140] Y. Du and P. Morris, "Numerical Investigation of the Noise Source Locations of Supersonic Jets Using the Beamformed Method," AIAA Aerospace Sciences Meeting 2012-1169 (2012), https://doi.org/10.2514/6.2012-1169.

[141] F. J. Fahy, *Sound Intensity* (Elsevier Science Publishing Co., 655 Avenue of the Americas, New York, NY 10010, USA, 1989).

[142] T. A. Stout, A. T. Wall, K. L. Gee, and T. B. Neilsen, "Obtaining acoustic intensity from multisource statistically optimized near-field acoustical holography," Proceedings of Meetings on Acoustics **33,** 055002 (2018).

[143] O. T. Schmidt and T. Colonius, "Guide to Spectral Proper Orthogonal Decomposition," AIAA Journal **58,** 1023–1033 (2020), https://doi.org/10.2514/1.J058809.

[144] E. G. Williams, "Continuation of acoustic near-fields," The Journal of the Acoustical Society of America **113,** 1273–1281 (2003), https://doi.org/10.1121/1.1528173.

[145] K. M. Leete, K. L. Gee, T. B. Neilsen, B. M. Harker, A. T. Wall, and M. M. James, "Azimuthal coherence of the sound field in the vicinity of a high-performance military aircraft," Proc. Mtgs. Acoust. **29,** 045007 (2016), https://doi.org/10.1121/2.0000673.

[146] J. E. Bridges, "Azimuthal Noise Directivity of Non-Axisymmetric Jets," AIAA SciTech Forum 2021-1183 (2021), https://doi.org/10.2514/6.2021-1183.

[147] B. Greska and A. Krothapalli, "On the far-field propagation of high-speed jet noise," Noise Control and Acoustics Division Conference 2008-73071 (2008), https://doi.org/10.1115/NCAD2008-73071.

[148] A. Adam, D. Papamoschou, and C. Bogey, "The Imprint of Vortical Structures on the Pressure Field at the Edge of a Turbulent High-Speed Jet," AIAA Scitech Forum 2021-1184 (2021), https://doi.org/10.2514/6.2021-1184.

[149] A. Towne, A. V. Cavalieri, P. Jordan, T. Colonius, V. Jaunet, O. Schmidt, and G. A. Brès, "Trapped acoustic waves in the potential core of subsonic jets," AIAA/CEAS Aeroacoustics Conference 2016-2809 (2016), https://doi.org/10.2514/6.2016-2809.

[150] A. Towne, O. T. Schmidt, and G. A. Brès, "An investigation of the Mach number dependence of trapped acoustic waves in turbulent jets," AIAA/CEAS Aeroacoustics Conference 2019-2546 (2019), https://doi.org/10.2514/6.2019-2546.

[151] H. Oertel, "Mach wave radiation of hot supersonic jets," Mechanics of sound generation in flows pp. 275–281 (1979).

[152] H. Oertel, in *Recent Contributions to Fluid Mechanics* (Springer, Berlin, Heidelberg, 1982), pp. 170–179, https://doi.org/10.1007/978-3-642-81932-2_18.

[153] C. K. W. Tam and F. Q. Hu, "On the three families of instability waves of high-speed jets," Journal of Fluid Mechanics **201,** 447–483 (1989).